Development of a Single Beam SERF Magnetometer using Caesium Atoms for Medical Applications

PhD Thesis

R. Dawson

Experimental Quantum Optics and Photonics Group

Department of Physics

University of Strathclyde, Glasgow

September 21, 2023

This thesis is the result of the author's original research. It has been composed by the author and has not been previously submitted for examination which has led to the award of a degree.

The copyright of this thesis belongs to the author under the terms of the United Kingdom Copyright Acts as qualified by University of Strathclyde Regulation 3.50. Due acknowledgement must always be made of the use of any material contained in, or derived from, this thesis.

Abstract

This thesis describes the design and implementation of a compact zero-field optically pumped magnetometer for human biomagetic measurements. This project aimed to achieve lower operating temperatures and a higher sensor bandwidth than current commercial rubidium-based equivalent sensors. Through careful selection of the sensing alkali, caesium, and all constituent components of the sensor package design, both of these aims are achieved.

All of the required systems and components for a single-beam zero-field magnetometer are discussed, including a high efficiency cell heating and monitoring system, multi-axis field control and the optical detection scheme. Through full understanding and development of these systems, miniaturised and microfabricated versions are developed that facilitate the construction of a sensor package with external dimensions of $25 \times 25 \times 50$ mm^3.

A number of machine learning tools are developed and applied to directly optimise the sensor's sensitivity through control of the appropriate operational parameters, yielding a factor of five improvement. These techniques also enabled the investigation of the effect of nitrogen buffer gas pressure on the sensor's measured sensitivity, demonstrating a linear increase in sensitivity with increasing pressure.

The prototype sensor demonstrated a significant advancement in terms of bandwidth achieving a linear frequency response up to $\simeq 900$ Hz. The external package temperature of the sensor for prolonged timescales (> 1 hour) maintained a skin-safe temperature (< 41 °C), with a biomagnetic field level sensitivity, 90 fT/$\sqrt{\text{Hz}}$, and compact package footprint, less than a square inch. A practical measurement of the magnetic field of a cardiac signal successfully demonstrates the sensor as a suitable biomagnetic measurement tool.

Acknowledgements

After completing my thesis, I now have the privilege of reflecting upon my journey and the chance to express my thanks to all those who have helped me. Firstly, I am deeply grateful for the guidance and unwavering support of my primary supervisor, Erling Riis. I extend my heartfelt appreciation to my secondary supervisor, Paul Griffin, for his meticulous reviews, expert insights, and dedicated involvement in various aspects of my thesis. Their mentorship has been instrumental in shaping both the quality of this research and me as a researcher.

Furthermore, this endeavour would not have been possible without my post-doctoral colleague and dear friend, Carolyn O'Dwyer. My gratitude for Carolyn's profound influence on my research and thesis cannot be overstated, alongside the entire SERF-project team; Edward Irwin, Marcin S. Mrozowski and Dominic Hunter. Their contributions, intellectual exchanges, and collaborative spirit were indispensable to the development of this research. Special recognition also goes to research fellow Stuart Ingleby, whose technical support throughout was invaluable.

I am also thankful to my thesis committee members, Robert Martin and Mark Fromhold, for their engagement in thoughtful discussions and feedback, which has enhanced the quality of this thesis.

I could not have undertaken this journey without my family and friends, who have been my biggest supporters while I've chased my career around the country, through various academic fields, without ever faltering to support me. In the hardest moments of both my research and the writing-up process, my dad has kept my spirits high through his unwavering belief in me, daily encouragement, advise and friendship. I am here today because of their belief in me.

Finally, special thanks go to my partner for their unwavering support, a thousand cups of tea, daily laughs, and for sharing in the journey of building a happy life alongside the pursuit of completing this PhD.

Contents

List of Figures

List of Tables

List of Acronyms

AC alternating current. 44

ADC analog-to-digital converter. 55

AWG american wire gauge. 110

CAD computer aided design. 53

Cs caesium. 40

DAC digital-to-analog converter. 96

DAQ data acquisition system. 46

DBR distributed Bragg reflector. 40

DC direct current. 51

DE differential evolution. 75

ECG electrocardiography. 2

EEG electroencephalography. 2

EMG electromyography. 2

FMCG fetal-magnetocardiography. 3

FWHM full-width at half-maximum. 30

GA genetic algorithm. 75

List of Acronyms

GD gradient descent. 85

GP Gaussian process. 80

GSHE ground state Hanle effect. 27

MCG magnetocardiography. 3

MEG magnetoencephalography. 3

MEMS microelectromechanical. 21

ML machine learning. 71

MLA machine learning algorithm. 73

MMG magnetomyography. 5

MOSFET metal–oxide–semiconductor field-effect transistor. 50

MRG magnetoretinograph. 3

MSR magnetically shielded room. 63

OO online optimisation. 74

OPM optically pumped magnetometer. 1

PCB printed circuit board. 53

PD photodetector. 96

PhD Doctor of Philosophy. 2

PID proportional–integral–derivative. 47

PSD power spectral density. 37

PWM pulse-width modulation. 47

SERF spin exchange relaxation free. 5

List of Acronyms

SNR signal-to-noise ratio. 4

SQUID superconducting quantum interference device. 3

SWAP size, weight, and power. 1

TEC thermoelectric cooler. 41

TIA transimpedence amplifier. 45

UART Universal asynchronous receiver-transmitter. 55

UV ultraviolet. 42

VCSEL vertical-cavity surface-emitting laser. 131

Chapter 1

Introduction

1.1 Introduction

Developments in metrological understanding and magnetometry technologies have made it possible to quantify smaller and smaller magnetic fields. The measurement of magnetic fields produced by biological functions, biomagnetism, has been achieved through realisation of ultra-sensitive magnetometers that are capable of detecting magnetic fields at sub picotesla scale ($< 10^{-12}$ T). Developments in the field of optically pumped magnetometers (OPMs) have delivered sensors capable of detecting biomagnetic signals in hand-held scale "portable" devices. Such OPMs provide both improvements in size, weight, and power (SWAP) and more modalities of sensing, than established technologies for biomagnetic sensing. However, production of ultra-sensitive OPMs at a portable scale for the use in biomagnetic sensing intersects and combines; 1) the challenges of highly sensitive sensor design and operation, 2) the constraints and challenges of miniaturised and microfabricated design processes and 3) operational, temperature and material constraints driven through the proximity of the sensor to a participant during biomagnetic sensing. There is a gap in the literature, due to commercialisation sensitivities, specifically regarding the development and production of OPM sensors for biomagnetic measurements that encompasses all aspects of sensor design, operation and testing.

The research in this thesis aims to develop the tools, software and hardware

required to build a portable OPM for biomagnetic sensing from base principles and explores the use of caesium for this purpose. This chapter will provide an introduction to the research undertaken during this Doctor of Philosophy (PhD), by first discussing the background and context of biomagnetism and optically pumped magnetometry.

1.2 Biomagnetism

Over 200 years ago Luigi Galvani, a physician and physicist, conducted experiments on the interdependence of electricity and muscle contraction in frogs [1], which is regarded as the discovery of the electrical phenomena associated with biological processes, electrophysiology. Electrophysiology is caused by the movement of ions across cell membranes, which generates electrical potentials and currents within biological systems. The first measurement of the electrical phenomena produced by an adult human heart, electrocardiography (ECG), was demonstrated in 1887 [2]. A vast array of electrophysiology measurements followed, including measurement of the electrical activity within the human brain, electroencephalography (EEG), first demonstrated in 1924 [3, 4], followed by demonstration of electrical activity during muscle contraction, electromyography (EMG), in 1929 [5–7]. Bioelectric phenomena studies are crucial for understanding many biological processes and have greatly advanced the understanding of human physiology. However, bioelectric signals are distorted by electrical fields generated by extracellular currents in human tissue [8,9] demonstrating a significant draw-back to non-invasive bioelectric measurement techniques.

A bioelectric current has an accompanying magnetic field, known as biomagnetism [10], that is not subject to the same deformation since tissue is magnetically transparent [11]. The lack of signal distortion allows for non-invasive measurements of biomagnetism measured outside of the body. However, biomagnetic signals are very small and the detection of such poses many technical challenges. The signal amplitude of biomagnetic signals are often of order 10^{-12} T, with the smallest signals such as evoked brain signals, measuring at $< 10^{-13}$ T. Sources of magnetism

and magnetic noise such as the Earth's magnetic field, power systems and electrical systems can overpower the measurement of tiny biomagnetic signals.

Baule and MaFee [12] recorded the first human biomagnetic measurement in 1963, with the detection of magnetic fields produced by the human heart, magnetocardiography (MCG), through use of an optimised induction coil assembly. Cohen also measured the heart field in 1967 through use of a copper induction coil detector, which he later used to successfully measure the brain's magnetic field in 1968, introducing the field of detection of magnetic fields produced by the human brain, magnetoencephalography (MEG). This first MEG measurement was enabled by use of a multi-layer magnetically shielded chamber used to attenuate large external sources of magnetic field.

The development of superconducting quantum interference devices (SQUIDs) in the 1970's facilitated measurement of biomagnetic fields with a better signal-to-noise ratio than recorded with induction coils [13–15]. SQUID-systems quickly advanced the field of biomagnetism measurements due to the high sensitivity capabilities at biomagnetic frequency ranges. SQUID dominance is further demonstrated by the gradiometric SQUID-system utilised in an unshielded environment in 1974 to first non-invasively record the in-vivo biomagnetic signal of the fetal heart, fetal-magnetocardiography (FMCG) [16], and the first measurement of the magnetic fields produced by the human eye in 1978, magnetoretinograph (MRG) [17]. Improvements in magnetometer sensitivity, magnetic shielding, and data processing continue to demonstrate biomagnetic measurements as a credible medical imaging tool [9, 18]. Today, SQUIDs in clinical MEG applications are developing to promising effect for both medical diagnosis, such as for the detection of cerebral haemorrhages [19] and diagnosis of Parkinson's disease symptom severity [20]. There are commercially available or prototype low T_C SQUID-based systems for various biomagnetic measurements; however, the use of SQUID-based systems impose a number of limitations due to the operational requirement for the system to be cryogenic cooled to $\simeq 4$ K. This cooling requirement is both costly and constrains the sensor placement in proximity to the patient, detrimentally affecting signal clarity due to

a large signal-to-noise ratio (SNR) [18,21]. High T_C SQUIDs are being explored for use within biomagnetic measurements, however, there is limited demonstrated use due to the technology not yet reaching the required level of maturity for mass production, leading to poor fabrication yield of sensors [22,23]. The demonstrated need for more effective and cost-efficient biomagnetic sensing has encouraged research in the field of quantum technology to develop innovative and resilient miniaturised technologies to prepare existing highly-sensitive OPMs for field deployment. This, in turn, drives the development of novel technologies such as compact lasers and microfabricated cells.

1.3 Optical magnetometry

Optical magnetometry utilises resonant light interactions with magnetically sensitive atomic vapour to detect magnetic fields. Atoms have a magnetic dipole moment, μ, that results from intrinsic properties of spin and electron charge. In the presence of an external magnetic field, B, the magnetic dipole experiences a torque, τ, orthogonal to μ and B:

$$\tau = \mu B \ . \tag{1.1}$$

The result is that the magnetic moment precesses about the magnetic field, B, at the Larmor frequency, ω_L.

$$\omega_L = \gamma |B| \ , \tag{1.2}$$

where γ is the atomic species dependent gyromagnetic ratio. The process of optically pumped magnetometry typically occurs in 3 stages.

1. **Pump**: The atomic vapour is optically pumped by polarised light tuned to the atomic resonance frequency. The light transfers angular momentum to the atomic ensemble, pumping the atoms into a polarised state and creates a net angular momentum, known as magnetisation.

2. **Precession**: Any external static magnetic field, B, that is applied to the

atomic ensemble causes the atomic polarisation to freely precess around the field at the Larmor frequency effectively causing the angular momentum of the atoms to precess.

3. **Probe**: The precession of the angular momentum of the atoms affects the atom-light interaction, which manifests as changes to the detected light transmitted through the atomic ensemble. The changes in light transmission is utilised to extract an accurate measurement of B-field.

Through this method we create a magnetised state of the atomic ensemble; however, this magnetisation has a finite lifetime due to relaxation mechanisms. In the 1970's, Happer and Tang discovered that a dominant relaxation mechanism, spin-exchange broadening, vanishes at extremely high alkali density [24]. This discovery started a branch of OPM development in which the OPM is designed such that spin-exchange broadening is suppressed, known as the spin exchange relaxation free (SERF) regime. SERF regime magnetometry maximises atomic polarisation lifetime to improve sensor sensitivity capabilities, discussed further in Chapter 2. SERF OPMs have demonstrated magnetic field sensitivity that approaches the sensitivity capabilities of SQUIDs, legitimising the use of SERF regime OPMs as a complimentary avenue for biomagnetic research alongside SQUID-based systems [25–27]. SERF OPMs have been demonstrated extensively using a range of alkali atom species and buffer gases reaching $\mathrm{fT}/\sqrt{\mathrm{Hz}}$ sensitivity [28–30], with the highest recorded sensitivity reaching 160 $\mathrm{aT}/\sqrt{\mathrm{Hz}}$ [31] in a controlled lab environment. OPMs do not require cryogenic cooling, providing a major advantage of OPMs compared to low temperature SQUIDs. The relative simplicity of OPMs design facilitates smaller, more portable sensors that can be placed much closer to the source of biomagnetic signals to improve the signal to noise ratio [25].

Figure 1.1 illustrates the signal amplitude and frequency range for a number of biomagnetic signals, indicated through the coloured regions. The simulated time domain signals can be observed for the biomagnetic measurements, including MCG, MEG and evoked muscle response measured through magnetomyography (MMG).

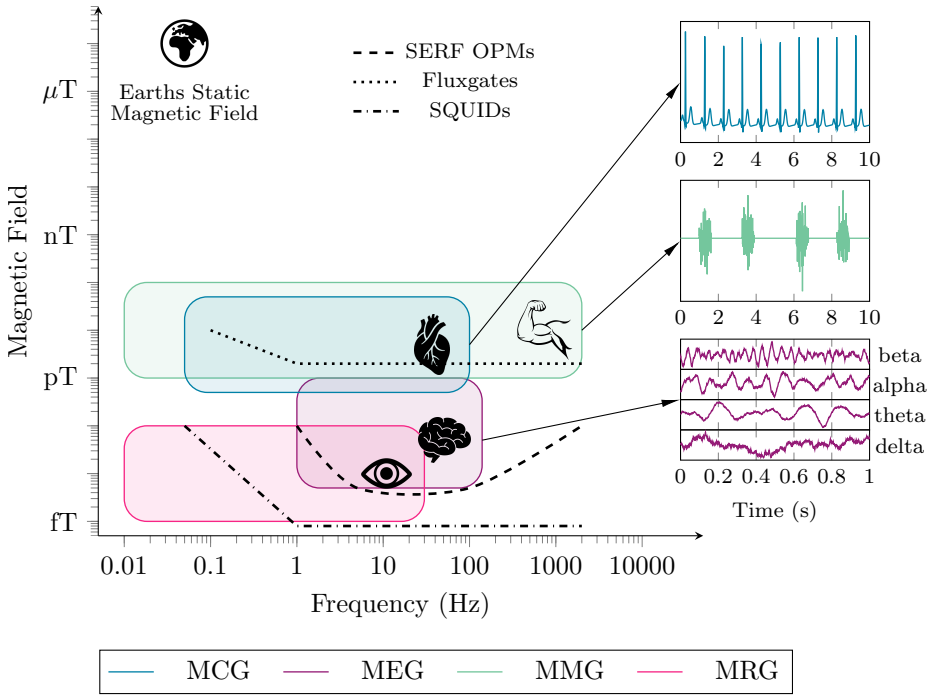

Figure 1.1: The magnetic field amplitude and frequency range for various biomagnetic signals with respect to the Earth's magnetic field. The various line types illustrate the approximate currently demonstrated capabilities of different magnetometer types, including SQUIDs, SERF OPMs, and fluxgate magnetometers. From the main graph the arrows point to examples of the time domain signals for three biomagnetic measurements, MCG, MEG and MMG, which are simulated and depicted in the right-hand column.

The dotted and dashed lines here indicate the capabilities of different types of magnetometers, including SQUIDs, SERF OPMs and fluxgate magnetometers.

1.4 Thesis structure

This thesis discusses the construction of a portable single-beam SERF OPMs using caesium atoms, for the use in biomagnetic measurements. The sensing head of the OPMs for biomagnetic measurements must be at a compact portable scale, to counter many of the issues of SQUID-based systems. Chapter 2 will provide a comprehensive overview of the atomic physics and optical magnetometry concepts that underpin the SERF magnetometer design and results presented in this thesis. In Chapter 3, the experimental setup at lab scale for the caesium SERF magnetometer is explored at a system, component and process level, to fully describe the magnetometers assembly and operation. Chapter 4 presents and demonstrates the effectiveness of machine learning techniques for optimisation of the SERF magnetometers performance through automated control of a selection of key operational parameters. The machine learning techniques are employed to benchmark magnetometer hardware improvements for fast characterisation of the magnetometers optimal performance. In Chapter 5, the development of a prototype portable version of the magnetometer is discussed, including description of the miniaturised components developed for the portable package. Practical biomagnetic measurements using the portable scale SERF magnetometer are also demonstrated in Chapter 5. Chapter 6 proposes a scheme of operation and measurement for the caesium SERF magnetometer that is less affected by extraneous magnetic fields. Lastly, Chapter 6 concludes the thesis through summary and presentation of future work.

SERF magnetometry was a new research interest for the Experimental Quantum Optics and Photonics group at the University of Strathclyde. The author, in collaboration with Edward Irwin, Marcin S. Mrozowski and postdoctoral researcher Carolyn O'Dwyer, actively contributed to the SERF magnetometry project, and subsequently made contributions to each other's work. The work reported in this thesis was the author's contribution, unless stated otherwise.

Publications arising from this work

- Dawson, R., O'Dwyer, C., Irwin, E., Mrozowski, M., Hunter, D., Ingleby, S., Riis, E., Griffin, P. F. *Automated Machine Learning Strategies for Multi-Parameter Optimisation of a Caesium-Based Portable Zero-Field Magnetometer.* Sensors. 2023; 23(8):4007. https://doi.org/10.3390/s23084007

- Dawson, R., O'Dwyer, C., Irwin, E., Mrozowski, M., McGilligan, J. P., Burt, D. P., Hunter, D., Ingleby, S., Riis, E., Griffin, P. F. (In Review). *A Portable Single-Beam Caesium Zero-Field Magnetometer for Biomagnetic Sensing.* Submitted July 2023, Journal of Optical Microsystems.

Chapter 2

General theory

Optical magnetometry uses light to measure the response of atoms to magnetic fields. Alkali metals contained within vapour cells underpin the development of highly sensitive magnetometers. Alkali vapour cells are relatively inexpensive, low-maintenance, low-power and physically robust to external temperature, pressure, and vibration. Optical pumping allows for control of the internal atomic states through use of the light polarisation to reach a well defined state in order to accurately predict atomic response to a magnetic field. This chapter will discuss the theories of atomic physics and optical magnetometry required to explain the experimental SERF magnetometer presented in this thesis.

2.1 Atomic structure

Alkali metal atoms are typically used in optically pumped magnetometry due to their accessible atomic transitions afforded by their atomic structure. Alkali metal atoms only have a single valence electron which allows for simplification of the atom energy as one electron outside of a central potential formed by the nucleus and closed energy shells. This simple structure allows for a well understood model of the dynamics of the electron spin. Through definition of alkali-metal atomic structure, the fundamental principles of atomic magnetometry can be explored. Such principles include discussion of how alkali atoms interact with magnetic fields and laser light,

as discussed in the following sections. Here a brief outline of atomic structure will be covered, in order to provide a framework for later discussion, for further details see [32] by Sobelman.

Alkali metal atoms have hydrogenic structure with a single valence electron occupying the outermost shell. The orbital angular momentum, **L**, arises due to the motion of the electron around the nucleus where $L = 0$ in the ground state and $L = 1$ in the first excited state.

2.1.1 Fine structure

Electrons have half-integer spin of $S = 1/2$ with corresponding spin angular momentum, $\mathbf{S} = 1/2$. The atomic fine structure arises due to magnetic interactions between the electron spin angular momentum, S, and the orbital angular momentum, L, to give the total angular momentum, **J**, where

$$\mathbf{J} = \mathbf{L} + \mathbf{S} \ . \tag{2.1}$$

The corresponding quantum number, J, is limited to integer steps within the range of $|L - S| \leq J \leq |L + S|$. The fine-structure spitting is hundreds of THz. Figure 2.1 shows the atomic structure of Cs, where atomic orbital and fine structure is denoted in the standard spectroscopic notation:

$$n^{2S+1}L_J \ , \tag{2.2}$$

where n is the principle quantum number and L denotes corresponding orbital such that $L = S, P, D, F, ...$

If a number of different atomic states share the same energy, the states are described as degenerate. The fine structure breaks the degeneracy of the first excited state. For example, in the case of caesium, fine structure separates the first excited state, 6^2P, of the $L = 1$ orbital into two so called fine-structure sub-levels; $6^2P_{1/2}$ and $6^2P_{3/2}$. The transitions, which represents the energy difference between these states, from the ground state, $6^2S_{1/2}$, to these excited states are known as the D_1

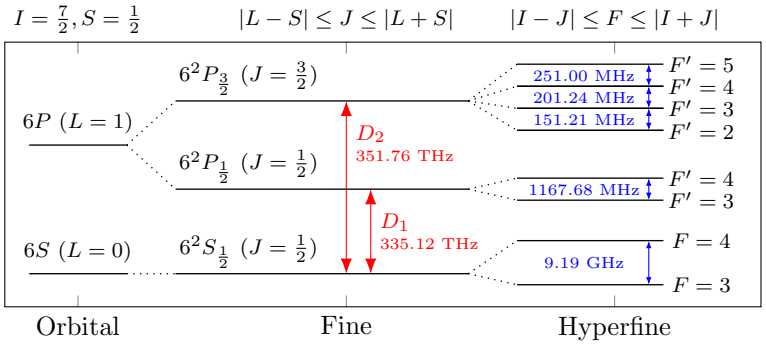

Figure 2.1: Energy structure diagram illustrating the orbital, fine and hyperfine structure of caesium atom. The red lines indicate the D_1 and D_2 transitions. The indicated splitting values are accurate [34] but not to scale

$(6^2S_{1/2} \rightarrow 6^2P_{1/2})$ and D_2 $(6^2S_{1/2} \rightarrow 6^2P_{3/2})$ transitions.

The energy shift, E_{fs}, between fine structure spectral lines is a function of the spin–orbit interaction constant β_{fs} is defined as [33]:

$$E_{\text{fs}} = \beta_{\text{fs}} \langle \mathbf{L} \cdot \mathbf{S} \rangle \tag{2.3}$$

$$= \frac{\beta_{\text{fs}}}{2} \left(J(J+1) - L(L+1) - S(S+1) \right) \ . \tag{2.4}$$

2.1.2 Hyperfine structure

The atomic hyperfine structure arises due to magnetic interaction between the total nuclear angular momentum, $\mathbf{I}$, with the angular momentum of the electron, $\mathbf{J}$, to give the total atomic angular momentum, $\mathbf{F}$, where;

$$\mathbf{F} = \mathbf{I} + \mathbf{J} \ . \tag{2.5}$$

The corresponding quantum number, F, is limited to integer steps within the range of $|I - J| \leq F \leq |I + J|$.

The energy shift, E_{hfs}, between hyperfine structure spectral lines is a function of

the hyperfine spin–orbit interaction constant, A_{hfs}, is defined as [33]:

$$E_{\text{hfs}} = A_{\text{hfs}} \langle \mathbf{I} \cdot \mathbf{J} \rangle \ , \tag{2.6}$$

For states with $\ell = 0$, such as the ground state;

$$E_{\text{hfs}} = \frac{A_{\text{hfs}}}{2} \left(F(F+1) - I(I+1) - J(J+1) \right) \tag{2.7}$$

2.2 Atom-field interaction

In the presence of an external magnetic field hyperfine magnetic sublevels are broken from degeneracy into m_f sublevels, known as Zeeman splitting. The number of m_f states for a given F state is given by $2F + 1$. For example, in the case of the caesium ground state, $6^2S_{1/2}$, $F = 4$ with corresponding sublevels $m_f = (-4, -3, -2, -1, 0, 1, 2, 3, 4)$ and $F = 3$ with corresponding sublevels, $m_f = (-3, -2, -1, 0, 1, 2, 3)$, as shown in Figure 2.4.

The hamiltonian H_B describes the atomic interaction with the magnetic field as:

$$H_B = \frac{\mu_B}{\hbar} (g_S \mathbf{S} + g_L \mathbf{L} + g_I \mathbf{I}).\mathbf{B} \ , \tag{2.8}$$

where μ_B is the Bohr magneton and g_S, g_L and g_I are electron spin, electron orbital, and nuclear g-factors respectively.

At the low field regime, as indicated by $\mu_B \ll A_{\text{hfs}} \langle \mathbf{I} \cdot \mathbf{J} \rangle$, the linear Zeeman effect occurs such that the energy splitting $E_{|F m_f\rangle}$ induced is small with respect to the hyperfine structure splitting.

$$E_{|F m_f\rangle} = \mu_B g_F m_f B_z \ , \tag{2.9}$$

where g_F is the hyperfine g-factor.

While we will not examine fields outside of this regime, it should be noted that the Breit–Rabi formula Equation (2.10) can be used to calculate the energy shifts for the states with $J = 1/2$ when subject to an external magnetic field [35]. For

example, in the case of caesium, Equation (2.10) can be utilised for the $6^2S_{1/2}$ and $6^2P_{1/2}$ states.

$$E_{|J=1/2 m_J I m_I\rangle} = -\frac{\Delta E_{\text{hfs}}}{2(2I+1)} + g_I \mu_B m B \pm \frac{\Delta E_{\text{hfs}}}{2}\left(1 + \frac{4m_F x}{2I+1} + x^2\right)^{1/2} , \quad (2.10)$$

where, $\Delta E_{\text{hfs}} = A_{\text{hfs}}(I + 1/2)$ and $m = m_I \pm m_J = m_I \pm 1/2$. In low magnetic fields $m = m_f$.

$$x = \frac{(g_J - g_I)\mu_N B}{\Delta E_{\text{hfs}}} , \quad (2.11)$$

where μ_N is the nuclear magneton.

Figure 2.2 shows the splitting of the caesium ground state, $6^2S_{1/2}$, with hyperfine levels $F = 3$ and $F = 4$, into the sublevels, m, under a large external magnetic field (Tesla level), calculated with Equation (2.10). Similarly, Figure 2.3 shows the splitting of the caesium ground state, $6^2S_{1/2}$, into the sublevels, m, under nT level external magnetic fields, as explored in this thesis.

2.3 Optical pumping

Optical pumping is the creation of non-equilibrium population states through the use of optical scattering [36]. The populations of states are given the Boltzmann distribution. For a system at temperature, T, with two states separated by energy ΔE, the ratio of the populations, $\frac{P_2}{P_1}$, can be expressed as;

$$\frac{P_2}{P_1} = \exp^{\left(\frac{-\Delta E}{k_B \cdot T}\right)} . \quad (2.12)$$

Zeeman state optical pumping occurs by shining polarised light resonant to the wavelength of an atomic transition through an atomic ensemble. The light polarisation is a manifestation of the resonant photons' angular momentum projected onto the beam axis, that transfers one unit of angular momentum to the atom's electron.

The effect of optical pumping, as illustrated in Figure 2.4, is two-fold, 1) excitation of the atom to the excited state, and 2) spontaneous decay of the atom

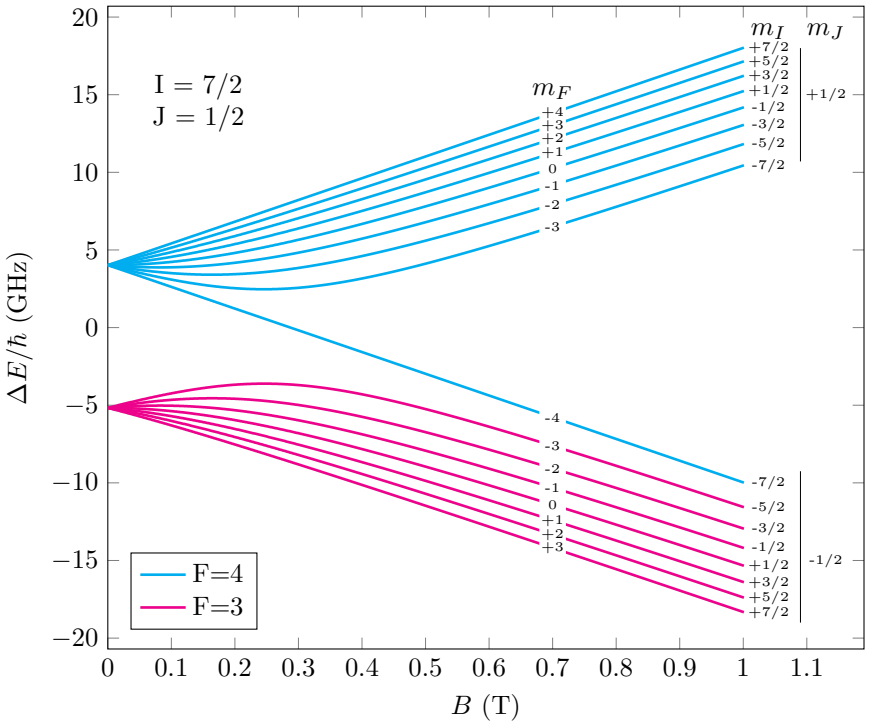

Figure 2.2: Breit Rabi Diagram for caesium, indicating the energy level splitting of the Zeeman sublevels for the ground-state $F = 3$ and $F = 4$ hyperfine levels, for Tesla level magnetic fields.

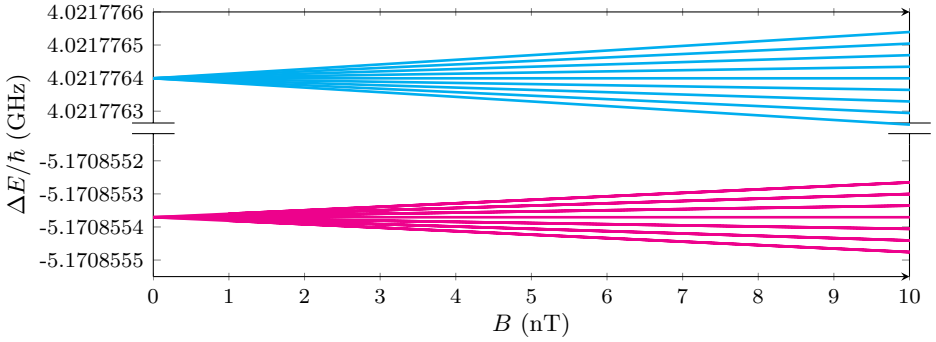

Figure 2.3: Breit Rabi Diagram for caesium, indicating the energy level splitting of the Zeeman sublevels for the ground-state $F = 3$ and $F = 4$ hyperfine levels, for magnetic fields up to 10 nT.

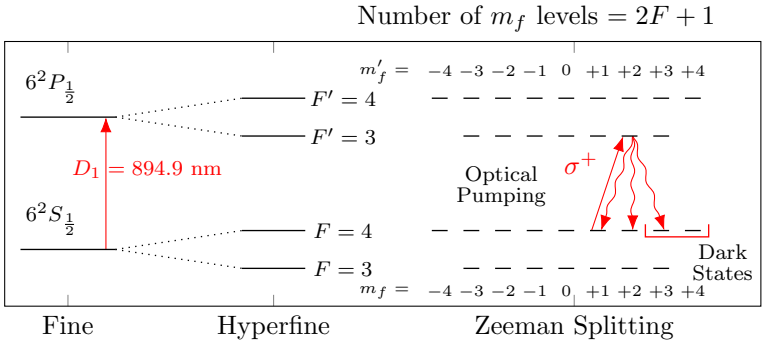

Figure 2.4: Fine, hyperfine and Zeeman splitting for caesium D_1 with optical pumping, adapted from [37]. Optical pumping is achieved using circular polarised light, that is orientated with respect to the B-field to give σ^+ transitions. On the left light is resonant with all states, whereas on the right it is resonant with $4 \rightarrow 3$ such that the atoms will only be pumped into F=3 Zeeman sublevels

back to the ground state manifold. The polarisation of the incident light determines the atoms excitation through "selection rules" for the magnetic sublevels, m_F, such that;

- $m'_f = m_f + 1$ for σ^+ transitions
- $m'_f = m_f - 1$ for σ^+ transitions
- $m'_f = 0$ for π transitions

However, the type of transition also depends on any applied B-field, for instance, in a system driving σ^+ transitions, reversing the direction of an applied B-field would drive σ^- transitions. Application of a shifting B-field to drive σ^+ then σ^- transition is fundamental in SERF magnetometry to measure magnetic resonance, as discussed further in Section 2.6.2.

In this thesis, light polarised to drive the σ^+ transitions and tuned to the D_1 transition of caesium ($\lambda = 894$ nm) is used throughout, as shown in Figure 2.4. As illustrated in Figure 2.4 an atom in $F = 4$ and $m_f = +1$ is optically pumped using σ^+ light to $F' = 3$ and $m'_f = +2$.

Spontaneous decay changes the state of the atom from the excited state to the ground state ($L = 1 \rightarrow L = 0$) by emitting a photon. This decay occurs through

one of three possible decay channels to return the atom to the ground state, such that;

$$m_f = m'_f + (1, 0, -1) \ , \tag{2.13}$$

where the probability of decaying to a particular channel depends on the Clebsch-Gordan coefficient, resulting in some proportion of the atomic ensemble to be optically pumped to a m_f ground state level with a higher quantum number.

Repeated pumping eventually creates populations of atoms in the two outermost magnetic sublevels, $m_f = 3$ and 4, (neglecting decay to the $F = 3$ sublevel), known as the stretched states. In these states, the atom can no longer be optically pumped as the light transfers no momentum to the atom, as such these are known as the dark states. By populating the dark states and depopulating other states, optical pumping leads to a non-equilibrium population distribution across the ground state resulting in a strong net magnetisation. The atomic ensemble in this state is referred to as polarised, and is highly sensitive to any magnetic field applied perpendicular to the laser beam axis.

2.4 Relaxation mechanisms

An optically pumped highly polarised atomic ensemble is depolarised by relaxation mechanisms. Relaxation randomises the atoms m_f states leading to depolarisation and loss of magnetic sensitivity. As such, relaxation mechanisms must be well defined, understood and controlled to ensure optimal sensitivity. Here, all relaxation mechanisms relevant to a microfabricated cuboid cell filled with caesium alkali vapour and nitrogen (N_2) gas will be discussed, as this type of cell will be utilised throughout all experimentation in this thesis.

2.4.1 Intrinsic relaxation

The total relaxation rate is a sum of effects intrinsic and extrinsic to the atomic vapour cell. Extrinsic relaxation effects are caused by operational processes, such as perturbation caused by laser light, and as such are managed through sensor design

and operation. Intrinsic relaxation processes are inherent to every vapour cell and are a function of the cell geometry and buffer gas quantity. The total relaxation rate, Γ_{total}, is the combination of all intrinsic relaxation mechanisms, which can be grouped as either relaxation due to atom-wall collisions, Γ_{wall}, or relaxation due to atom-atom collisions, $\Gamma_{\text{collisions}}$, such that;

$$\Gamma_{\text{total}} = \Gamma_{\text{wall}} + \Gamma_{\text{collisions}} \ . \tag{2.14}$$

2.4.2 Atom-wall collisions

Collisions of the caesium atoms with the glass cell walls are depolarising and can be effectively suppressed with the addition of buffer gases, such as nitrogen or neon, to the atomic vapour cell. For cells with buffer gas, the wall collision relaxation rate, Γ_{wall}, is diffusion limited, and hence a function of the diffusion coefficient, D. The diffusion coefficient is defined as $D = \frac{\lambda}{3}\bar{v}$ [38], where λ is the mean free path of an atom between collisions with buffer gas atom within the cell.

With the addition of a buffer gas the average velocity of the atoms, $\bar{v}$, can be expressed as [38];

$$\bar{v} = \sqrt{\frac{8k_B T}{\pi M}} \ , \tag{2.15}$$

where k_B is Boltzmann's constant, and T is temperature. The reduced mass, M, of both the masses of the alkali atom, m, and the buffer gas mass, m', is defined as;

$$\frac{1}{M} = \frac{1}{m} + \frac{1}{m'} \ . \tag{2.16}$$

The wall collision rate is most accurately described with respect to the vapour cell geometry. The cuboid geometry cells used within this research can be adequately modelled by a simplification to a well defined cylindrical geometry [39]. This assumes the effect of complex cuboid corner collisions are negligible.

$$\Gamma_{\text{wall}} = \left[\left(\frac{\pi}{d}\right)^2 + \left(\frac{2.405}{r}\right)^2 \right] \frac{D n_0}{n_b} \sqrt{\frac{T}{273.15\text{K}}} \ , \tag{2.17}$$

where n_b is the buffer gas number density and n_0 is the Loschmidt constant. For cylindrical geometry, the radius, r, of the circular face and the height, d, of the cylinder, map to the required cuboid geometry such that $r = F$ for a square-faced cuboid with dimensions $= F \times F \times d$.

2.4.3 Atom-atom collisions

Atom-atom collisions are spin depolarising, manifesting in two distinct ways, 1) spin-exchange that preserves the total atomic spin of the colliding pair, and 2) spin-destruction that randomise atomic polarisation post collision. The total relaxation due to collisions, $\Gamma_{\text{collisions}}$, is defined as the sum of spin-exchange, Γ_{SE}, and spin-destruction relaxation, Γ_{SD}.

$$\Gamma_{\text{collisions}} = \Gamma_{SE} + \Gamma_{SD} \ . \tag{2.18}$$

Γ_{SE} and Γ_{SD} are further defined as the sum of all types of atom-atom collisions possible within the atomic vapour cell, in this case; caesium-caesium (Cs-Cs) and caesium-nitrogen (Cs-N_2).

$$\Gamma_{\text{SD}} = \Gamma_{\text{SD}}^{\text{Cs-Cs}} + \Gamma_{\text{SD}}^{\text{Cs-N}_2} \ , \tag{2.19}$$

$$\Gamma_{\text{SE}} = \Gamma_{\text{SE}}^{\text{Cs-Cs}} \ . \tag{2.20}$$

The general equation for relaxation due to atom-atom collisions is given by:

$$\Gamma = q\sigma n\bar{\nu} \ , \tag{2.21}$$

where n is the caesium vapour density and σ is the cross-section giving the probability of a spin-destruction or spin-exchange event to occur during a collision. The relevant cross section values for caesium are summarised in Table 2.1 adapted from [28]. The degree to which spin coherence is maintained, described by the nuclear slowing down factor, q, is dependent on the atomic spin polarisation, P, of the atomic ensemble. For a highly polarised atomic ensemble, $P \simeq 1$, the nuclear slowing down

factor, q_{hp}, is described as;

$$q_{\mathrm{hp}} = 2I + 1 \ , \tag{2.22}$$

such that for a highly polarised atomic ensemble of caesium atoms where $I = 7/2$, $q = q_{\mathrm{hp}} = 8$ [38].

Table 2.1: Cross section values for SE between alkali-alkali atoms, SD between alkali-alkali, and alkali-buffer gas atoms. For caesium (Cs) alkali and nitrogen (N_2) buffer gas.

Caesium cross sections σ	
$\sigma_{\mathrm{SE}}^{\mathrm{Cs-Cs}} =$	$2.1\mathrm{x}10^{-14}\mathrm{cm}^2$ [40, 41]
$\sigma_{\mathrm{SD}}^{\mathrm{Cs-Cs}} =$	$2.0\mathrm{x}10^{-16}\mathrm{cm}^2$ [41]
$\sigma_{\mathrm{SD}}^{\mathrm{Cs-N_2}} =$	$5.5\mathrm{x}10^{-22}\mathrm{cm}^2$ [42]

2.4.4 Transverse and longitudinal relaxation

The discussed relaxation mechanisms apply only with respect to the beam axis such that separate total relaxation rates are defined for the longitudinal and transverse axes, corresponding to polarisation lifetimes T_1 and T_2 respectively. The longitudinal relaxation rate, Γ_1, is composed of mechanisms that affect the spin component along the beam axis (z). Conversely, the transverse relaxation rate, Γ_2, is composed of mechanisms that affect the spin component orthogonal to the beam axis (x or y).

$$\Gamma_1 = \frac{1}{T_1} = \Gamma_{\mathrm{wall}} + \Gamma_{\mathrm{SD}}^{\mathrm{Cs-Cs}} + \Gamma_{\mathrm{SD}}^{\mathrm{Cs-N_2}} \ , \text{ and} \tag{2.23}$$

$$\Gamma_2 = \frac{1}{T_2} = \Gamma_1 + \Gamma_{\mathrm{SE}}^{\mathrm{Cs-Cs}} \ . \tag{2.24}$$

For the caesium SERF magnetometer presented throughout this thesis, the total relaxation, Γ_{total}, is derived from Equations 2.17, 2.21 and 2.24,:

$$\Gamma_{\mathrm{total}} = \Gamma_{\mathrm{wall}} + \Gamma_{\mathrm{SD}}^{\mathrm{Cs-N_2}} + \Gamma_{\mathrm{SE}}^{\mathrm{Cs-Cs}} \ , \tag{2.25}$$

$$= \left[\left(\frac{\pi}{d}\right)^2 + \left(\frac{2.405}{F}\right)^2\right] \frac{Dn_0}{n_{\mathrm{N_2}}} \sqrt{\frac{T}{273.15\mathrm{K}}}$$

$$+ \frac{1}{q}\sigma_{\mathrm{SD}}^{\mathrm{Cs-N_2}} n_{Cs-\mathrm{N_2}} \bar{v}_{Cs-\mathrm{N_2}} + \frac{1}{q_{SE}}\sigma_{\mathrm{SE}}^{\mathrm{Cs-Cs}} n_{Cs} \bar{v}_{Cs} \ , \tag{2.26}$$

where $\Gamma_{\text{total}} = \Gamma_2$ and spin destruction is dominated by alkali-buffer collisions due to high buffer gas density. The spin-exchange broadening factor, q_{SE}, is dependent on the ambient magnetic field magnitude and alkali vapour density. For caesium atoms at suitably high magnetic field ($\sim$10's of nT level [43]) $q_{SE} = \frac{7}{32}$, however $q_{SE} \to 0$ in zero-field sensing conditions, as will be explained in Section 2.6.

2.4.5 Intrinsic linewidth

Whilst intrinsic relaxation can be calculated numerically using Equation (2.24), Γ_2 can also be extracted experimentally through interrogation of the atomic vapour cell. The measured magnetic linewidth (described in Section 2.6.2) is composed of intrinsic relaxation processes and additional contributions from power broadening. To accurately measure the intrinsic linewidth, the effects of power broadening must be accounted for. The effect of broadening is expected to be linear to power, however, for other power broadening effects, such as in optical spectroscopy, the broadening scales as a function of square-root of power. A measurement of the magnetic linewidth with respect to laser power allows for extrapolation of the zero-crossing which corresponds to zero power and subsequently the intrinsic linewidth Γ.

2.5 Buffer gas effects

The caesium atomic vapour cell used throughout this thesis contains nitrogen buffer gas. The various intrinsic relaxation mechanisms vary with the amount of buffer gas added to the atomic vapour cell, as shown in Figure 2.5 modelled using Equation (2.26).

Relaxation due to alkali-wall collisions, Γ_{wall}, reduces with increasing buffer gas pressure, indicated by the dashdotted line in Figure 2.5. The increased buffer gas pressure means more nitrogen atoms are available to slow down alkali diffusion and increase the time between the alkali-wall collisions. However, the addition of more buffer gas atoms increases the rate of alkali-buffer gas spin-destruction collisions, $\Gamma_{\text{SD}}^{\text{Cs}-\text{N}_2}$, indicated by the dotted line in Figure 2.5. Spin-exchange collisions are

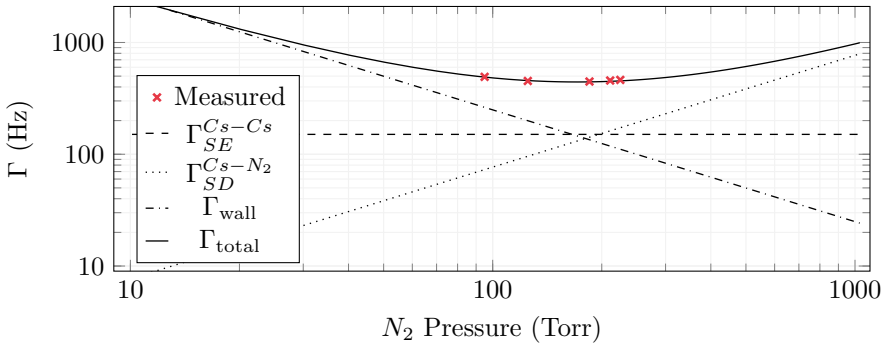

Figure 2.5: Intrinsic linewidth measured for a range of microelectromechanical (MEMS) atomic vapour cells, with internal dimensions of $6 \times 6 \times 3$ mm^3. Five atomic vapour cells with distinct pressures are tested, spanning a range of nitrogen buffer gas pressures ($95, 125, 185, 211$ and 225 Torr). The intrinsic linewidth, Γ, is extracted for each cell with the measured value, Γ Measured, indicated by crosses and the modelled total relaxation rate, Γ_{Total}, is indicated by the solid line. Each component of the total relaxation rate, as in Equation (2.25) where $q_{SE} = 4$, is indicated by various line types.

dominated by alkali-alkali collisions, therefore relaxation due to spin-exchange collisions, $\Gamma_{\text{SE}}^{\text{Cs-Cs}}$, remains constant regardless of buffer gas pressure, indicated by the dashed line in Figure 2.5.

The total relaxation rate, Γ_{total}, combines all relaxation mechanisms, indicated by the solid line in Figure 2.5. The total relaxation rate can be used to find the optimum buffer gas pressure that considers the trade-off between increasing spin destruction rate and decrease in wall collision rate. For measurement of B-fields, we want to operate at a minimum total relaxation rate and subsequent narrow resonance. A region with the lowest total relaxation rate is indicated in Figure 2.5 by the trough of the curve, correlating to a region of potential optimal buffer gas pressure at $\simeq 150$ Torr.

The relaxation rate calculations are also verified through experimentally measured intrinsic linewidth values indicated in Figure 2.5 by the red crosses. The intrinsic relaxation rates of the measured points were taken in the same manner as in Section 2.4.5, for a range of caesium microfabricated cells with different pressures of nitrogen buffer gas (all cells have identical geometry and were heated to 90 °C).

With the addition of buffer gas, the atomic spectral lines are both 1) broadened

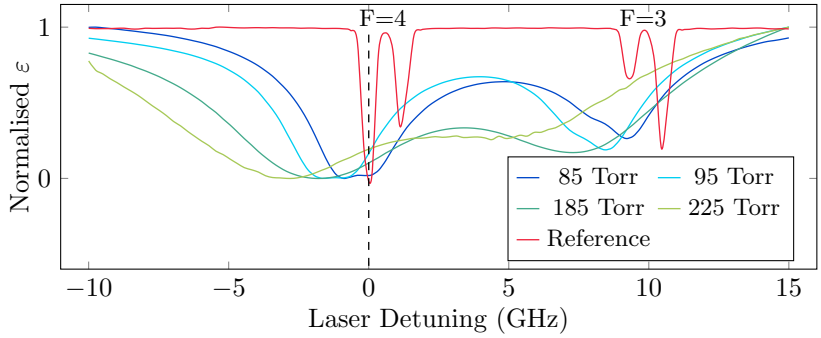

Figure 2.6: Spectroscopy of various caesium MEMS cells. The red line indicates a reference cell. Colour indicated the various cells and corresponding nitrogen buffer gas pressure.

and 2) frequency shifted, due to collisions with the buffer gas molecules. Absorption spectroscopy measures the absorption of light incident through an atomic ensemble as a function of wavelength or frequency, resulting in a number of dips in measured light transmission, ε, correlating to appropriate hyperfine components as defined in Section 2.1. Figure 2.6 shows a well-defined absorption spectrum for a caesium only reference cell (Thorlabs GC25075-CS) indicated by the red line. The broadening and frequency shifting phenomena caused by buffer gas increases with increasing buffer gas pressure [44], for example, at 21 °C, the linewidth broadens by 30.93 ± 5.71 MHz/Torr, and shifts by -7.38 ± 0.11 MHz/Torr [45]. Figure 2.6 demonstrates this broadening and shifting for a range of cells (with identical geometries) with varying buffer gas pressures (85 to 225 Torr indicated by line colour). All cells were measured experimentally where transmission, ε, is normalised between 0 and 1 for each cell.

The same physical collision mechanisms due to the buffer gas affects all the alkali atoms in the same way, which results in the observed homogeneous broadening of spectral lines seen in Figure 2.6. This broadening effect on the absorption profiles of the optical transitions enables the simultaneous pumping to both excited states using a single narrow-band laser for buffer gas pressures $\gtrsim 100$ Torr.

A Voigt profile, including the appropriate hyperfine components, fit to the absorption spectrum identifies homogeneous broadening of the Lorentzian linewidth caused by nitrogen buffer gas, Γ_{N_2}, and a characteristic shift of the transition fre-

quencies, Δ_{N_2}. The ratio of $\Gamma_{N_2}/\Delta_{N_2}$ is suitably well defined such that it can be used to analytically extract the buffer gas pressure within an atomic vapour cell [45].

2.6 Suppressing spin exchange relaxation

In zero-field conditions with high alkali vapour density the relaxation effect of spin-exchange collisions can vanish [46]. Operation within this scheme is known as the SERF regime. Counterintuitively, in the SERF regime spin-exchange relaxation is largely reduced by increasing the rate of spin-exchange collisions Γ_{SE} [29].

During spin-exchange collisions, spin directions of colliding atoms may be reversed resulting in a swap of the sign of their electron spin, S. For example, atom A with electron spin $S_A = 1/2$ and atom B has electron spin $S_B = -1/2$ collide and spin-exchange such that atom A and B may have swapped electron spin to $S_A = -1/2$ and $S_B = 1/2$ respectively [46]. Consequently, the atomic angular momentum jumps between the states of total angular momentum $F = I + 1/2$ and $F = I - 1/2$ [24]. As such spin-exchange collisions leads to a change in precession direction whilst conserving angular momentum. The average precession frequency of the atomic ensemble is altered by the time it takes to change precession direction after spin-exchange collisions, as such the average precession frequency is tied to the spin-exchange rate.

At high atomic density, statistical analysis of the effect of spin-exchange defines the average precession frequency, $\bar{\omega}$, as a function of the Larmor frequency, ω_L, and nuclear spin, I [46].

$$\bar{\omega} = \frac{6I + 3}{4I^2 + 4I + 4}\omega_L \ . \tag{2.27}$$

The effect of spin-exchange relaxation on the average precession frequency is determined by the relationship between the Larmor frequency and the rate of spin-exchange collisions, Γ_{SE}, in the follow ways:

- **Slow spin-exchange rate,** $\Gamma_{SE} < \omega_L$:

  If the Larmor frequency is higher than the spin-exchange rate the atoms precess freely in one of the hyperfine states multiple times before switching to another

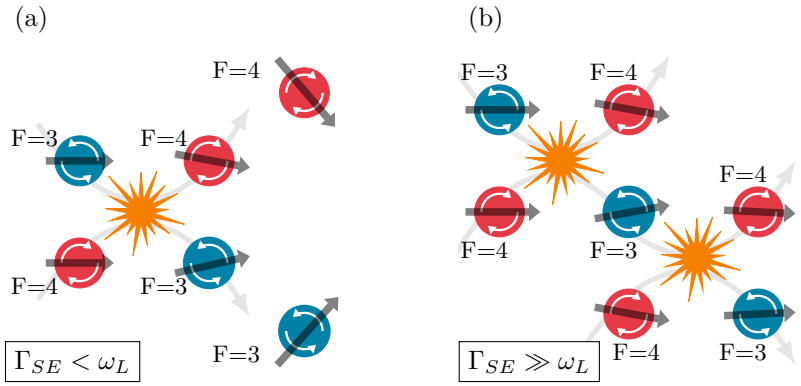

Figure 2.7: Diagram of spin-exchange collisions, indicated by orange starburst, for different spin-exchange rates, Γ_{SE}. The atom colour indicates the hyperfine state and precession direction. Spin-exchange collisions change an atoms hyperfine state causing the atoms to precess at Larmor frequency, ω_L, in the opposite direction. **a)** Slow spin-exchange rate, $\Gamma_{SE} < \omega_L$. After a spin-exchange collision, the atoms decoherently precess in opposite directions. **b)** Fast spin-exchange rate, $\Gamma_{SE} \gg \omega_L$, in the SERF regime. A high rate of spin-exchange collisions causes the atoms to precess between collisions only marginally before another spin-exchange collision occurs. The populations of the two hyperfine levels subsequently precess coherently.

hyperfine level post collision. Figure 2.7(a) illustrates the decoherence of two atoms post collision.

- **Intermediate spin-exchange rate,** $\Gamma_{SE} > \omega_L$:

  As the spin-exchange rate is increased the atoms undergo less precession between collisions. Once the spin-exchange rate is larger than the Larmor precession frequency, individual atoms spend less time in an individual hyperfine state and only precess a small amount between collisions.

- **Fast spin-exchange rate,** $\Gamma_{SE} \gg \omega_L$:

  If the spin-exchange rate is much faster than the Larmor frequency, the precession between collisions is so small that atoms in the two hyperfine levels become locked together as they experience the same slower net precession frequency $\bar{\omega}$. Figure 2.7(b) illustrates the coherence of two atoms post multiple collision. Statistically the atoms spend more time in the upper $F = I + 1/2$ hyperfine level due to the higher number of Zeeman sublevels than the lower hyperfine level, which determines the direction of the net precession. Spin-

exchange collisions no longer cause spin relaxation because the entire alkali ensemble precesses coherently [38, 46, 47].

In operation the SERF regime is reached through the combination of high vapour density and a zero magnetic field environment provided through magnetic shielding and residual field compensation using magnetic field coils.

2.6.1 High vapour pressure

The relationship between vapour pressure, P_v, and temperature, T, is described by the Clausius–Clapeyron equation;

$$\frac{dP_v}{dT} = \frac{P_v \Delta H}{RT^2} \ , \tag{2.28}$$

where R is the universal gas constant and ΔH is the heat of vapourisation as a function of temperature.

The integrated form of Equation (2.28) can be derived such that vapour pressure is expressed in terms of only temperature and a number of constants that are specific to the atomic species [48]:

$$P_v = 10^{\left(A + \frac{B}{T} - CT + D \log_{10} T\right)} \ , \tag{2.29}$$

where constants A, B, C and D are well defined in the literature for each atomic species [34, 49, 50].

Through combination of the ideal gas law and the definition of vapour pressure in Equation (2.29), the atomic density, ρ, is expressed as;

$$\rho = \frac{133.3 \times 10^{\left(A + \frac{B}{T} - CT + D \log_{10} T\right)}}{RTm} \ , \tag{2.30}$$

where m is the atomic mass.

The consensus within SERF literature defines the atomic density required for SERF regime magnetometry as $\rho \simeq 10^{14}$ cm^{-3}, where the corresponding cell temperature is dependent on the atomic species utilised; caesium $T \simeq 120$ °C [51],

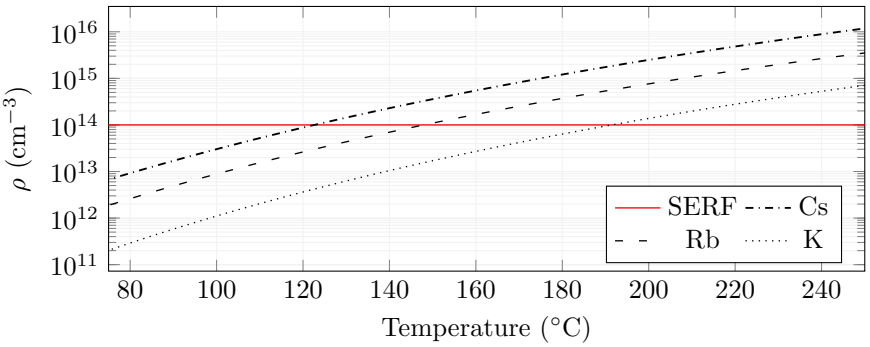

Figure 2.8: Atomic density, ρ, of caesium (Cs), rubidium (Rb) and potassium (K), with respect to temperature. The density required for SERF regime magnetometry (10^{14} cm^{-3}) is indicated by the red line.

rubidium $T \simeq 150$ °C [52] and potassium (K) $T \simeq 190$ °C [28]. Figure 2.8 illustrates density, ρ, with respect to temperature for various alkali species typically used for magnetometry, calculated with Equation (2.30). The density required for SERF regime magnetometry (10^{14} cm^{-3}) is illustrated by the red line.

The temperature of the atomic vapour cell is of particular interest for magnetometers where the intended use is for biomagnetic measurements. During biomagnetic measurements an external face of the atomic sensor will be in close proximity to a participants' skin. Operationally, this means the external package of the magnetometer must be skin safe. IEC 60601 [53] defines the technical standards for the safety and essential performance of medical electrical equipment, set by the International Electrotechnical Commission. IEC 60601-1 specifies the maximum allowed external temperature limit for a device that has contact with healthy skin of an adult, based on touch duration t. For measurements that require over 10 minutes of touch duration $t > 10$ min, the allowable maximum temperature is 41 °C [53]. As such, here we define the maximum skin-safe temperature for the external face of the sensor as 41 °C.

Based on discussions and personal experience, rubidium SERF sensors experience significant heat generation during operation, with temperatures reaching up to $\gg$ 41 °C, causing discomfort. In this thesis caesium was selected as the sensing alkali due to the lower temperature required to reach the SERF regime atomic density.

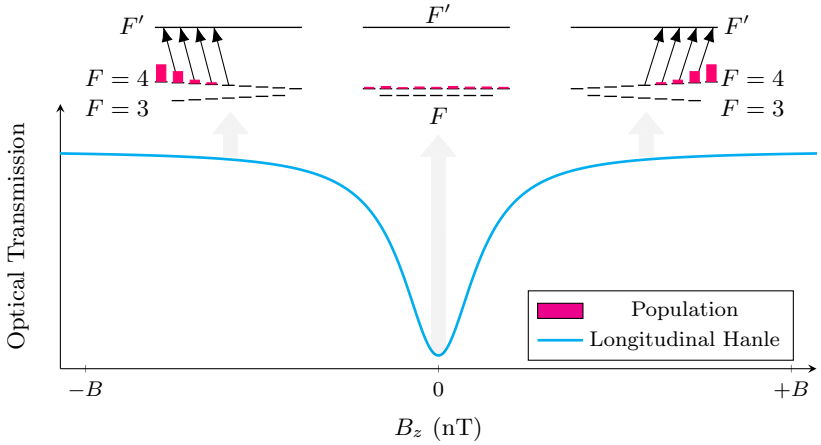

Figure 2.9: Diagram of the ground state Hanle effect, demonstrated as a change in optical transmission with respect to a magnetic field applied along the beam axis, B_z. The inset graphs show the hyperfine manifold of caesium at various values of applied field, as shown by the grey arrows. The break in degeneracy of the Zeeman sublevels caused by the magnetic field allows for large population (pink) distributions to the dark states.

2.6.2 Ground state Hanle effect

Magnetometers operating in the SERF regime exploit the ground state Hanle effect (GSHE) to generate a magnetic resonance. GSHE resonances are absorptive measurements manifesting as changes in transmitted optical power when the atomic ensemble is subject to a static magnetic field that is swept through zero from negative ($-B$) to positive ($+B$).

The longitudinal GSHE is realised when a static magnetic field is applied along the beam axis, when optically pumped with circularly polarised light. The longitudinal GSHE is illustrated in Figure 2.9. The break in degeneracy of the Zeeman sublevels caused by the magnetic field allows for large population distribution to the dark states (for $-B$, $m_f = -4$ and -3) resulting in a highly polarised atomic ensemble and high transmission of laser light. As the applied static field is swept to zero, $B \to 0$, ground state populations redistribute evenly resulting in less optical pumping, more absorption of light and less light transmission. Finally, as the applied static field is swept strongly in the opposite direction to the initial field, degeneracy of the hyperfine manifold is again broken to allow large population distribution to

the dark states (for $+B$, $m_f = 4$ and 3), resulting in a highly polarised atomic ensemble with high transmission of laser light. As such, the GSHE results from the interplay of polarisation creation, stabilisation, and depolarisation as a response to a static magnetic field [54].

Longitudinal (along the beam axis) and transverse (orthogonal to the beam axis) magnetic field components affect the atomic polarisation distinctly differently. The Bloch equations provide a foundation to phenomenologically describe atomic magnetisation. This is realised firstly with the use of the equation of motion for a classical magnetic dipole to describe the vector change in magnetisation with time $\dot{\underline{M}}$

$$\dot{\underline{M}} = \gamma \underline{M} \times \underline{B}(t) - \underline{\Gamma}.\underline{M} + \Gamma_P \underline{M_0} \ , \tag{2.31}$$

where γ is the gyromagnetic ratio, $\underline{B}(t)$ is the magnetic field applied to the atoms. The relaxation rate, $\underline{\Gamma}$, consists of the longitudinal relaxation rate, Γ_1, and the transverse relaxation rate, Γ_2 on the appropriate axes. Γ_P is relaxation due to optical pumping along the beam axis defined in $\underline{M_0}$. $\underline{M}$ is the magnetisation vector;

$$\underline{M} = \begin{pmatrix} M_x \\ M_y \\ M_z \end{pmatrix} \ . \tag{2.32}$$

Through definition of the applied magnetic field $\underline{B}(t)$, the system can be interrogated to demonstrate separate components of the atomic response such as the transverse, longitudinal and magnetically modulated responses.

2.6.3 Transverse magnetic resonance

The transverse resonance occurs when the magnetic field varies in an orthogonal plane to the direction of the pump beam [55]. A transverse resonance is realised through application of a sweeping magnetic field in an axis transverse to the beam axis, z, from positive to negative, in this instance y. Thus, for the most simple case,

the applied magnetic field $\underline{B}(t)$ is expressed as;

$$\underline{B}(t) = \begin{pmatrix} 0 \\ B_y \\ 0 \end{pmatrix} . \tag{2.33}$$

Substituting $\underline{B}(t)$ into Equation (2.31), where $\Gamma = \Gamma_1 = \Gamma_2$, due to the suppression of spin-exchange, Equation (2.24), as a result of operating in the SERF regime. The change in magnetisation vector, $\dot{\underline{M}}$, can be defined as:

$$\dot{\underline{M}} = \begin{pmatrix} -\Gamma & 0 & -\gamma B_y \\ 0 & -\Gamma & 0 \\ \gamma B_y & 0 & -\Gamma \end{pmatrix} \underline{M} + \begin{pmatrix} 0 \\ 0 \\ \Gamma_P M_0 \end{pmatrix} . \tag{2.34}$$

The equations for magnetisation along each axis can subsequently be defined as;

$$M_x = \frac{-\gamma B_y}{\Gamma^2 + \gamma B_y^2}(\Gamma_P M_0) , \tag{2.35}$$

$$M_y = 0 , \tag{2.36}$$

$$M_z = \frac{\Gamma}{\Gamma^2 + \gamma B_y^2}(\Gamma_P M_0) . \tag{2.37}$$

From here we will assume $\Gamma_P M_0 \to 1$ due to efficient optical pumping.

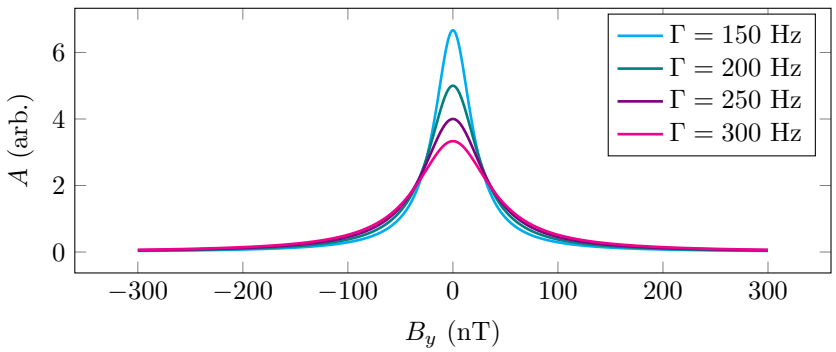

Figure 2.10: Transverse Hanle amplitude (arb) with sweeping B_y (nT), for a range of relaxation rates, Γ (Hz).

The resultant magnetisation vector, R, across the two transverse axes reflects

the light transmitted through the cell, where $R = \sqrt{{M_x}^2 + {M_y}^2}$. In practical terms, the transmission signal is measured as a change in light intensity amplitude, A, on the photodetector measured in volts.

Using Equations (2.35 & 2.36), the amplitude of light intensity, A, is modelled with respect to a sweeping transverse field, B_y, demonstrating the transverse Hanle effect as shown in Figure 2.10. The transverse Hanle effect lineshape varies in amplitude with respect to total relaxation rate, Γ, due to homogeneous broadening, as demonstrated by the coloured lines in Figure 2.10, ranging from 150 to 300 Hz. The peak of the transverse resonance indicates the value of the applied transverse magnetic field, B_{y_0}, at which the atoms experience close to zero-field.

The transverse resonance is described here as the 1D Hanle resonance and is homogeneous resulting in a Lorentzian profile. A Lorentzian model, S_{1D}, is used to extract key lineshape parameters:

$$S_{1D} = A_0 \left(\frac{\Gamma^2}{\Gamma^2 + (B_y - B_{y_0})^2} \right) + C \ , \tag{2.38}$$

where B_y denotes the magnetic field values that are swept along the y axis. An offset, C, accounts for the background signal. The resonance peak signal amplitude, A_0, and full-width at half-maximum (FWHM) Γ are also described through function Equation (2.38).

Figure 2.10 and Equations (2.35 & 2.36), demonstrates how the sharpness of the transverse Hanle resonance depends on total relaxation. We have already shown that the cell temperature is tied to relaxation as described by Equation (2.26), and as such can describe the transverse Hanle resonance with respect to temperature. The rate of spin-exchange collisions increase with an increase in cell temperature, and spin-exchange relaxation and total relaxation consequently decreases, as discussed in Section 2.6.

Figure 2.11 shows measured linewidths (black points) extracted from a number of transverse Hanle resonances measured using a caesium atomic vapour cell at increasing cell temperature, and modelled (black line) equivalent using Equa-

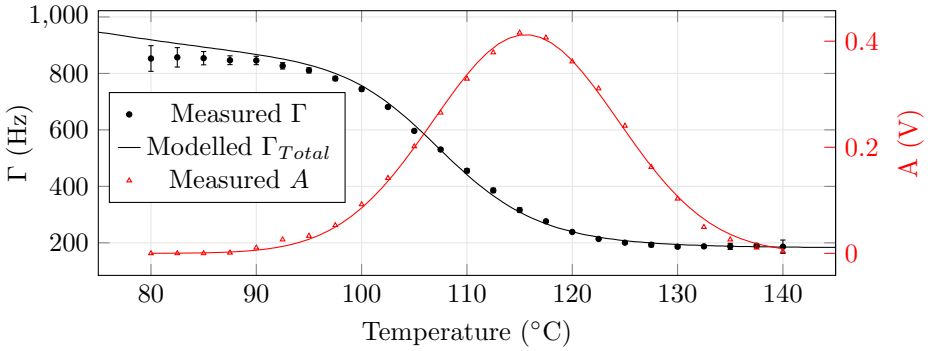

Figure 2.11: Measured resonance amplitude, A, in red and magnetic linewidth, Γ, in black of a caesium atomic vapour cell filled with 225 Torr of nitrogen buffer gas, at increasing cell temperature. The measured Γ is extracted from the transverse Hanle resonance, indicated by dots, and the model (Equation (2.26)) is fit indicated by the line. The measured peak amplitude value for each Hanle resonance are indicated by triangles, and a Gaussian curve is fit to the measured data.

tion (2.26). The narrowest magnetic linewidths are reached at $>$ 120 °C, which aligns with the expected temperature required to reach the desired atomic density, as shown in Figure 2.8.

However, whilst minimising linewidth is important, the resonance amplitude must be maximised to increase the SNR of the measured response. The opacity of the vapour cell increases with temperature to the detriment of the measured signal amplitude. Figure 2.11 shows resonance amplitude, A, with respect to temperature. A Gaussian curve (red line) fit to the measured resonance amplitude values (red triangles) is found by minimising the sum of squared errors.

As such, Figure 2.11 illustrates how amplitude decreases as temperature increases $>$ 115 °C. The trade off between amplitude and linewidth must be managed to locate the sharpest resonance to optimise SNR of the sensor.

2.6.4 Longitudinal magnetic resonance

Whilst transverse fields depolarise the atomic ensemble, longitudinal magnetic fields stabilise spin polarisation [54]. The longitudinal resonance occurs when the magnetic field varies in a plane parallel to the direction of the pump beam [54]. In this case, spin polarisation is proportional to both the magnetic field and the transverse

relaxation time of the electron spins. Here, the longitudinal resonance is modelled as a function of both transverse and longitudinal fields. From the equation of motion for a classical magnetic dipole Equation (2.31), a more complex definition of B-fields across two axes must be applied.

$$\underline{B}(t) = \begin{pmatrix} B_x \\ 0 \\ B_z \end{pmatrix} \ , \tag{2.39}$$

where B_x and B_z contribute to transverse and longitudinal Hanle effects. $\underline{\dot{M}}$ is now defined as:

$$\underline{\dot{M}} = \begin{pmatrix} -\Gamma & \gamma B_z & 0 \\ -\gamma B_z & -\Gamma & \gamma B_x \\ 0 & -\gamma B_x & -\Gamma \end{pmatrix} \underline{M} + \begin{pmatrix} 0 \\ 0 \\ \Gamma_P M_0 \end{pmatrix} \ . \tag{2.40}$$

The equations for magnetisation along each axis can subsequently be defined as;

$$M_x = \frac{\gamma^2 B_x B_z}{\Gamma^2 + \gamma {B_z}^2 + \gamma {B_x}^2} M_0 \ , \tag{2.41}$$

$$M_y = \frac{\gamma B_x}{\Gamma^2 + \gamma {B_z}^2 + \gamma {B_x}^2} \Gamma_P M_0 \ , \tag{2.42}$$

$$M_z = \left(1 - \frac{\gamma B_x^2}{\Gamma^2 + \gamma {B_z}^2 + \gamma {B_x}^2} \right) M_0 \ . \tag{2.43}$$

Similarly to Section 2.6.3, by using the resultant magnetisation vector from Equations (2.41 & 2.42), the amplitude of light intensity, A, is modelled with respect to a sweeping longitudinal field across B_z, demonstrating the longitudinal Hanle effect as shown in Figure 2.12.

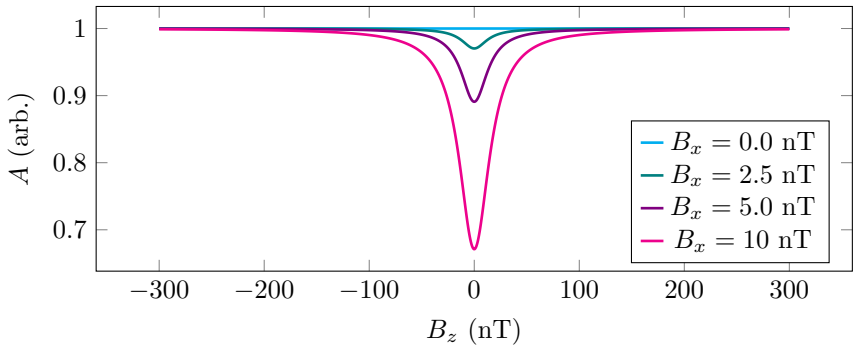

Figure 2.12: Longitudinal Hanle amplitude (arb) with sweeping B_z (nT), for a range of transverse fields, B_x (nT).

The atomic response as a function of magnetic field on orthogonal axes is described here as the 2D Hanle landscape, as seen in Figure 2.13. The solution to the Bloch equations with dual-axis magnetic fields, described in Equations (2.41), (2.42) and (2.43), describes the atomic response to form such a landscape. This feature of atomic response is used to identify and null any remaining magnetic fields across all axes of the SERF OPM. The point at which the transverse resonance is the most narrow, manifesting as the narrowest profile as seen in Figure 2.13, indicates the value of the applied longitudinal field at which the atoms experience close to zero-field, B_{z0}. The position of the peak of the most narrow transverse resonance identifies the zero-field point of the transverse axis, B_{x0}.

Experimentally, this landscape is found through iteratively sweeping the magnetic field across the x- and z-axes to generate a series of transverse Hanle resonances with respect to the longitudinal field. A Lorentzian model, S_{2D}, is used to extract the value of the applied transverse and longitudinal magnetic fields for zero-field (B_{x0} and B_{z0} respectively) and other key landscape parameters:

$$S_{2D} = A_0 \left(\frac{\Gamma^2 + (B_x + B_{x0})^2}{\Gamma^2 + (B_z + B_{z0})^2} \right) - C \ , \tag{2.44}$$

where B_x and B_z denote the magnetic field values that are swept along the x and z axes. C is the background offset, A_0 is the peak signal amplitude, and Γ is the FWHM on the resonance.

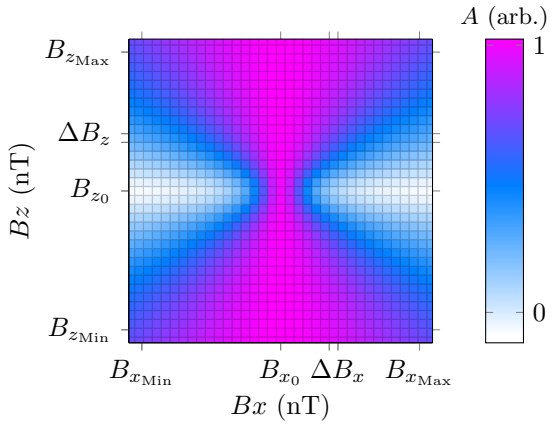

Figure 2.13: Simulated 2D Hanle Landscape, where colour indicates the amplitude of light intensity, A, from the resultant magnetisation vector found using Equations (2.41 & 2.42). The landscape is measured by rastering across the full range of B_x and B_z in steps of ΔB_x and ΔB_z. The point at which atoms experience close to zero-field is indicated at B_{x0} and B_{z0}.

2.6.5 Magnetic modulation response

OPM measurements run in schemes with only static field application, as seen in Sections 2.6.4 and 2.6.3 are highly sensitive to low frequency noise. In order to reduce the effect of low frequency noise and improve SNR, magnetic modulation is commonly used [25, 56].

Magnetic field modulation refers to the application of an oscillating magnetic field to the atomic ensemble that rotates the direction of the atomic spin polarisation, which in turn creates a large modulation of the light polarisation [57]. Modulation of the light polarisation induces a magnetic moment which changes the transparency of the atomic ensemble proportionally [58]. The transparency of the atomic vapour is detected through light transmission where the measured signal is shifted to higher frequencies by the modulation [59].

The measured modulated signal is demodulated through a lock-in detection scheme, which extracts the in-phase, X, and quadrature-phase, Y, components. The strength or power of the signal, R, is calculated as the square root of the sum of the squares of the X and Y components ($R = \sqrt{X^2 + Y^2}$). Signal recovery through this magnetic modulation and lock-in detection scheme shifts the measured signal

away from the low frequency end and increases the signal-to-noise ratio.

Whilst the relationship between amplitude and magnetic field is absorptive in a static scheme, as seen in Figures 2.10 & 2.12, the demodulated response, A_{Demod}, produces a dispersive curve with respect to a magnetic field applied orthogonal to the beam axis. Importantly, the dispersive curve amplitude response $A_{\text{Demod}} = 0$ at zero field (B_{y_0}), which allows for positive and negative field changes to be identified. Furthermore, the dispersive signal is used to lock the sensor to zero field through the use of external control to feedback to the zero field point, $A_{\text{Demod}} = 0$.

The demodulated response can be modelled again through use of Equation (2.31), where;

$$\underline{B}(t) = \begin{pmatrix} B_x \\ B_y + B_{My} \sin \omega_M t \\ B_z \ , \end{pmatrix} \tag{2.45}$$

where fields across all axes contribute to the demodulated response, and modulation is applied on the sensitive axis (y) at a given amplitude B_{My} and frequency $\omega_M t$. $\dot{\underline{M}}$ is now defined as:

$$\dot{\underline{M}} = \begin{pmatrix} -\Gamma & \gamma B_z & -\beta \\ -\gamma B_z & -\Gamma & \gamma B_x \\ \beta & -\gamma B_x & -\Gamma \end{pmatrix} \underline{M} + \begin{pmatrix} 0 \\ 0 \\ \Gamma_P M_0 \end{pmatrix} \ , \tag{2.46}$$

where $\beta = B_y + B_{My} \sin \omega_M t$.

The X, Y and R demodulated response amplitude A_{Demod} using a modelled time evolved solution to Equation (2.46) is shown in Figure 2.14.

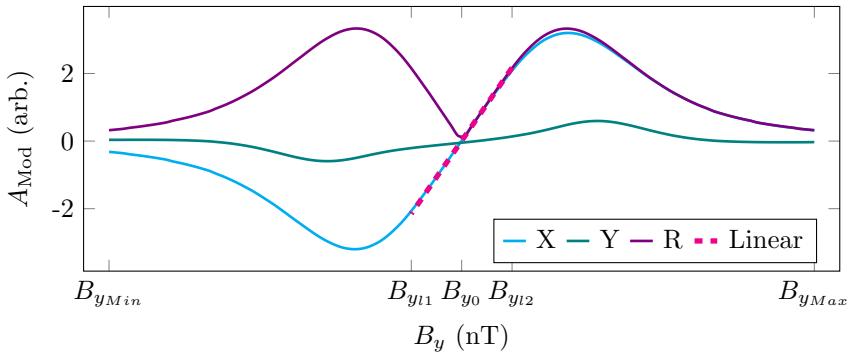

Figure 2.14: The modelled atomic response, found using a time evolved solution to Equation (2.46), to a sweeping field across the y-axis, from $B_{y_{\mathrm{Min}}}$ to $B_{y_{\mathrm{Max}}}$, through the zero-field point, B_{y_0}. The in-phase, X, quadrature-phase, Y, and resultant, R, demodulation components are extracted, where $R = \sqrt{X^2 + Y^2}$. The linear region (pink dashed) indicates the dynamic range, R_{dyn}, in which the measured response of in-phase component is proportional to the applied magnetic field, bound within the limits of $B_{yl1} \leq R_{dyn} \leq B_{yl2}$.

The linear region of the dispersive curve defines the dynamic range, R_{dyn}, of the sensor in which measured response of the signal is proportional to the applied magnetic field. Linearity is important for accurate sensing, to reliably provide the calibration of measured atomic response to a magnetic field value, within a small margin of error and to a high degree of certainty. A simple linear model is fit to the linear region of the in-phase component, X, of the demodulated atomic response, which in turn defines the linear region boundaries. Deviation from the linear fit within the linear region is expected as ≤ 1 % as a rule of thumb [25]. The linear region as illustrated in Figure 2.14 by the pink dashed line, is bound between B_{yl1} and B_{yl2}, such that $B_{yl1} \leq R_{dyn} \leq B_{yl2}$. The linear region boundaries are defined as the points after which deviation from linear fit exceeds the expected value (> 1 %). If the sensor is operated outside of the dynamic range in the non-linear region, through application of fields $< B_{yl1}$ or $> B_{yl2}$, the measured atomic response cannot be reliably used to extract magnetic field information.

The gradient of the linear region provides the measured response (mV) to detected field (nT) conversion factor (χ) in mV/nT.

$$\chi = \frac{\delta A_{\text{Demod}}}{\delta B_y} \ , \tag{2.47}$$

where δA_{Demod} is the change in amplitude of the demodulated response and δB_y is the change in magnetic field, across the linear response region.

A steep demodulated gradient means very small fields produce a large voltage response which translates to a more sensitive magnetometer. The dispersive response and linear region are defined by the resonance width of the atoms, modulation amplitude and modulation frequency. Efforts to increase the gradient (such as optimising for the narrowest magnetic resonance) can reduce the boundaries of the demodulated linear region, and consequently the dynamic range.

The presence of any extraneous magnetic fields, B_{ex}, greater than the boundaries of the dynamic range ($B_{ex} > |B_{yl1}|$ or $B_{ex} > |B_{yl2}|$) will produce a non-linear amplitude response with respect to the field. As such, the extraneous fields present across the OPM must be kept as low as possible, or be managed through active closed-loop feedback.

2.6.6 SERF sensitivity

The fundamental sensitivity limit, δB_0, of a SERF magnetometer is defined as [28];

$$\delta B_0 = \frac{1}{\gamma\sqrt{\rho T_2 V t}} \ , \tag{2.48}$$

where ρ is the atomic density, V is the cell volume and t measurement time.

Experimentally, the sensitivity of the sensor is directly extracted from the sensor response which also includes all magnetic and electrical noise contributions. The sensitivity is measured after zero-field has been established across the atomic ensemble (through application of B_{x0}, B_{y0} and B_{z0}). The sensor noise floor and therefore sensitivity is characterised through a "free-running" measurement, achieved through monitoring the atomic response for a set measurement time, t, whilst the atoms are magnetically modulated across an axis orthogonal to the beam axis. Analysis of the free running measurement through the square root of the power spectral density

(PSD) provides amplitude response as a function of frequency. The $\sqrt{\text{PSD}}$ scaled by the measured demodulated gradient (Equation (2.47)) constitutes the magnetometer noise floor with magnetic field as a function of frequency.

The sensitivity, as a single figure of merit, is calculated across a selected frequency band of interest through the geometric mean. The use of the geometric mean is more appropriate than the arithmetic mean as the geometric mean is less susceptible to the influence of stochastic noise that manifests as positive peaks in the $\sqrt{\text{PSD}}$. Measured sensitivity, δB_1, is therefore expressed as;

$$\delta B_1 = \left(\prod_{f_{\text{Min}} \leq k \leq f_{\text{Max}}}^{n} \frac{\delta A_{\text{Demod}}}{\delta B_y} X(k) \right)^{\frac{1}{n}}, \tag{2.49}$$

where f_{Min} minimum and f_{Max}maximum frequencies define the frequency band of interest.

Chapter 3

SERF experimental setup

This section will detail the systems and components that are required to create a single beam SERF magnetometer. The specific laboratory-scale components used for the caesium SERF magnetometer presented in thesis will be discussed. The operational procedure of the caesium SERF magnetometer will also be explored, including description of how the user controls the magnetometer, collection of data and the measurement scheme required to ensure fast calibration to a zero-field environment throughout all testing.

3.1 Caesium SERF magnetometer setup

To aid system discussions in later sections, we will first describe the single-beam SERF OPM from a high-level perspective. In single beam magnetometry a single laser source, tuned to the wavelength of the appropriate atomic transition, is utilised to both pump and probe the atomic ensemble [51, 60]. The beam simultaneous optically pumps the atoms into a desired state of polarisation and probes the atomic response to a magnetic field. Two-beam setups with separate pump and probe laser sources are also common [30, 61, 62] that allow for individual adjustment of pump and probe beams to provide optimal pumping and probing efficiency with minimised pump beam noise. However, single-beam systems are only explored in this thesis, due to simplicity of construction with the view to aid miniaturisation of the system.

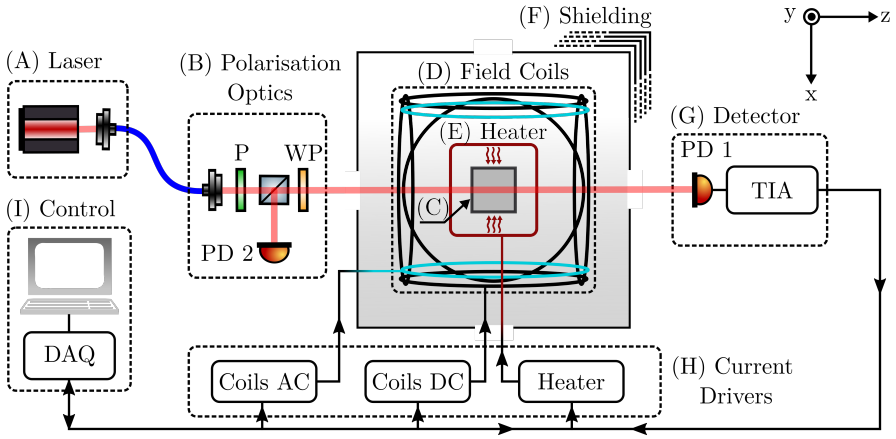

Figure 3.1: Generic SERF OPM topology showing essential components and systems

The caesium SERF magnetometer presented here uses a distributed Bragg reflector (DBR) laser resonant with the caesium D_1 ($F = 4 \rightarrow F' = 3$) transition at 895 nm in the interest of miniaturising the sensor for portability. The D_1 line is selected due to its superior optical pumping efficiency [38]. The single beam setup is less complex in terms of hardware and benefits microfabricated cells with a single axis of optical access due to the silicone frame. The DBR laser optically pumps the atomic ensemble into a dark state, leading to decreased transmission of light through the cell. A quarter waveplate, $\lambda/4$, elliptically polarises the light before it is incident on the atomic vapour cell for optimal polarisation [57].

In this section the specific hardware, control and calibration of the laboratory-scale components required for the caesium (Cs) SERF magnetometer setup are discussed. Components developed specifically for the portable sensor package, including a miniaturised rotation mount for a waveplate and coil design, will be discussed in further in Chapter 5. The general architecture of a single beam SERF magnetometer is illustrated in Figure 3.1. The essential systems of a SERF magnetometer can be summarised as below, with reference to the corresponding components labelled in Figure 3.1:

(A) **Pump and probe laser source**:

The power and wavelength of the DBR laser is tunable by the laser current

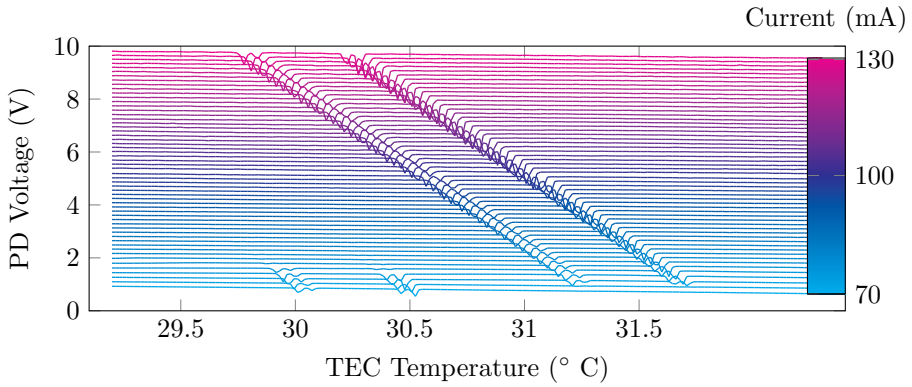

Figure 3.2: Laser calibration. Spectroscopy taken by sweeping the TEC temperature, across the full range of laser current available. The measured photodector (PD) voltage for a range of laser currents (mA) with respect to TEC temperature

and temperature. A digital butterfly laser diode controller (Koheron CTL200) provides direct control of the laser current and thermoelectric cooler (TEC) temperature. The effects of changing the TEC temperature and laser current are entwined, but can be calibrated to provide direct control of laser power and frequency.

Frequency calibration is realised through repeated measurement of a reference cell that is typically only Doppler broadened that allows for clear identification of the four expected optical peaks. Figure 3.2 shows the measured absorption spectra of a caesium reference cell (Thorlabs GC25075-CS) found by sweeping the TEC temperature. Identification of the $F = 3$ peak is used for calibration such that the temperature and current set on the laser controller produces the same frequency response, where 0 GHz corresponds to the $F = 4 \rightarrow F' = 3$ transition. By mapping the full range of current and TEC temperature available it can be seen in Figure 3.2 that at ~ 72.05 mA the laser exhibits a sudden jump in wavelength due to a mode hop between different modes of the laser.

Laser current (mA) to laser power (mW) is calibrated through iterative measurement using a power meter. Full calibration is defined in Appendix A.

(B) **Optics**:

Optics are required to set the polarisation of the light before interrogating the atomic ensemble. For the caesium SERF magnetometer the light is elliptically polarised, for optimal polarisation [57] (Section 2.3), using a quarter waveplate, $\lambda/4$, to enable optical pumping of the atomic ensemble into the dark state to facilitate sensing.

(C) **Atomic vapour cell**:

Atomic vapour cells can vary in size and shape, from small MEMS cells [63–65] to larger glass blown cylindrical cells [66–68]. The selection of the atomic vapour cell is based on the application and considerations that largely impact the atomic response, such as buffer gas, aperture diameter and optical path length. The caesium SERF magnetometer uses a MEMS fabricated silicon cell with external dimensions of $10 \times 10 \times 4$ mm^3, featuring a 3 mm optical path length and a 6×6 mm^2 optical aperture enclosed between two layers of borofloat glass (0.5 mm thickness), seen in Figure 3.3. The cell is filled with a caesium and nitrogen vapour, achieved through the deposition of droplets of caesium azide (CsN) in the vapour cell prior to the final glass bond in a nitrogen environment. The caesium azide is then dissociated using ultraviolet (UV), resulting in the presence of caesium and nitrogen, which minimises the rate of wall collisions and prolongs the lifetime of the atomic coherences [69].

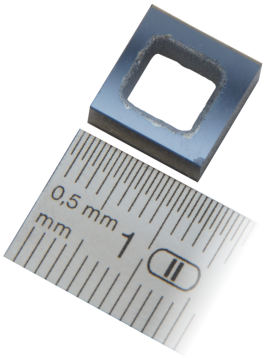

Figure 3.3: Photograph of the caesium MEMS atomic vapour cell

(D) **Magnetic field control**:

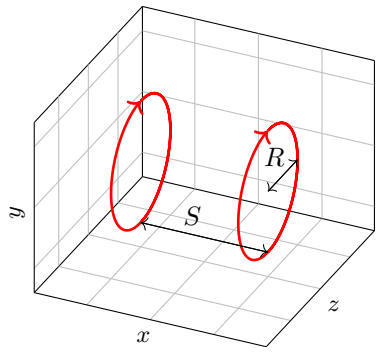

Figure 3.4: Current loop direction and geometry for circular Helmholtz coils, indicating the separation, S, and radius, R, of the coils.

A combination of coils are required across all axes to compensate for any residual magnetic fields across the magnetometer. The coils assist in providing a zero-field environment to maintain SERF regime operation. Magnetic modulation is also required to enable sensing along the $y-$axis as discussed in Section 2.6.5. Typical coil configurations include Helmholtz [70] and saddle coils [71], however implementation of customised novel coil geometries have also found success [72–74]. The important consideration for coil design include the produced magnetic field homogeneity and current noise.

A Helmholtz coil configuration is a commonly utilised design in magnetometry applications due to its ability to generate a region of nearly uniform magnetic field which can be simply and reliably calculated. This configuration consists of two circular coils with radius, R and each wound N times with equal electric current flowing in the same direction. A Helmholtz-like configuration is seen in Figure 3.4, where the coils are separated by the free parameters of distance, S. The resulting on-axis magnetic field, denoted as B_{HH}, for circular geometry Helmholtz coils can be described by the following equation, derived from the Biot-Savart law [75, 76].

$$B_{\mathrm{HH}} = \frac{\mu_0 N I R^2}{2} \left(\frac{1}{\left(\left(D + \frac{s}{2}\right) + R^2\right)^{\frac{3}{2}}} + \frac{1}{\left(\left(D - \frac{s}{2}\right) + R^2\right)^{\frac{3}{2}}} \right) , \tag{3.1}$$

where D is the distance of the measured field value from the coils. Other ge-

ometries of Helmholtz-like coils can be utilised, in a similar symmetrical configuration, with the geometry specific resultant on-axis magnetic fields found similarly, including square [77, 78] and equilateral triangular [79] coil geometries.

Portable scale microfabricated coil design and construction is discussed in the portable sensor chapter (Chapter 5).

(E) **Cell heating**:

The caesium MEMS atomic vapour cell must be heated to $\simeq 120$ °C to reach an atomic density of $\simeq 10^{14}$ cm^{-3} for SERF regime magnetometry, as discussed in Section 2.6.1. Heating through methods that do not produce a magnetic field that the sensor can detect are preferred such as heating laser sources [80], or ohmic heating using alternating currents (ACs) [31]. Here, ohmic electrical heating is realised through use of a heating resistor, as discussed in detail in Section 3.2.1.

Heating currents, provided through a custom heater driver, are digitally user-selectable and automatically controlled to maintain stability during any measurements through closed-loop control. The full heating system, including heater driver, temperature monitor and automatic controller are discussed in greater detail in Section 3.2.

(F) **Magnetic shielding**:

Magnetic shielding and static field compensation is necessary to keep the atomic ensemble in a zero-field environment. Magnetic shielding directs the external magnetic flux around the shielded area using high-permeability ferromagnetic material with high nickel content such as mu-metal [81]. The shielding ratio, ζ, defines the efficiency of the shielding in terms of the magnetic field outside the shielding and the field induced inside the shielding B_{in} due to B_0, where:

$$\zeta = \frac{B_{in}}{B_0} \ . \tag{3.2}$$

Here in the laboratory setting magnetic shielding is provided by five lay-

ers of mu-metal magnetic shielding with a shielding factor of $\zeta \simeq 10^5$. The shielding maintains a low nT-level magnetic field environment through the attenuation of external magnetic fields. To negate the effect of the residual magnetization of the innermost shielding layer, the shielding is demagnetised through degaussing. Degaussing is achieved through application of a slowly decaying alternative current to degaussing coils around the shielding [82].

(G) **Photodetector**:

A photodiode (OSRAM, SFH 206 K), labelled PD 1 in Figure 3.1, with a large active area of 7.02 mm^2 measures light transmitted through the vapour cell which varies in relation to the applied magnetic field. The photodiode current with a responsivity of 620 mA/W, is amplified by a custom transimpedence amplifier (TIA) with a gain of 5000 Ω which produces measured signals in the $\pm$10 V range. Differential detection through use of a second monitor photodiode (where typically light is picked off before the polarisation optics) as shown in Figure 3.1 labelled PD 2, can be used to cancel common mode laser noise to improve sensitivity [51].

(H) **Low-noise current drivers**:

Electronics drivers are required to provide current to the field coils and heating system for ohmic heating.

Coil driver: To compensate for the residual fields inside the magnetic shield, currents are applied to the coils on each axis. It is crucial to ensure these currents do not introduce excess magnetic field noise that could degrade the sensor's sensitivity. The static field coils are driven using an ultra-low noise programmable current source system with a narrow $1/f$ noise bandwidth of 1 Hz [83]. The current source, described here as the coil driver, has a bi-directional current range of $\pm$192 mA on three independent channels with 16-bit resolution. The current noise on this driver is in the nA regime, leading to a maximum of 37 $fT/\sqrt{Hz}$ contribution in magnetic noise (for a 1 μT applied field) for the specific coils within the caesium SERF magnetometer. The

desired coil magnetic field value is provided digitally to the custom coil driver through serial connection. The coil driver internally converts the digital signal to an analogue low-noise current [83]. A restraint exists that limits the speed at which the coil driver can be addressed which is important when considering measurement time, discussed more is Section 3.3.

Heater driver: The noise of any heater currents is of great importance due to proximity of the heater to the atomic vapour cell. To reduce the effect of current noise on the noise floor of the sensor alternating currents are preferred, as the net effect of the current across the atoms averages to effectively zero. The frequency of the heating currents should be selected far outside the region of interest of the OPM (≥ 1 kHz) [57]. A $\simeq 275$ kHz AC is used here for heating provided by a custom high efficiency heater driver, described in Section 3.2.2.

(I) **Data acquisition and control**:

To digitally interface with the system, control appropriate electronics and collect data, a data acquisition system (DAQ) is utilised. The measured photodetector signal is digitised via a 16-bit data acquisition system (National Instruments NI USB-6366). The DAQ records data at 1 MHz sample frequency. The data can be down-sampled in post-processing for analysis if required.

3.2 Closed-loop cell heating

An important process in successful operation of an OPM in the SERF regime is reaching and maintaining the required atomic density of the sensing alkali, as discussed in Section 2.6.1. The cell temperature required for the caesium OPM is $\simeq 120$ °C which must be reached quickly, and maintained to ± 0.5 °C level accuracy throughout any OPM measurements. These cell heating requirements introduce a number of operational challenges which in practicality facilitate the need for a full closed-loop cell heating system. The simplified topology for a full closed-loop cell heating system is illustrated in Figure 3.5, which consists of a number of custom designed subsystems. An overview of how these heating subsystems interface, in

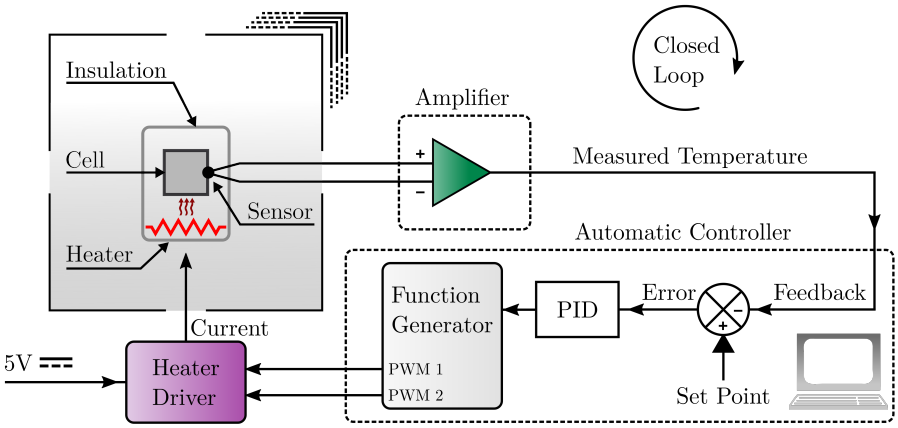

Figure 3.5: Simplified topology of the closed-loop cell heating system. A custom heater driver, powered by two PWM wave-forms from a function generator, produces a low noise and efficient heating current. The heating resistor, driven by the heater current, heats the atomic vapour cells bottom face. A temperature sensor, attached to the top face of the atomic vapour cell, measures current cell temperature. A custom temperature monitoring system accurately amplifies and calibrates the measured temperature value. The deviation of the measured temperature from a set point temperature is input to an automatic proportional–integral–derivative (PID) controller. The controller adjusts the driving wave-forms from the function generator, to correct for the temperature deviation, in a closed-loop process.

a closed-loop system, to maintain cell temperature at a user-defined set point, is summarised below.

Firstly, a custom heater driver, as will be described in more detail in Section 3.2.2, driven by two pulse-width modulation (PWM) wave-forms from a function generator, generates a low noise heating current with high efficiency. A heating resistor, as described in Section 3.2.1, is driven by the heater current which in turn directly heats the bottom face of the atomic vapour cell. The temperature of the cell is measured through a custom designed temperature monitoring system, which will be discussed in Section 3.2.3. The temperature monitoring is realised through amplification of the output of a non-magnetic temperature sensor attached to the top face of the atomic vapour cell. The deviation of the measured temperature to the user input specified set point temperature, is provided to an automatic PID controller. The controller in turn calculates the correct driving wave-forms to correct for the temperature deviation, interfacing with the function generator directly, to

provide stabilised heating control in a closed-loop process. The automatic controller and stabilised heating control process will be discussed in Section 3.2.4. In operation, the combination of these subsystems allow for digital selection of a cell temperature, the temperature is reached quickly (minutes scale), and automatically maintained throughout all measurements without any further user input required.

3.2.1 Cell heating

Ohmic electrical heating is achieved with an AC signal (at $\simeq$ 275 kHz) passed through a heating resistor. An aluminum nitride non-magnetic thin-film resistor (PN: PCNM2512K8R20FST5), is thermally bonded using boron nitride paste to an edge of the atomic vapour cell surface, as seen in Figure 3.6. The heating resistor covers a total heating surface area of 20.2 mm^2 equating to 67% coverage of the MEMS cell bottom-edge surface and resulting in rapid heating.

The MEMS cell is further packaged in a heating assembly that includes insulation and a cell mount produced in temperature resistant materials. Full description of the heating assembly can be found in Chapter 5. Furthermore, cell heating through this method results in minimal thermal gradients across the MEMS cell, as discussed in Section 5.3.

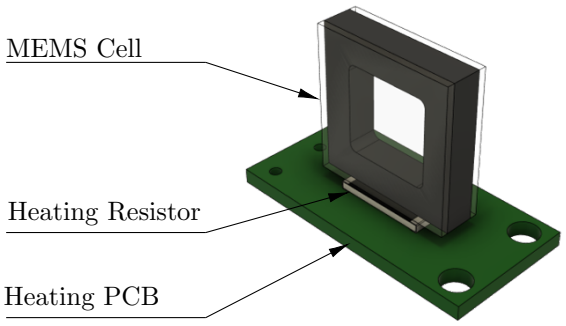

Figure 3.6: Model of the PCB mounted heating resistor in contact with the caesium MEMS atomic vapour cell. The heating resistor is bonded to an edge of the MEMS with boron nitride paste.

3.2.2 AC heater driver

Cell heating is achieved through ohmic heating of a resistor thermally connected to the atomic vapour cell. An AC method for heating the cell at high efficiency is not readily available through off the shelf control devices. Here, high efficiency heating is particularly important for reducing power consumption as the sensor and control electronics will be portable. This section will describe the design of an efficient and controllable AC source used for the magnetometer's cell heating.

Initially, we assumed audio amplifiers would be suitable for the purpose of providing AC for cell heating. However, the use of commercial off-the-shelf audio amplifiers results in low efficiency heating due to power losses across the amplifier circuit. The power efficiency of a typical low distortion audio power amplifier (NCS2211) was measured at 300 kHz (far outside the bandwidth of the SERF magnetometer), at around 1 W (desired output power), for an 8 Ω resistive load, such that the audio amplifier was calculated to be $\simeq$60% efficient. The amplifier maximum power is also capped at 1.5 W, which would not provide enough power to adequately heat the atomic vapour cell to 120 °C. To improve power efficiency and cell heating, an amplifier with less power loss is required.

In this thesis, a custom heater design for a SERF magnetometer is proposed. The new design improves upon the limitations of commercial off-the-shelf amplifiers by increasing efficiency ($\geq$ 60%) and providing more precise control over the heating process. The new design uses a H-bridge amplification scheme to reach a superior efficiency of >90 % at the desired output power range, $\simeq 1 - 2$ W.

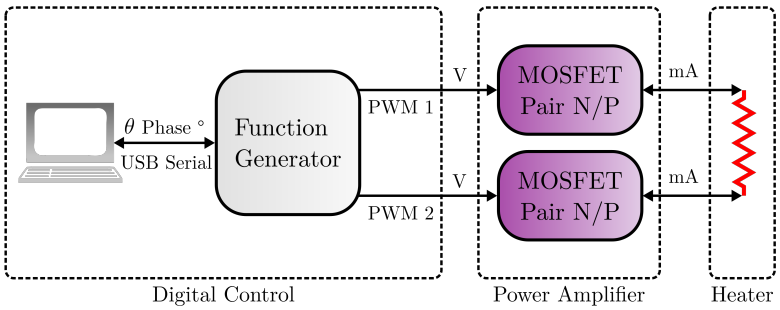

Figure 3.7: Simplified architecture of the heater driver. Three steps are indicated. Digital control; using USB serial to interface from the computer to a function generator, which in turn drives the selection of two driving waveforms, PWM 1 and PWM 2. Power amplifier; voltage is provided to two metal–oxide–semiconductor field-effect transistor (MOSFET) pairs and amplified. Heater; Amplified current is provided to the heating resistor, indicated in red.

The efficient heater driver system architecture can be simplified into three main steps as shown in Figure 3.7. These steps include: 1) heating, 2) power amplification and 3) digital control .

1. Heating:

   A heater element is bidirectionally driven by current provided by the power amplifier. Bi-directionality allows for the net direct current and subsequent time average of the magnetic field experienced by the atoms to be zero by ensuring current flow in each direction is equally driven.

2. Power Amplification:

   Power amplification is achieved through a MOSFET H-bridge circuit, powered by a single 5 V supply, and controlled by two PWM wave-forms. PWM wave-forms are utilised as the magnitude of the current flowing in both the positive and negative directions is the same, which eliminates the need for dynamically adjusting or trimming the amplitudes of the waveform during operation. The amount of current driven to the heating resistor is controlled by the phase offset, θ, between the two driving PWMs. The smaller the phase offset, the more power is delivered through heating (Figure 3.10). The H-bridge Amplifier is a circuit configuration that consists of 4 MOSFETs (Q1, Q2, Q3 and Q4),

configured as two pairs on two sides, labeled as A and B side in Figure 3.8. The net zero direct current (DC) is maintained by AC-coupling the driving current through capacitors $C1$ and $C2$, where the capacitor values are tuned using the high pass transfer function, Equation (3.3).

$$f_c = \frac{1}{2\pi RC} \ , \tag{3.3}$$

where the cutoff frequency, f_c, in this application is in the 10's of kHz scale.

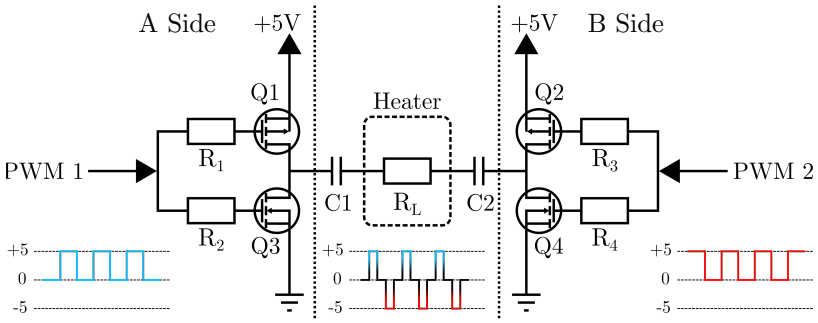

Figure 3.8: Simplified schematic of the heater driver H-Bridge. The H-bridge Amplifier consists of 4 MOSFETs (Q1, Q2, Q3 and Q4), configured as two pairs on two sides, labeled A and B side

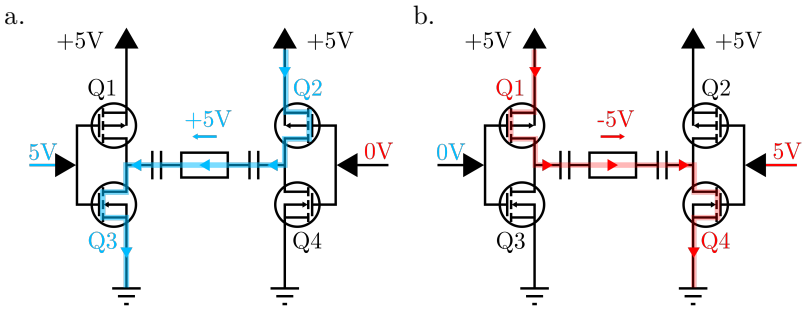

Figure 3.9: The heater driver H-bridge amplifier current flow demonstration. **a)** Positive flow, turning on Q2 and Q3. **b)** Negative flow, turning on Q1 and Q4

The direction of current flow is determined by how the MOSFETs are engaged. Both MOSFET pairs from the same side must not be turned on at the same time as it will create a 'shoot-through' condition by shorting the power supply to ground. The current is bi-directionally controlled in 3 states:

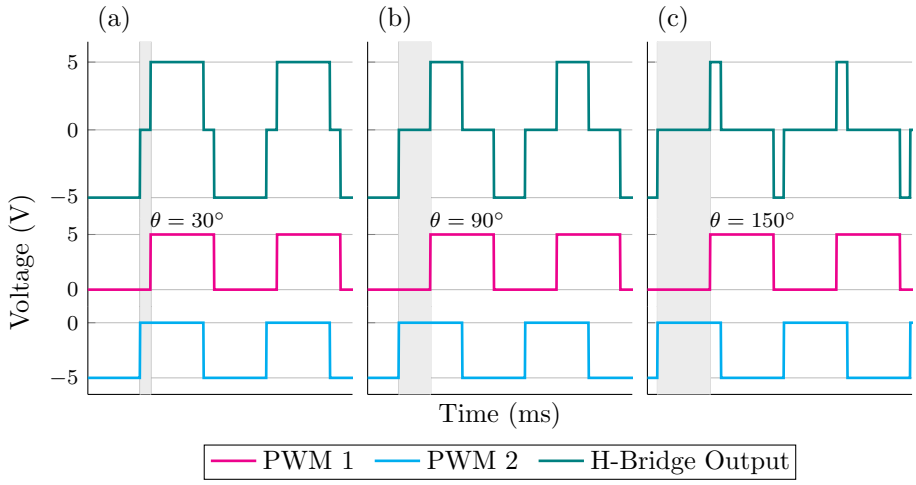

Figure 3.10: H-bridge Output of two PWMs (PWM 1 and PWM2) with varying degrees of offset θ between PWMs. Full H-bridge output power is achieved at $\theta = 180\ ^\circ$, null power is achieved at $\theta = 0\ ^\circ$. **a)** $\theta = 30\ ^\circ$, **b)** $\theta = 90\ ^\circ$ and **c)** $\theta = 150\ ^\circ$

(a) **No current flow**, all MOSFETs closed.

(b) **Positive flow**, turning on Q2 and Q3. Current flows right to left, as seen in Figure 3.9(a) indicated by blue arrows.

(c) **Negative flow**, turning on Q1 and Q4. Current flows left to right, as seen in Figure. 3.9(b) indicated by red arrows.

Current is always driven equally in the positive and negative directions. The power delivered to the heating element is determined by the amount of time with no current flow, which is controlled through the phase offset between the two driving PWMs. One driving input PWM must be inverted to introduce a dead time and protect same side MOSFETs from engaging simultaneously. The full H-bridge is differential in nature, meaning it can deliver twice the output signal (5 V to -5 V) and four times the output power of single-ended implementations.

3. Digital Control:

   Desired temperature is selected by the user through a custom program created in LabVIEW. Temperature is converted to PWM offset θ (from prior

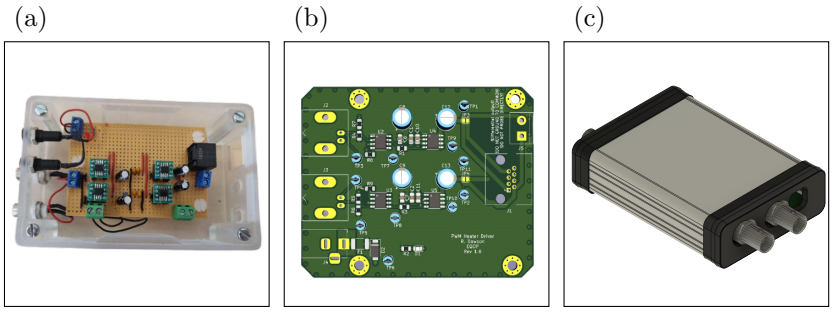

Figure 3.11: High efficiency heater driver: **a)** Prototype stripboard version, **b)** printed circuit board (PCB) design, **c)** computer aided design (CAD) drawing of the external casing and BNC connectors

calibration) and sent to a function generator through USB serial. The function generator creates two PWMs of equal frequency, amplitude, and duty cycle, with an offset in one of the PWMs as specified, seen in Figure 3.10. The resolution of the PWM phase offset is such that mA level of current control is achievable that provides m°C level temperature control of the heating resistor.

The efficient heater driver design was first built and tested on a strip board (Figure 3.11(a)) and then refined on a PCB (Figure 3.11(b & c)).

Figure 3.12 demonstrates the power efficiency of the efficient heater with respect to output power, and shows that the heater is over 90 % efficient within the desired output power range, $\simeq 1 - 2$ W. In practicality there is some deviation from the ideal wave-form seen in Figure 3.10, which can skew the applied current causing net average to deviate from zero. The measured cycle-averaged DC across the heater at maximum power delivery (2.5 W) is measured at 0.3 A, which is sufficiently small that a resultant B-field is not measurable across the atoms. Maximum current delivery is also not required during sensor operation during measurement.

The heater driver power output, typically within the range of 1-2.5 W, varies depending on operation and desired cell temperature. During the initial warming of the cell, to reach the set temperature, the heater driver provides $\simeq$ 450 mA, delivering $\simeq$ 2.5 W at $\simeq$ 97 % efficiency. At steady-state heating, maintaining a temperature of 120 °C, the heater driver provides $\simeq$ 250 mA, delivering $\simeq$ 1.25 W at $\simeq$ 95 % efficiency.

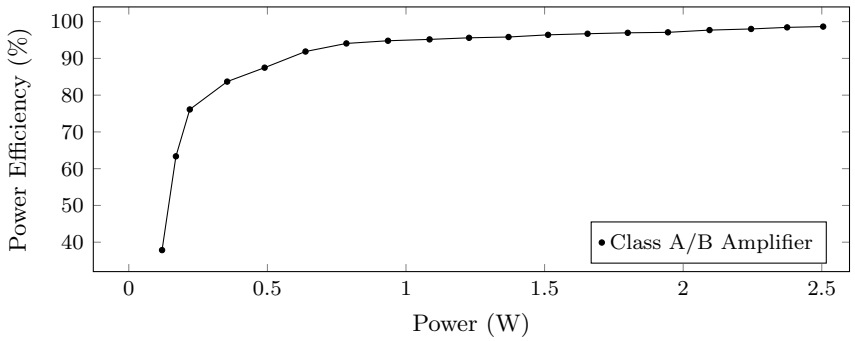

Figure 3.12: Power efficiency, of the new high efficiency heater driver, calculated from the measured heater driver power output with respect to the expected output.

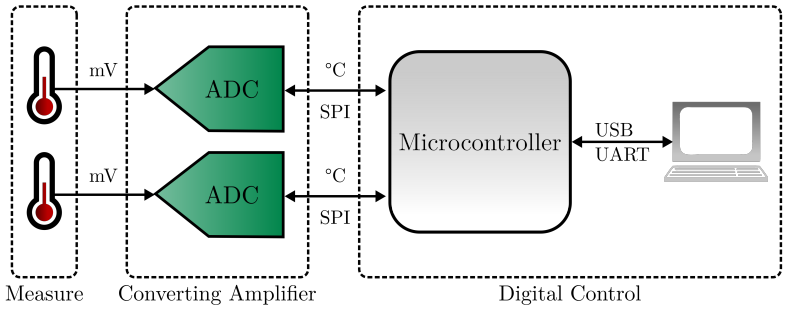

Figure 3.13: Simplified architecture of the temperature measurement system for two-channel independent temperature measurements.

3.2.3 Temperature monitoring

Temperature monitoring of the atomic vapour cell is important for closed-loop temperature control to maintain a steady temperature. However, the chosen measurement method can introduce magnetic fields in the sensing region of the sensor. It is important to minimise the introduction of any magnetic fields through the selection of non-magnetic measurement components. Thermocouples produce a very low DC voltage (mV level) and can be manufactured from non-magnetic materials (such as T-Type theromocouples [84]), making them well-suited for use in sensitive magnetometry applications and for this reason we will make use of them in the project. The cell temperature of the caesium SERF magnetometer is measured using the following scheme.

Figure 3.13 illustrates the simplified architecture for a 2-channel measurement

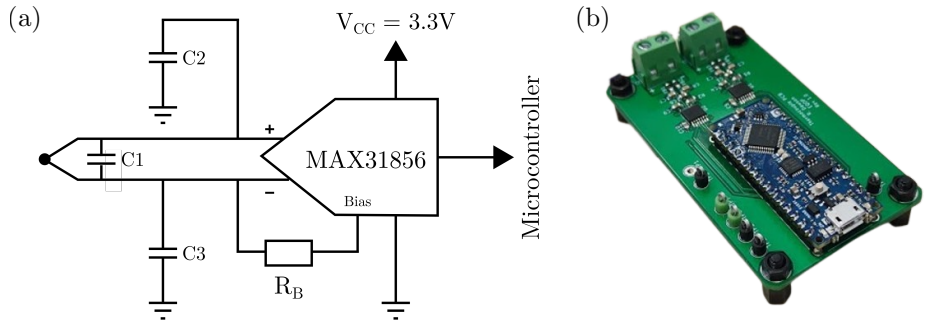

Figure 3.14: a) Simplified schematic of thermocouple conversion and amplification. b) PCB temperature monitoring system for the two-channel system showing the analogue circuitry, ADC, and microcontroller

system, where measurements are taken through two T-type thermocouples. The voltages produced by the thermocouples are amplified and converted through an analog-to-digital converter (ADC) and accessed by the user through digital control, achieved with a microcontroller interfacing to the control computer through Universal asynchronous receiver-transmitter (UART).

Figure 3.14(a) shows a simplified schematic of a temperature monitor that uses a MAX31856 as the ADC. The MAX31856 is a temperature monitor converter and amplifier specifically for thermocouple temperature sensors. The MAX31856 digitises the signal from a thermocouple between -63.15 to 2073.15 K with ±0.4 K accuracy. The conversion uses a lookup table for linearity correction. Additionally, to set the sensor voltage DC operating point a bias is applied within the MAX31856 circuit; this is shown in Figure 3.14(a), as R_B. To increase the robustness of the design by minimising the number of thermocouple connections, the design is produced on the PCB seen in Figure 3.14(b). The 2-channel design allows for simultaneous recording of 2 individual thermocouples, for example to measure different points across an atomic vapour cell (top and bottom) to indicate any temperature gradients.

3.2.4 Stabilised heating control

This section will discuss automatic heating control for rapid cell heating in the caesium SERF magnetometer. PID controllers are widely utilised in heating systems due to high levels of stability, precision, and response time. Here, a LabVIEW based

PID is utilised that interfaces to the SERF magnetometer through USB serial. The PID allows for user input of the set temperature and calculates heating error between the measured and set temperatures, forming a feedback loop with the OPM. The heating error informs phase offset (θ), Section 3.2.2, configurations sent to the heater driver via the function generator.

Whilst simple to implement, the parameters for the PID controller need to be tuned for each new complete system – controller plus device. The tuning process involves adjusting three governing parameters: proportional, integral, and derivative gains. Through careful selection of these gains, the system response can be controlled. Metrics to define system response include:

- Rise time: The time taken to reach the set temperature.
- Overshoot: Heating above the set temperature.
- Settling time: The time taken to stop oscillating around the set temperature.
- Steady state error: The deviation from the set temperature.

Figure 3.15 demonstrates the outcome of manually tuning a PID controller to reach a set temperature of 120 °C, from a starting temperature of ≃85 °C, where PID_1 to PID_8 refer to iterative tuned configurations of the PID controller gain values. The optimal PID configuration for the heater was determined to include the proportional and integral terms, whilst excluding the derivative term. The proportional gain is the most critical parameter, largely controlling the overshoot and dampening of the heating response. The integral gain helps to eliminate steady-state error. Excluding the differential term prevents instability caused by hysteresis-induced delays and non-linear responses.

The goal of PID tuning is to achieve a critically damped response, where heating is neither too slow nor too oscillatory, and reaches the set point without overshooting. This is considered the ideal state for a PID controller, as it allows for a fast response to changes in temperature while still maintaining stability. This has been achieved with tuning configuration PID_6, as shown in Figure 3.15 inset graph. Configurations

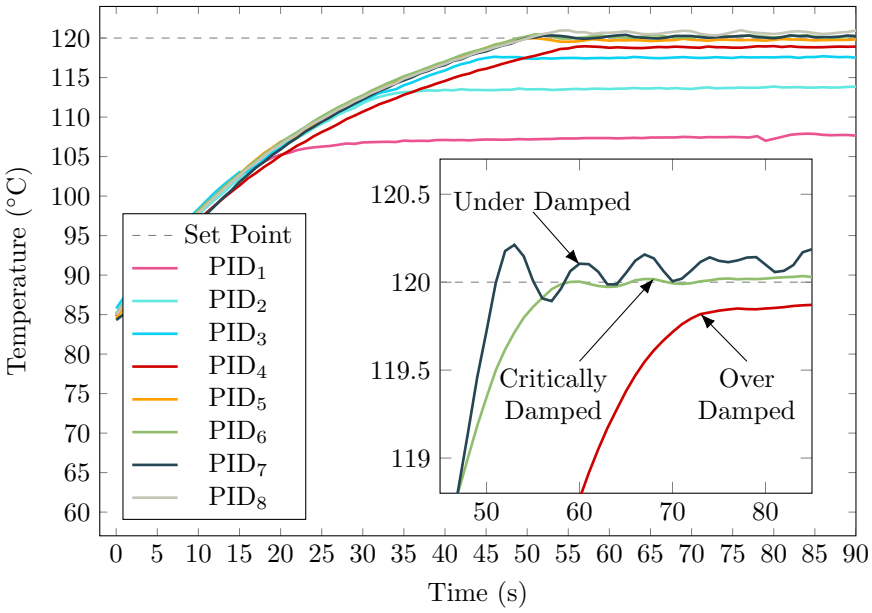

Figure 3.15: Tuning PID to defined set point of 120 °C. Various configurations of PID settings are tested from a starting temperature of ≃85 °C, denoted as PID_1 to PID_8. The inset shows three configurations that demonstrate over damping, under damping and critical damping, as indicated.

of the system that are under damped (PID_7) are characterised by fast overshoot and oscillation, while configurations that are over damped (PID_4) are characterised by slow response and large steady-state error.

During operation of the SERF magnetometer, the goal is to reach and stabilise at set-temperature as quickly as possible. Whilst it is important to quickly reach the desired temperature, unfortunately, during operation we see an effect of the rapidly changing PWM phase manifesting as noise in the measured signal. Investigations to the cause of this noise have not been able to fully remove it. We know the heater driver does not apply any DC, or subsequent magnetic field, to the system during operation of the PID and we only apply PWM phase changes in multiples of full cycles of the PWM, however the noise still effects the signal. It is possible that quickly addressing the heater driver with the same computer is introducing small amounts of noise into the measured detector signal. Regardless of the cause, during long measurements the PID cannot run, and a constant value for the heater phase must be applied, to ensure no noise from the PID is added to the signal. As such, the

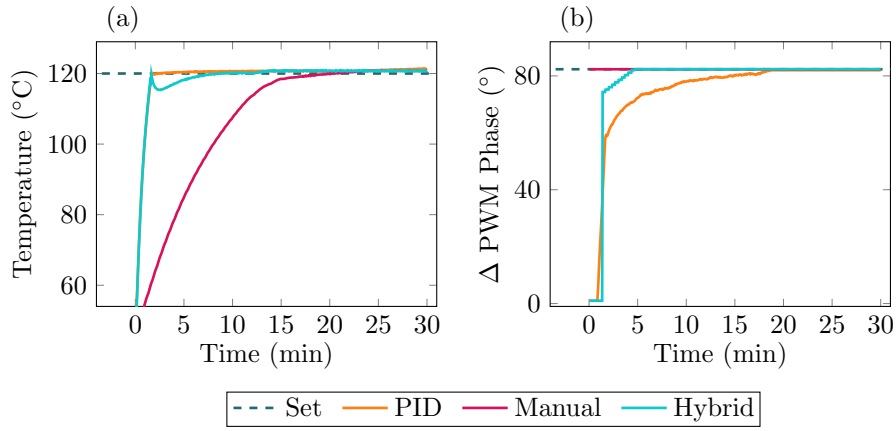

Figure 3.16: Comparison of three heating control techniques, 1) PID, 2) Manual, which set the phase to a pre-defined value, 3) Hydrid approach. **a)**, Measured temperature of the atomic vapour cell for each heating control method. The dashed line indicates the target temperature. **b)** The applied PWM phase offset, ΔPWM, sent to the heater driver during each method, where maximum heating is delivered at $\Delta\text{PWM} = 0$. The dashed line indicates the target phase

optimal state of heating is reached when a constant phase offset is applied, which only occurs once the vapour cell has saturated in temperature. There is a trade off between the time needed to reach either stable temperature or the PWM phase offset, which will be investigated next.

Here saturation time for cell heating and PWM phase will be explored to understand operation methodology to balance temperature and PWM phase stabalisation, by understanding three heating schemes: 1) Manual, 2) PID and 3) Hybrid.

1. **Manual**

   Implementing the calibration of PWM phase to temperature value (Equation (A.3), the phase value for a required temperature can be set manually, seen in Figure 3.16(b). Cell temperature will slowly rise and saturate at set-temperature in approximately 20 minutes. For the manual technique, the target phase is reached immediately but the system drifts from target temperature for a long time.

2. **PID**

   A PID quickly reaches the set-temperature ($\leq$ 2 minutes), Figure 3.16(a), by

using a very low PWM phase value to provide large heating currents. However, once the required temperature is reached, the phase offset value slowly saturates over the course of 20 minutes 3.16(a). For the PID technique, the target temperature is reached immediately but the system drifts from target phase for a long time.

3. **Hybrid**

   Here, a third scheme is explored with the goal of reaching temperature quickly and reaching stable PWM offset quickly. This scheme, denoted in Figure 3.16 as "Hybrid" uses the quick heating methodology of the PID, and the stable PWM methodology of manual heating, with a period of ramping the PWM phase to the pre-calculated desired value over a course of 5 minutes. This ramping period reduces the time needed to saturate at set-temperature to around 10 minutes, 3.16(a) (teal line). Similarly, the time needed to reach stable PWM phase in the hybrid scheme is also reduced in comparison to the PWM, at around 5 minutes 3.16(b) (teal line).

3.3 Caesium SERF magnetometer procedure

In order to measure a field of interest there are a number of procedures that must be completed. The operational and experimental procedures for using the caesium SERF magnetometer will be described in this section. This includes activities to ready the sensor for data collection, preparation and maintenance of a zero-field environment and the data collection methods employed to extract external magnetic field information.

The full experimental procedure for using the caesium SERF magnetometer is illustrated by the flow diagram in Figure 3.17, with examples of important graphical outputs shown for certain processes to the left indicated by grey arrows. The caesium SERF magnetometer experimental procedure can be summarised as follows, with reference to corresponding system labelled in Figure 3.17:

(1) **Set operational parameters:**

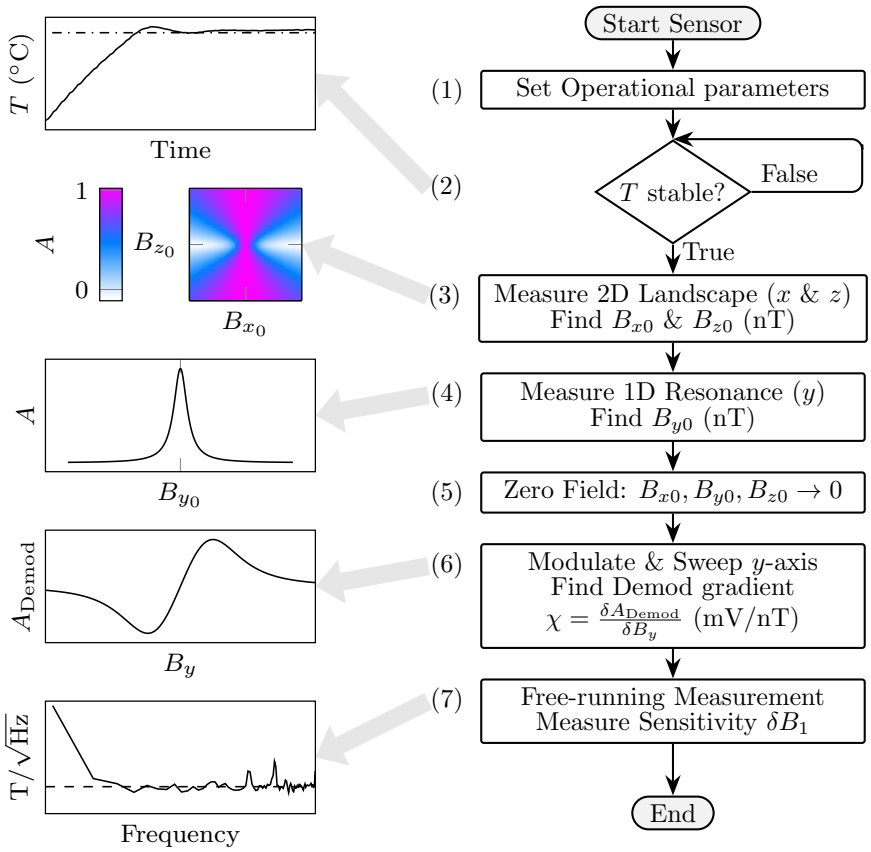

Figure 3.17: The SERF Magnetometer operational procedure, including all steps for operating the magnetometer. The expected results at each stage are indicated by corresponding graphs, as shown by the grey arrows.

Here we classify the sensors key operational parameters as; 1) laser power (mW), laser frequency (GHz) and cell temperature (°C). The values of these parameters are independently optimised for performance, as discussed in more detail later (Chapter 4). To ready the sensor for data collection, the operational parameters are digitally selected using the calibration parameters in Appendix A.

(2) **Reach stable temperature:**

Before any data can be collected, the temperature of the cell must reach the desired temperature, T_{Set}, and stabilise consistently at this value such that measured cell temperature $T = T_{\text{Set}} \pm 0.5$ °C. The time taken to heat the cell into a stable state far exceeds the time taken to complete any other process that is required to use the magnetometer. To minimise the heating time I implement automatic heating control. The procedure for the automatic heating control is discussed in Section 3.2.4.

(3) **Measure 2D landscape:**

The 2D landscape, as described in Section 2.6.4, allows for identification of the zero-field magnetic field values across two axes. In this case, the 2D landscape is measured across the $x-$ and $z-$axes, to extract the zero-field values B_{x0} and B_{z0} respectively. To apply the shifting fields required to measure the 2D landscape, the $x-$ and $z-$coils are utilised, to provide a homogeneous region of the required field B across the vapour cell. The coils are driven by the current driver, digitally selected using the calibration parameters in Appendix A.

The time taken to measure the full 2D landscape, $\simeq$100 s, is the second most time-exhaustive process for the SERF magnetometer. The time for this measurement is due to a combination of the time needed for the atoms to reach equilibrium, the restraints of the coil driver and the number of total measurements needed. A method to reduce the number of total measurements needed, to identify the zero-field values B_{x0} and B_{z0}, is proposed in the following section.

(4) **Sweep 1D on y, find B_{y_0}:**

The 1D resonance, as described in Section 2.6.3, is a transverse resonance that allows for identification of the zero-field magnetic field values across the remaining axis. In this case, the 1D resonance is measured across $y-$axis, to extract the zero-field values B_{y0}. To apply the shifting fields required to measure the 1D resonance, the $y-$coil is scanned, driven by the current driver using the conversion in Equation (A.4).

(5) **Apply zero-field across all axis:**

The remaining magnetic field across each axis are now identified as B_{x0}, B_{y0} and B_{z0}. All three zero-field values are applied to maintain zero-field across all axes.

(6) **Modulate and sweep $y-$axis:**

The magnetic field across the $y-$axis is swept, with an additional field modulation applied along the same axis at an amplitude, A_{Mod} and frequency F_{Mod}. For each value of B_y, the signal is demodulated. The gradient, χ, of the demodulated line shape provides the amplitude response A_{Demod} as a function of magnetic field B_y (as described in Section 2.6.5). Measurement of the gradient χ is important for recovering the magnitude of any magnetic fields that are subsequently applied to the atomic ensemble.

(7) **Free-running measurement:**

The sensor is used to take a free-running measurement to monitor the magnetic field in the environment of the sensor after all the remaining fields have been nulled. This measured magnetic field could be just the noise in the shield or some external magnetic field such as a biomagnetic signal. The free-running measurement is realised by monitoring the atomic response of the atoms as they are magnetically modulated on an axis orthogonal to the quantisation axis (here, we selected the y-axis). The measurement time, t, and analysis of the free-running measurement depends of the type of recovered signal that is required, specifically whether the signal is analysed in the frequency domain

or the time domain. Both types of domain are extracted from the same photodetector output which monitors atomic response as a time domain series, and it is from this that the frequency domain information is extracted. Some biomagnetic signals are observed in the frequency domain (MEG [85]) and others in the time domain (MCG). For a noise floor measurement, typically $t \simeq 1$ s and the measurement is repeated (typically 10 times) and averaged using Welch's method [86] to provide more accurate frequency domain information by reducing the effects of stochastic noise.

3.3.1 3-axis zero-field identification

In this section we will discuss the methods for identifying the zero-field magnetic field values across orthogonal axes (B_{x0} and B_{z0}) that must be applied to maintain a zero-field region across the atomic vapour cell. As discussed, an exhaustive measurement for zero-field identification is a highly time-exhaustive aspect of the magnetometers operation. This section will explore the design and implementation of a method, here named the fast zero-field technique, developed to reduce the total measurement time for identifying zero-field across two axes.

We assume the magnitude of any residual background fields falls within the range ± 1 μT. A low nT-level magnetic field environment is provided by the laboratory-based magnetic shielding as discussed in Section 3.1. When the magnetometer is taken outside the laboratory-environment for practical measurements (discussed further in Chapter 5), the sensor is housed inside a magnetically shielded room (MSR). The uniformity in a MSR has variations in the 10's of nT range [72,87,88]. By housing the sensor is the MSR or even a different location within the same MSR [89,90], we will have to cancel the residual field quickly and efficiently.

The presence of remaining static magnetic fields perpendicular to the sensitive axis cause systematic errors in the sensor that ultimately results in reduced sensor capacities [43]. If the remaining static field is larger than the dynamic range of the sensor, the sensor response is no longer linear and thus not useful for magnetometry. It is therefore very important to manage the field across the atoms to keep a zero-field

environment.

Identification of the zero-field point for orthogonal axes is aided through the existence of a narrowing in the 2D landscape, as described in Section 2.6.4. Here the transverse and longitudinal axes measured in the 2D landscape are the $x-$axis and $z-$axis respectively. The magnetic field swept across each axis is defined between selected maximum (Max) and minimum (Min) values such that the magnetic field on the $x-$axis is defined as $B_{x\mathrm{Min}} \leq B_x \leq B_{x\mathrm{Max}}$ and the magnetic field on the $z-$axis is defined as $B_{z\mathrm{Min}} \leq B_z \leq B_{z\mathrm{Max}}$. Each magnetic field range is measured by a set number of points n. The change in magnetic field between measurements ΔB_x and ΔB_z across the $x-$ and $z-$axis respectively are described as;

$$\Delta B_x = \frac{B_{x\mathrm{Max}} + |B_{x\mathrm{Min}}|}{n_x} \text{ , and} \tag{3.4}$$

$$\Delta B_z = \frac{B_{z\mathrm{Max}} + |B_{z\mathrm{Min}}|}{n_z} \text{ ,} \tag{3.5}$$

where n_x is the number of samples measured across the $x-$axis and n_z is the number of samples measured across the $z-$axis.

Experimentally, a naive method for identifying the zero-field value is through rastering across the full range of B_x and B_z in steps of ΔB_x and ΔB_z to enable fitting of the data to a single fit function (Equation (2.44)). Use of this systematic method to identify the zero-field point across each axis is an exhaustive process that requires a substantial amount of total measurement time, t_{2D}. After applying any magnetic fields the atoms require time to respond to the field and reach equilibrium. This response time varies with the amplitude and frequency of the applied field, I found experimentally waiting 20 ms ensures equilibrium response is measured for the full range of amplitudes and frequencies of magnetic fields we apply. Restraints to the speed at which the coil driver can be addressed also exist due to a mandatory wait period that allows for settling, which effectively adds another 20 ms to each measurement point. As such, a single measurement takes $\sim$40 ms, and each resonance sweep at typical resolution, $n_x = n_z = 50$, takes $\sim$2 s to measure. Accordingly, total measurement time for a 2D landscape at typical resolution is at least

100 s ($t_{2D} \geq 100$ s).

3.3.2 Simulated 2D Hanle landscapes

To test the robustness of the fast zero-field technique, a set of 2D landscapes are required where the zero-field values in each axis are known.

Simulation of a 2D landscape with known zero-field offsets is achieved again through derivation of the equation of motion for a classical magnetic dipole Equation (2.31). Here, we can model atomic response using a definition of the B-fields $\underline{B}(t)$ to incorporate two parts of the static magnetic field to be applied to each axis:

1. A static field that defines location of zero-field ($B_{x\text{Offset}}$ & $B_{z\text{Offset}}$)
2. A further static field to simulate the application of field during a transverse resonance sweep at a particular longitudinal field value, (B_x & B_z).

The applied magnetic field across all axes $\underline{B}(t)$ becomes;

$$\underline{B}(t) = \begin{pmatrix} B_x + B_{x\text{Offset}} \\ B_y \\ B_z + B_{z\text{Offset}} \end{pmatrix} , \tag{3.6}$$

where, $B_{x\text{Offset}}$ and $B_{z\text{Offset}}$ are the defined zero-field points across the $x-$ and $z-$axis respectively. $\dot{\underline{M}}$ is now defined as:

$$\dot{\underline{M}} = \begin{pmatrix} -\Gamma & \beta_{z2D} & \gamma B_y \\ -\beta_{z2D} & -\Gamma & \beta_{x2D} \\ \gamma B_y & -\beta_{x2D} & -\Gamma \end{pmatrix} \underline{M} + \begin{pmatrix} 0 \\ 0 \\ \Gamma_P M_0 \end{pmatrix} , \tag{3.7}$$

where γ is the gyromagnetic ratio. $\beta_{x2D} = \gamma(B_x + B_{x\text{Offset}})$ and $\beta_{z2D} = \gamma(B_z + B_{z\text{Offset}})$.

The solution to Equation (3.7) allows simulated 2D landscapes to be easily created with a user defined zero-field point (defined as $B_{x\text{Offset}}$ and $B_{z\text{Offset}}$) seen in Figure 3.18(a).

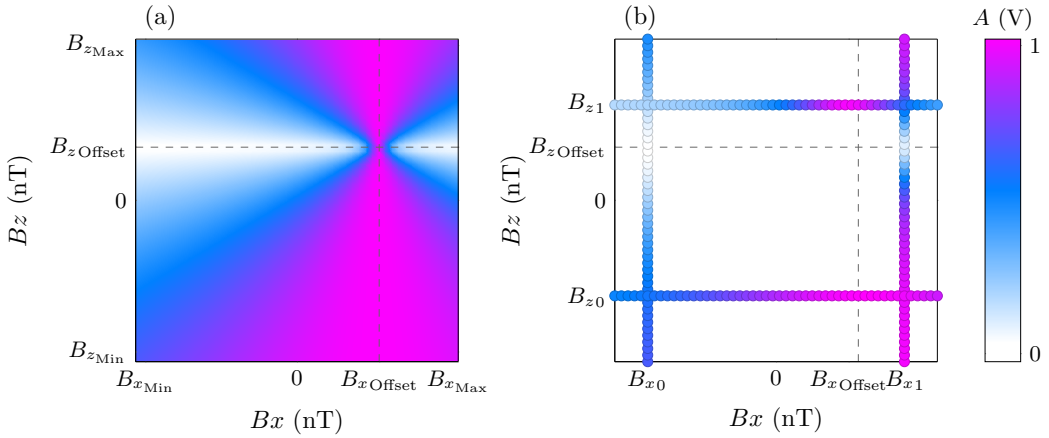

Figure 3.18: Simulated 2D Hanle landscape modelled using the time evolved solution to Equation (3.7), simulated between across the x- and z-axes, in the ranges: $B_{x\text{Min}} \leq B_x \leq B_{x\text{Max}}$ and $B_{z\text{Min}} \leq B_z \leq B_{z\text{Max}}$. The known applied zero-field values, $B_{x\text{Offset}}$ and $B_{z\text{Offset}}$, are indicated. Colour indicates the amplitude, A, of the modelled atomic response. **a)** The full simulated 2D Hanle landscape for 2500 sampled points. **b)** The sampled landscape using the fast zero-field technique, for 200 sample points. Two longitudinal sweeps and two transverse sweeps are measured.

3.3.3 Fast zero-field technique

The 2D Hanle landscape has some useful symmetry, shown in Figure 3.18(a), centered around the zero-field value along each axis. Knowing this, rather than exhaustively measuring the entire landscape as in Figure 3.18(a) (a total of 2500 sampled points), we could instead take individual sweeps along both axes. To reduce the amount of time required to identify the zero-field point in the $x-$ and $z-$axes, I implemented a technique that only requires two sweeps along each axis (a total of 200 sampled points), as illustrated by Figure 3.18(b), equating to a 92 % reduction in the number of measured points across the 2D landscape. As such, the total time to identify zero-field now takes $\simeq 8$ s, resulting in a >10 factor improvement of t_{2D}.

The faster zero-field technique measures two longitudinal resonances, followed by two transverse resonances, to accurately locate the zero-field point for the entire landscape. The technique is described by the flow chart seen in Figure 3.19, which can be summarised as;

1. **Longitudinal resonances:**

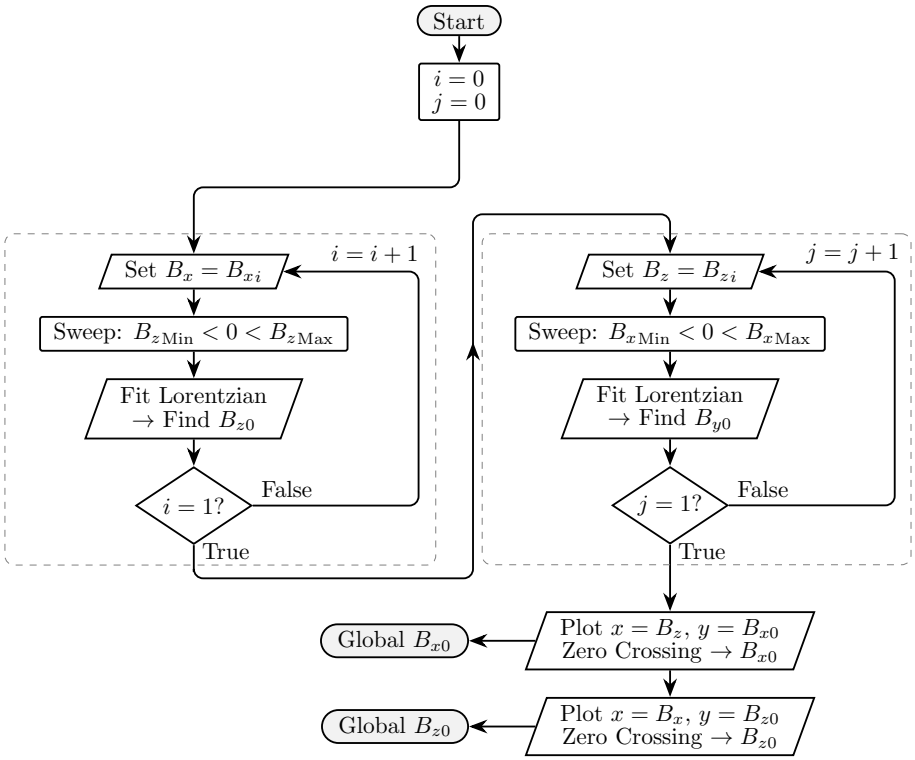

Figure 3.19: Flow chart indicating the steps for the fast zero-field finding technique.

The longitudinal resonance is measured at two values that span broadly across the full range of B_x, B_{x0} and B_{x1}. Using the 1D resonance model (Equation (2.38)), A_0 (the trough of the resonance) is found which correlates to the zero-field point for the resonance. An example of both longitudinal resonances are illustrated in Figure 3.20(a).

2. **Transverse resonances:**

   The transverse resonance is measured at two values that span broadly across the full range of B_z, B_{z0} and B_{z1}. Using the 1D resonance model (Equation (2.38)), A_0 (the peak of the resonance) is found which correlates to the zero-field point for the resonance. An example of both transverse resonances are illustrated in Figure 3.20(a).

3. **Zero-field identification:**

   The global longitudinal zero-field value for the landscape, B_{z0}, is found by

using the A_0 longitudinal resonance values found for the applied transverse field values of B_{x0} and B_{x1}. Plotting the transverse field against the found A_0 values, allows for identification of the zero crossing value, which aligns to B_{z0}, as illustrated in Figure 3.20(b).

Similarly, the global transverse zero-field value for the landscape, B_{x0}, is found by using the A_0 transverse resonance values found for the applied longitudinal field values of B_{z0} and B_{z1}. Plotting the longitudinal field against the found A_0 values, allows for identification of the zero crossing value, which aligns to B_{x0}, as illustrated in Figure 3.20(c).

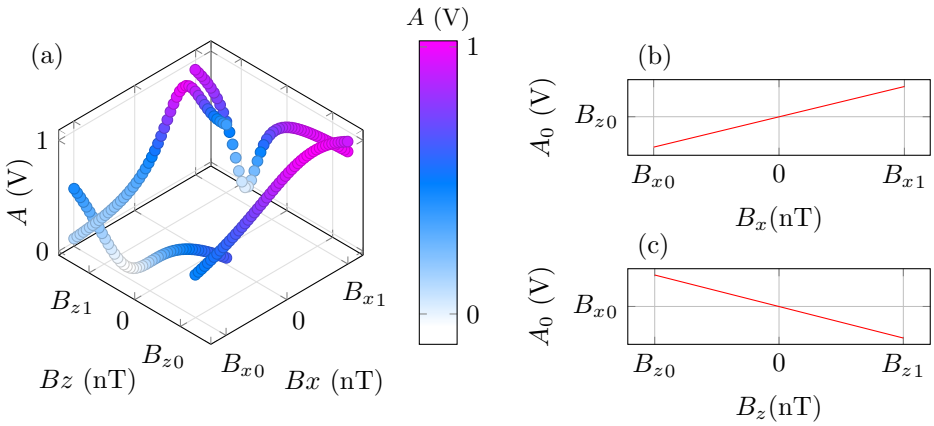

Figure 3.20: Results of the fast zero-field finding technique. **a)** The sampled landscape using the fast zero-field technique, for 200 sample points. Two longitudinal sweeps and two transverse sweeps are measured. **b)** Plot of the transverse field against the found A_0 values which allows for identification of the zero crossing, that aligns to the global longitudinal zero-field value for the landscape, B_{z0}. **c)** Plot of the longitudinal field against the found A_0 values which allows for identification of the zero crossing, that aligns to the global transverse zero-field value for the landscape, B_{x0}.

The model described in Equation (3.7) is used to produce a variety of 2D landscapes with a known randomly selected zero-field value across each axis, to test the accuracy and robustness of the zero-field finding techniques described. Figure 3.21 shows the results of the identification of zero-field for 100 simulated landscapes for both the proposed fast technique in pink, and the slower exhaustive measurement scheme in blue. The deviation of the found zero-field values (B_{x0} and B_{z0}) from the

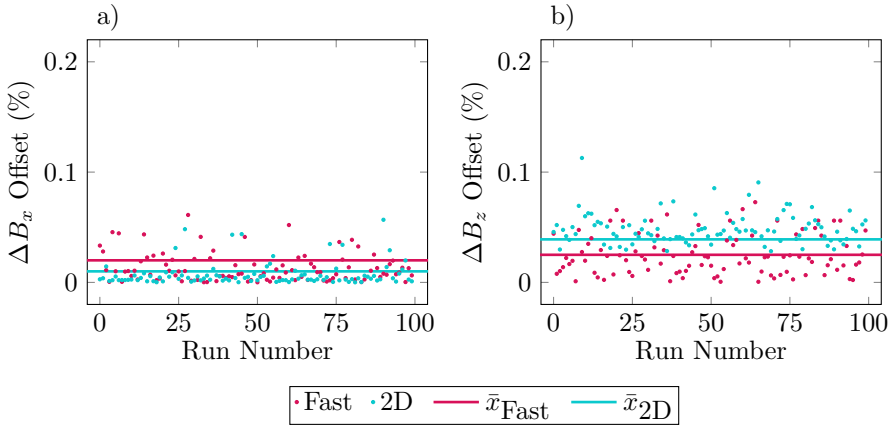

Figure 3.21: Accuracy of identification of the zero-field values for 100 simulated landscapes with known B_x and B_z offsets, simulating the zero-field points along each axis. The percentage difference between the known and measured values, ΔB. **a)** Shows deviation from the zero-field point on the x-axis, ΔB_x. **b)** Shows deviation from the zero-field point on the z-axis, ΔB_z. **a,b)** The colour indicates the routine used; the fast zero-field technique is shown in pink (Fast), and the exhaustive full landscape method is indicated in blue (2D). The found values are indicated with points, and the arithmetic averages for each technique, $\bar{x}_{Fast}$ and $\bar{x}_{2D}$, are indicated by solid lines.

known applied zero-field values ($B_{x\text{Offset}}$ and $B_{z\text{Offset}}$) is measured as $\Delta B_{x\text{Offset}}$ (%) in Figure 3.21(a), and $\Delta B_{z\text{Offset}}$ (%) in Figure 3.21(b). The average deviation value is indicated for both techniques by the appropriately coloured solid line as indicated, which is $< 0.1\%$ for all techniques. Both graphs show that the fast technique is similarly accurate in both the $x-$ and $z-$axis for identifying the known zero-field values. Thus, we can conclude that the fast zero-field technique is considerably faster (>10 factor improvement of t_{2D}) without a significant loss in accuracy when identifying the zero-field value in two orthogonal axis.

Chapter 4

Machine learning optimisation

The work presented in this chapter is based on and expands upon the results published in [91], seen in full in Appendix B. The performance of a SERF magnetometer is driven by: 1) the experimental design of the magnetometer and 2) the selected value of the magnetometer's operational parameters. The hardware development of the laboratory and portable systems are discussed elsewhere in the thesis, although, as will be discussed, computational optimisation methods can be brought to bear on design. Here, the control of the magnetometer describes the selection of all operational parameters such as cell temperature and laser power. In this chapter the selection of operational parameter values with the direct aim of optimising the SERF magnetometer's performance will be explored. I will show that the selection of operational parameters has a large effect on performance. For example, if the vapour cell in the SERF magnetometer is only heated to 50 °C, we would expect a very broad Hanle resonance due to a high rate of spin exchange relaxation and low atomic density, leading to an overall poor magnetometer performance. In contrast, if the same vapour cell in the SERF magnetometer is heated to 120 °C, we would expect a narrow Hanle resonance due to suppression of spin exchange relaxation and high atomic density, leading to an overall improvement in magnetometer performance. In this chapter I will discuss a single, common metric to compare the effect on performance of changes of a range of parameters.

This chapter will discuss a number of optimisation methods that were developed

and used on the SERF magnetometer to optimise sensitivity through experimentally found optimal values for operational parameters. All the optimisation methods explored are types of automated machine learning (ML) strategies. Machine learning is an effective tool to interrogate complex systems to find optimal parameters more efficiently than through manual methods. This efficiency is particularly important for systems with complex dynamics between multiple parameters and a subsequent high number of parameter configurations, where an exhaustive optimisation search would be impractically time consuming. The magnetometer's sensitivity will be optimised through both direct measurement of the noise floor, and indirectly through measurement of the on-resonance demodulated gradient (mV/nT) of the zero-field resonance. The validity of ML techniques for optimisation will be proven through measured sensitivity improvements of the SERF magnetometer. The flexibility and efficiency of the ML approaches also facilitates optimisation of parameters beyond experimentally controlled parameters, such as hardware changes. Lastly, this chapter demonstrated the use of ML to quickly optimise the hardware of the OPM, by iteratively testing a number of atomic vapour cells with varying nitrogen buffer gas pressure, to improve magnetometer performance as measured by sensitivity.

4.1 Machine learning for caesium SERF magnetometry

The optimal signal from the SERF sensor has intrinsic complex dynamics in at least five-dimensions contained within the parameters of: 1) atomic density (through cell temperature), 2) laser frequency, 3) laser power, 4) detection modulation frequency and 5) detection modulation depth. To date, few SERF sensors reported in the literature use caesium [29, 92] and only a single sensor is known by the author that operates in the single-beam configuration that is used in portable sensors [51]. As such, the optimal operation parameters of the sensor are not known a priori. Some experimental parameter configurations have been well-described in the literature [93, 94] and others may be modelled accurately [54]. In general, sensitivity is improved by elevating the temperature of the cell to the increase atomic density and subsequently increase spin exchange collisions. A threshold exists at which the opacity of the

cell reduces the transmission of the light through the cell and hence the signal amplitude. Increasing laser power raises the optical pumping efficiency, at the cost of higher intensity noise and broadening of the magnetic resonance (and subsequent reduction of sensitivity). Here, an automated approach is utilised for optimising the primary experimental parameters with a view to maximising the sensitivity of the SERF magnetometer.

Here three automated optimisation techniques are presented that have been used independently to assess the best operation parameters based on experimental performance quantified through a chosen cost function, C. The techniques include a genetic algorithm, a simplified form of gradient ascent optimisation, and an open-source machine-learning package that utilises predictive modelling. These automated optimisation techniques are presented in the context of the caesium SERF magnetometer to demonstrate use as a generic routine for finding the optimal operating point for a complex sensor.

Beyond the realms of computer science, automated optimisation and machine learning have been utilised across many disciplines [74, 95–99], and have found success in quantum and particle physics [100–102]. Machine learning has been adopted for the optimisation of experimental parameters for complex systems [103–105], where traditional human-intuition-based experimental control is laborious, inefficient, and may not result in the optimal configuration [106].

The optimisation approach applied here has yielded previously unknown configurations of parameters leading to operation of the magnetometer blue-detuned from the optical absorption peak rather than at peak absorption [65]. It has allowed us to create a robust, flexible and fast test environment for benchmarking cells of various buffer gas pressures and different alkali species, which aids sensor development.

4.2 Machine learning optimisation methods

For all the research presented in this chapter, the SERF magnetometer set-up as described in Chapter 3 is utilised and constructed in a portable sensing package. The full description of the portable sensor design is found in Chapter 5, and the full

operational procedure is explained in extensive detail in Section 3.3.

4.2.1 Machine learning

Machine learning works to identify a global optimum (maximum or minimum) within a parameter space. Here, multiple machine learning algorithms (MLAs) that implement supervised learning will be demonstrated and compared. Supervised learning refers to providing the MLA with a quantitative measure of performance known as cost [103]. For all techniques, the MLA and experiment are contained within a closed loop where the MLA controls the experiment, which in turn gathers and returns cost information to the MLA. More specifically, the MLA selects the experimental parameters, which are translated to the experiment through control instrumentation. The experiment automatically completes the zero-field resonance measurements in both 2D and 1D, and calculates cost according to a particular cost function, $C(\rho)$. The cost associated with each parameter set is used by the MLA to inform the next set of parameters to sample.

The choice of cost functions is one of the arts of implementing ML and it is not always evident a priori what the optimal cost function might be. In this work two cost functions, $C_1(\rho)$ and $C_2(\rho)$, are defined to optimise in two distinct ways in order to assess which cost function is most effective. The first cost function, $C_1(\rho)$, measured in (mV/nT), is equal to the gradient of the demodulated lineshape, where $C_1(\rho) = \chi$ as defined by Equation (2.47), such that:

$$C_1(\rho) = \frac{\delta A_{\text{Demod}}}{\delta B_y} \ , \tag{4.1}$$

where δA_{Demod} and δB_y are, respectively, the change in amplitude and magnetic field of the demodulated lineshape within the linear range. C_1 has been selected as this corresponds to a "sharp" 1D resonance line-shape, that is, a high amplitude with narrow width, which is a good indicator of OPM performance. Thus, C_1 must be maximised to increase line-shape sharpness and as such a global maximum of C_1 is desired.

The second cost function, $C_2(\rho)$, is a sensitivity approximation measured directly through analysis of the noise floor. A power spectral density is taken to extract a series of frequency dependent amplitude values, $X(k)$, that are scaled by the demodulated gradient (C_1) to provide a frequency response as a function of magnetic field. $C_2(\rho)$ is found through combination of the measured sensitivity, δB_1, from the geometric mean of the noise spectrum as expressed by Equation (2.49) within our band of interest (5 to 20 Hz).

$$C_2(\rho) = \left(\prod_{5 \leq k \leq 20}^{n} \frac{\delta A_{\mathrm{Demod}}}{\delta B_y} X(k) \right)^{\frac{1}{n}} . \tag{4.2}$$

Stochastic noise manifests logarithmically thorough only positive peaks, therefore the use of the geometric mean is more appropriate than the arithmetic mean, as discussed in Section 2.6.6. By minimising C_2, which is a measure of the intrinsic noise of the magnetometer in the frequency band of interest, the magnetic sensitivity is optimised. Thus, the location of a global minimum of C_2 across the parameter space is desired. Both defined cost functions aim to improve sensitivity, where C_2 will achieve this directly and C_1 indirectly.

4.2.2 Optimisation techniques

For the total number of experimental parameters, M, a single set of experimental settings (temperature, laser power, etc.) is defined as $X = (x_1, \ldots x_M)$. For each individual set, X_i, an associated cost, $C(X_i)$, and associated cost uncertainty, $U(X_i)$, are found experimentally. All optimisation techniques selected are examples of online optimisation (OO) in which optimisation is implemented concurrently with experimental testing. Two evolutionary OO algorithms are employed, a gradient ascent OO and a predictive model-based machine learning algorithm. All optimisation methods continue until 250 sets of parameters are tested, known as the end condition, $N_{\mathrm{end}} = 250$, which takes approximately 4 h in total. This end condition is selected to allow all MLA methods the same number of interactions and to ensure

optimisation is completed in a time-frame that is reasonable for equivalent manual optimisation activities for a skilled operator.

4.2.3 Evolutionary algorithms

Evolutionary algorithms are heuristic search-based approaches to solving problems. The processes of evolutionary algorithms are inspired by nature and biological systems [107]. The scheme, shown in Figure 4.1, includes the evaluation of the performance of individuals within a population to inform the selection of a new population mimicking "survival of the fittest", a crossover of high-performing individuals to imitate reproduction and mutation. Mutation introduces a stochastic component and aims to drive optimisation to a global maximum or minimum. Evolutionary algorithms are commonly used across many types of optimisation problems [108], due to their robust convergence to a solution. However, this convergence time increases with the system complexity. We use two evolutionary algorithms within the ML techniques in this chapter, which are both standard methods in the ML community [109–111]. The first evolutionary algorithm used is a genetic algorithm (GA) [112, 113] that is implemented standalone, and the second is a differential evolution (DE) [114, 115] algorithm, which is incorporated into the process of the predictive model-based machine learning algorithm [103], discussed more in Section 4.2.5.

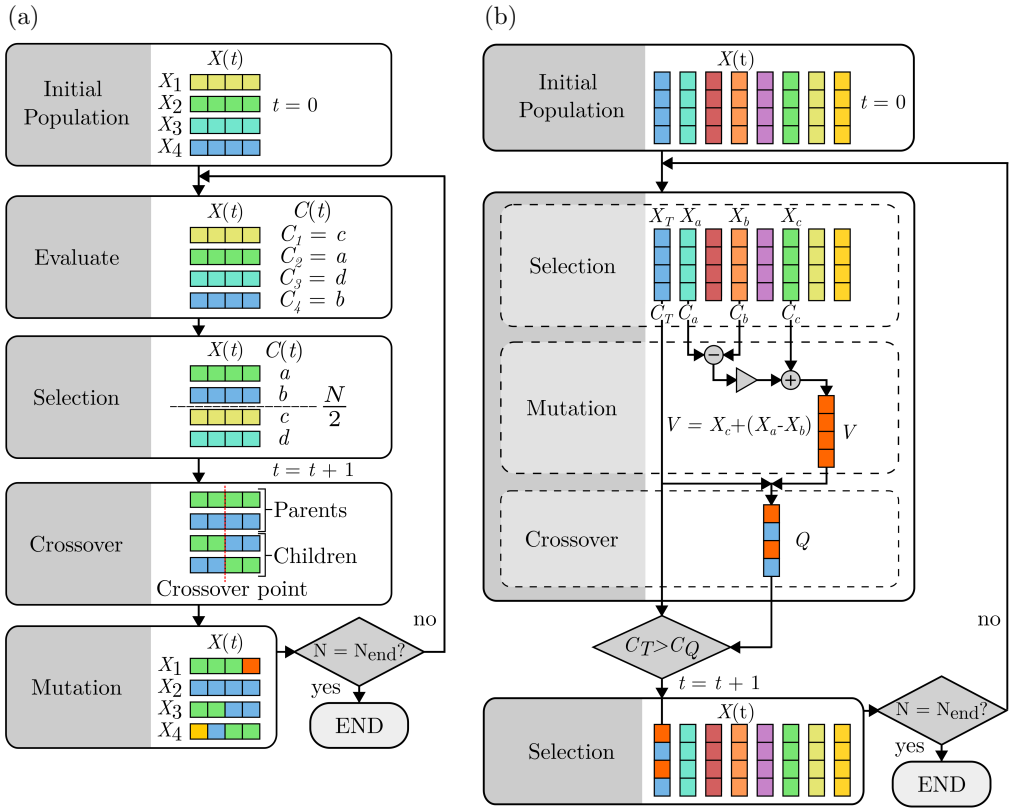

Figure 4.1: Two evolutionary algorithm processes, **a**) Genetric algorithm and **b**) differential evolution, where (**a**) & (**b**) share evolutionary elements of initial population formation, selection, crossover and mutation. For both algorithms, the initial population $X(t)$ contains a population of N sets of parameter settings. The colour indicates each set of parameter settings. t, generation or loop number; $t = t + 1$, the next generation; and $C(t)$, measured cost. Both algorithms repeat until the end condition is met, where the number of sets of parameters tested N is equal to 250 (N_{end}). (**a**) GA process. The initial population is generated and evaluated for cost, with individual costs denoted as C_i. $\frac{N}{2}$ parameter sets are selected for the next generation based on ranked cost. The best performing $\frac{N}{2}$ are used as "parents" to produce "children" sets during crossover with respect to the crossover point. Mutation of individual parameter values randomly occurs in the new population. (**b**) DE process. The initial population is generated and evaluated for cost where three random sets X_a, X_b & X_c and a target set X_T are selected. A new set V is created during mutation from the randomly selected sets, and used in a crossover with the target set to make a new set Q. C_Q, the cost of Q, is evaluated and measured against C_T, the cost of the target set. The target set is replaced in a new generation if $C_Q > C_T$ (for C_1) or $C_Q < C_T$ (for C_2).

The GA process is displayed in Figure 4.1(a). The GA first randomly creates the initial population, $X(t)$, of N sets of experimental parameters

$$X(t) = \{X_1, \dots X_N\} \ , \tag{4.3}$$

where t denotes the generation of the population, initially $t = 0$.

All parameters chosen are selected within predefined parameter space limits. Next, each parameter set, X_i, is automatically and iteratively evaluated through experimental testing and find associated cost $C(t)$ and uncertainty $U(t)$ of the entire population, where, $C(t) = (C_1, \dots C_N)$ and $U(t) = (U_1, \dots U_N)$. Parameter sets with high levels of uncertainty will be ranked poorly even in cases of favourable costs, to ensure robust optimisation. The selection of the new generation population, $X(t)$, is based on the best performing sets of experimental parameters from the previous generation $X(t-1)$. To achieve this, $X(t-1)$ is ranked by $C(t-1)$ with respect to $U(t-1)$ and the best performing $\frac{N}{2}$ sets of parameters are added to $X(t)$. The remaining $\frac{N}{2}$ sets of parameters are created through a crossover. Crossover occurs between sets of parameters from the previous generation to create sets for the new generation, shown in Figure 4.1(a) and given by:

$$X(t)_j = \{x | x \in X_a(t-1) \text{ if } x_i \leq CP, x \in X_b(t-1) \text{ if } x_i > CP\} \tag{4.4}$$

$$X(t)_k = \{x | x \in X_b(t-1) \text{ if } x_i \leq CP, x \in X_a(t-1) \text{ if } x_i > CP\} \ , \tag{4.5}$$

where $X(t)_j$ and $X(t)_k$ are "children" sets of "parent" $X_a(t-1)$ and $X_b(t-1)$. The crossover point, CP, refers to an individual element, x_i, of the parent sets. The final step is to introduce random mutation to prevent optimisation for a local optimum. The new population, $X(t)$, is then evaluated experimentally and the algorithm continues until the end condition is met.

The process of DE deviates from GA as shown in Figure 4.1(b), while maintaining the same evolutionary elements. The initial population of sets of parameters is created as defined in Equation (4.3) and similarly evaluated to find the associated

cost $C(t)$ and uncertainty $U(t)$ of the entire population. The mutation process is incorporated through creation of a new set, V, derived from three randomly selected parameter sets (X_a, X_b and X_c), where each individual parameter is a combination of the value from all three sets such that $V = X_c + |X_a - X_b|$. Crossover occurs between V and a randomly selected target set X_T to produce an additional set Q. Q is evaluated experimentally and replaces X_T in the new generation where $t = t + 1$, if C_Q outperforms C_T. Lastly, three random sets and a target set are selected from the new population, $X(t)$. The algorithm continues until the end condition is met. DE algorithms can be more efficient during optimisation due to a generalised higher occurrence of evolution mechanisms than GAs [116].

4.2.4 Gradient ascent

Gradient ascent algorithms are a first-order process. As such, the differential of the changing cost $C(\rho)$ is used to inform the learning process [117]. Here, a form of batch gradient algorithm is implemented, displayed in Figure 4.2. Small batches of data are tested to find the optimal parameters based on the gradient of the cost across the batch. Learning occurs between iterations of batches. Batch gradient algorithms guarantee convergence to a local or global optimum. However, as the batch sizes are pre-defined, some points tested may be redundant, especially compared to stochastic gradient processes with a higher learning rate [118–120].

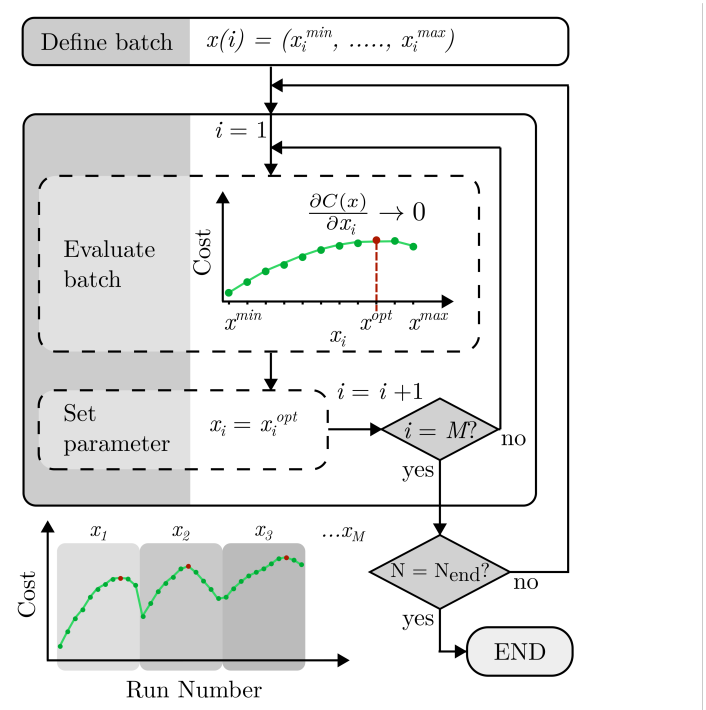

Figure 4.2: Gradient ascent algorithm process. $x(i)$, a vector value for a single parameter x_i ranging from minimum x_i^{min} to maximum x_i^{max} as defined by parameter space range. i, the individual parameter selected. Initially, the first parameter is selected for the first batch $i = 1$. All other parameters are kept constant. The batch is evaluated based on cost, indicated in green, to find where the gradient tends to zero, $\frac{\partial C(\rho)}{\partial x} \rightarrow 0$ indicated in red. The corresponding parameter value x_i^{opt} is then set for this parameter for the next batch, $i = i + 1$. This continues until all parameters are used as batches, for a total number of parameters M. The segmented graph shows this process as a function of the run number. This process in turn repeats until the end condition is met, where the number of sets of parameters tested N is equal to 250 (N_{end}).

In this context, each batch $x(i)$ is defined as a broad sweep of a single parameter across the full range for that parameter in regular intervals as follows:

$$x(i) = (x_i^{min}, x_i^{min} + n, \ldots x_i^{max}) \ , \tag{4.6}$$

where i denotes the individual parameter, n is the interval for the parameter, and x_i^{max} and x_i^{min} are the maximum and minimum values of the specific parameter from the defined parameter range. The first batch targets the first parameter only, where

$i = 1$. The non-target parameter values are kept constant throughout the batch testing at the previously found optimum, or initially selected randomly. Evaluation of the batch experimentally finds the associated cost for each element of $x(i)$. The cost curve of the batch is used to find where the gradient tends to zero, $\frac{\partial C(\rho)}{\partial x} \to 0$. The value of x_i is set to the corresponding parameter value, x_i^{opt}, for the next batch iteration. Each iteration changes the target parameter used for the batch, where $i = i+1$ after each batch, up to the total number of M parameters. One full process of the gradient algorithm occurs after all parameters have been selected as the target parameter, which in turn loops until the end condition is met.

4.2.5 Gaussian process regression

The Gaussian process (GP) regression OO method creates a model defining how each experimental parameter relates to the experimentally found cost, known as the cost-landscape. The cost-landscape is formed through training the MLA with data collected by DE for $2M$ sets of parameters. The model generates correlation lengths to indicate how sensitive the cost is to each parameter, where the correlation length is inversely proportional to its influence on cost. The cost-landscape model informs the selection of new parameter values to test. Each iteration informs the model and contributes to defining the noise level of "expected cost" to "found cost", i.e., the variance of the cost if measured at the same set of parameters many times. For this method, an open-source Python-based machine learning toolkit, M-LOOP [103] (Machine Learning Online Optimization Package), is implemented which utilises DE and GP during optimisation. While GP regression is the most sophisticated MLA employed, Gaussian processes lose efficiency in high dimensional spaces and the computational time required scales with the cube of the number of tests.

4.2.6 Experimentally controlled parameters

The parameters, p, selected for optimisation are: (1) Cell Temperature, T, (2) Laser Power, LP and (3) Laser Detuning, LD. These parameters are intrinsically linked with complex dynamics as described in Section 4.3.1. Each parameter is directly

Table 4.1: Definition of all controlled parameters (p) used for optimisation, with corresponding units. Min(p), the minimum value for each parameter. Max(p), the maximum value for each parameter. Default (p), chosen default value if parameter is not directly optimised during optimisation.

Parameter	**Min*(p)***	**Max*(p)***	**Default*(p)***	**Unit**
Temperature	115	140	-	°C
Laser Power	0.5	6	-	mW
Laser Detuning	−20	20	-	GHz
A_{Mod}	0.2	1.5	0.5	dimensionless
F_{Mod}	0.2	1.5	1	dimensionless

controlled through experimental hardware. Both amplitude and frequency of the applied modulated magnetic field influence light absorption and magnetometer performance. As such, a further two parameters are defined, namely (4) Modulation Amplitude, B_{Mod}, and (5) Modulation Frequency, ω_{Mod}. For optimisation we use the dimensionless parameters $\mathrm{A_{Mod}}$ and $\mathrm{F_{Mod}}$, defined with respect to the magnetic resonance linewidth;

$$A_{\mathrm{Mod}} = \frac{B_{\mathrm{Mod}}}{\Gamma} \tag{4.7}$$

$$F_{\mathrm{Mod}} = \frac{\omega_{\mathrm{Mod}}}{\Gamma\gamma}, \tag{4.8}$$

where total relaxation Γ is equal to the HWHM width extracted from magnetic resonance and γ is the gyromagnetic ratio ($2\pi \times 3.5$ Hz/nT for Cs). B_{Mod} and ω_{Mod} are dependent factors, and the modulation index, m_i, defines this dependency:

$$m_i = \frac{\gamma B_{\mathrm{Mod}}}{q(P)\omega_{\mathrm{Mod}}} \ , \tag{4.9}$$

where $q(P)$ is the nuclear slowing-down factor at high polarisation [38]. It has been shown that the optimal modulation index occurs when $m_i = 0.5 - 1$ [56]. All control parameter ranges are defined in Table 4.1.

The selection of the parameter ranges shown in Table 4.1 was based on systematic testing of the OPM response around the boundaries of these ranges to identify when a resonance is no longer measurable. For example, if the cell temperature is > 140°C, the opacity of the cell is increased by the increasing atomic density, to the point

that no light reaches the detector, to an extent that cannot be accommodated for by increasing the laser power or shifting the laser frequency away from resonance.

4.3 ML optimisation of experimental parameters

The MLAs presented in Section 4.2.2 were applied to optimise the sensitivity of the single-beam caesium SERF OPM. Two cost functions (C_1, C_2) were utilised to investigate cost function suitability. The number of parameters optimised ($M = 3$: LD, LP, T, $M = 5$: LD, LP, T, A_{Mod}, F_{Mod}) is varied to demonstrate MLA robustness with respect to optimisation complexity. In total, four independent optimisation schemes were measured:

Scheme 1. Cost = C_1, $M = 3$

Scheme 2. Cost = C_1, $M = 5$

Scheme 3. Cost = C_2, $M = 3$

Scheme 4. Cost = C_2, $M = 5$

Three MLAs were used per optimisation scheme: (1) genetic algorithm, (2) gradient descent algorithm and (3) Gaussian process regression. The full parameter space used for all optimisation schemes is defined in Table 4.1. For equality between optimisation schemes, all methods initialise with a random set of parameter values, often initially producing no magnetic resonance signal. Each MLA ran until the end condition, requiring 250 sets of experimental settings to be tested, $N_{\text{end}} = 250$, taking approximately 4 h in total per MLA. Both cost functions were measured during each technique, regardless of the selected cost function, to allow comparison.

To benchmark the optimised sensitivity of all MLAs and optimisation schemes, the SERF magnetometer was first manually optimised through human-intuition-based experimental control. The human optimisation process found an optimal sensitivity of 500 fT/$\sqrt{\text{Hz}}$, in approximately 4 h, through directly optimising sensitivity, C_2. The human optimisation process was carried out by a skilled operator, familiar with OPMs and given control of all operational parameters, where general intuition lead to the selection of the first parameter values selected, and all subse-

quent parameter values tested. The skilled operator was selected from within the department, and had no prior knowledge of the optimum parameter values before operation, to remove any potential bias in parameter selection.

The results of all optimisation schemes for all MLAs are shown in Figure 4.3. Each row in Figure 4.3 displays the results for an individual optimisation scheme, with Cost Function $C(\rho)$ and the number of parameters (M) indicated accordingly. Progression of each technique can be seen in Figure 4.3(a,d,g,j), where cost is a function of the experimental run number and the moving maximum (for C_1) or minimum (for C_2) throughout optimisation run is indicated by the solid line for each MLA. Figure 4.3(b,e,h,k) show the corresponding $\sqrt{\text{PSD}}$ for the optimal parameters found per MLA, with the sensitivity shown as a function of frequency (Hz) in the bandwidth of interest (5 to 20 Hz). Figure 4.3(c,f,i,l) depict the corresponding demodulated line shape for the optimal parameters found per MLA.

The optimised cost for each MLA and optimisation scheme with corresponding optimal parameter settings can be seen in Table 4.2. All optimisation schemes resulted in large cost improvement throughout optimisation. Each ML technique generates a converging solution, the values of these vary but are close within each scheme.

The optimum sensitivity of 109.5 fT/$\sqrt{\text{Hz}}$ was identified by the gradient descent algorithm (with an uncertainty of ± 1 fT/$\sqrt{\text{Hz}}$ taken from the geometric standard deviation across the frequency band of interest) using five parameters ($M = 5$) and direct optimisation of sensitivity (C_2). The optimum demodulated gradient of 4.75 mV/nT was identified (with an uncertainty of ± 0.03 mV/nT, taken as the linear fitting error across demodulated linear region) by the Gaussian process regression model using five parameters and direct optimisation of demodulated gradient (C_1).

The GP model is the most sophisticated MLA demonstrated. Due to the nature of the optimisation method, as described in Section 4.2.5, a cost-landscape depicting how each parameter affects the measured cost is produced throughout the optimisation process. Figure 4.4 shows the measured data for each parameter as a function of cost, for optimisation schemes 2 and 4 (5 parameter optimisations). The parameter

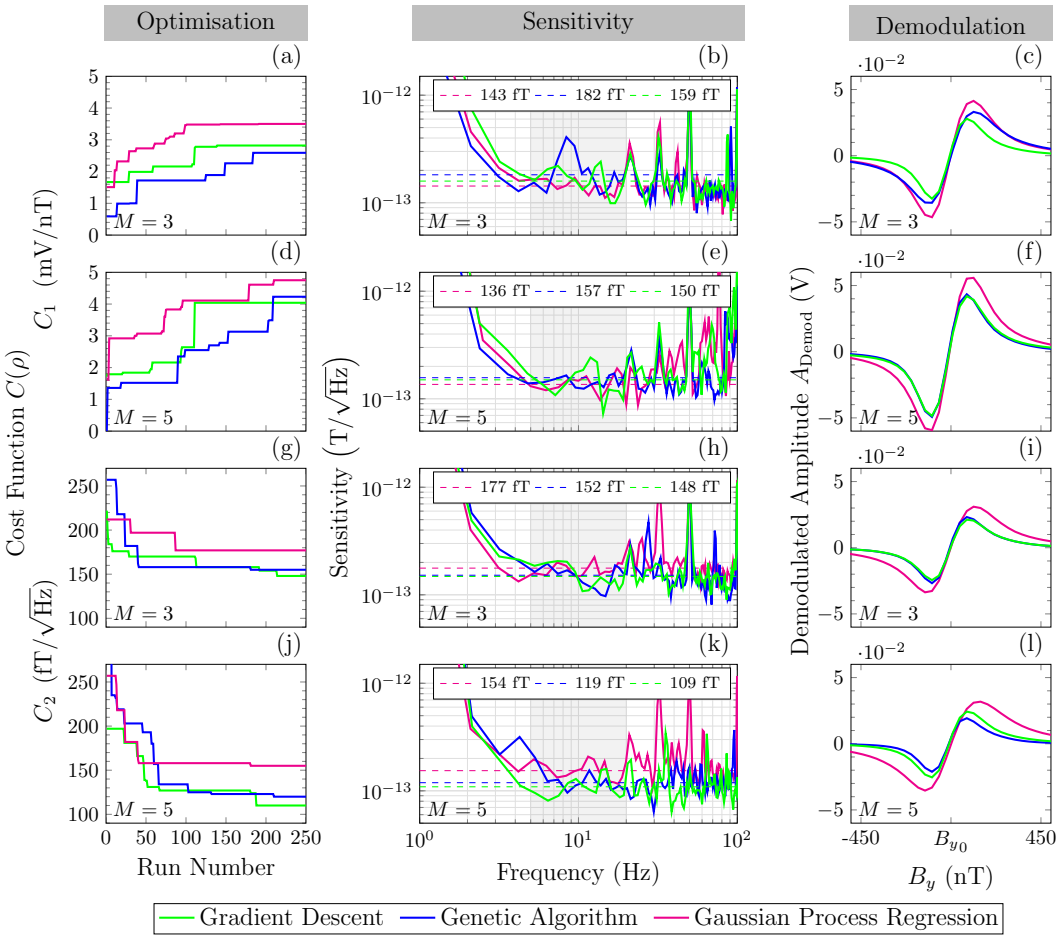

Figure 4.3: All figure parts contain the following optimisation techniques, gradient descent algorithm in green, genetic algorithm in blue and Gaussian process regression model in pink. M, the number of parameters optimised. Row 1 & 3, (**a**–**c**,**g**–**i**), optimisation of 3 parameters ($M = 3$). Row 2 & 4, (**d**–**f**,**j**–**l**) optimisation of 5 parameters ($M = 5$). Row 1 & 2, (**a**–**f**), optimise for maximising cost function C_1 the demodulated line shape gradient (mV/nT). Row 3 & 4, (**g**–**l**), optimise for minimising cost function C_2, calculated sensitivity (T/$\sqrt{\text{Hz}}$). Column 1 "Optimisation", (**a**,**d**,**g**,**j**), show Cost function as a function of run number. The solid line indicates the moving maximum per optimisation technique. Column 2 "Sensitivity", (**b**,**e**,**h**,**k**), shows corresponding $\sqrt{\text{PSD}}$ for the optimal parameters found per optimisation technique. Sensitivity is shown as a function frequency (Hz), raw data are shown by solid lines. The frequency band of interest (5 to 20 Hz) is highlighted in grey. Averaged sensitivity in this band is shown by the dashed line (value represented in the key). Column 3, "Demodulation", (**c**,**f**,**i**,**l**), shows a corresponding demodulated line shape for the optimal parameters found per optimisation technique.

Table 4.2: Optimal parameters found for the following optimisation techniques, GA), gradient descent (GD) and GP. The outcome for a skilled operator, SO, is also shown. The number of parameters tested, M, is specified for each optimisation run. T, cell temperature ($^{\circ}C$). LP, laser power (mW). LD, laser detuning (GHz). A_{Mod}, modulation amplitude factor (dimensionless). F_{Mod}, modulation frequency factor (dimensionless). m_i, modulation index (dimensionless). $C(\rho)$ defines the cost function implemented. C_1 is the demodulated lineshape gradient (mV/nT), with uncertainty taken as the geometric standard deviation across the frequency band of interest. C_2 is the calculated sensitivity (fT/$\sqrt{\mathrm{Hz}}$), with uncertainty taken as the linear fitting error across demodulated linear region. Γ is the FWHM of the magnetic resonance (nT), with uncertainty taken as the fit error to Equation (2.38). Values in grey indicate parameters that were not optimised during operation. The scheme that found the optimal sensitivity, C_2, is highlighted in **bold**.

ML	**M**	$C(\rho)$	C_1	C_2	Γ	T	LD	LP	A_{Mod}	F_{Mod}	m_i
GD	3	C_1	2.8 ± 0.03	158.6 ± 1.3	132.5 ± 1.5	119.4	8.24	6.00	0.50	1.00	0.55
GA	3	C_1	2.6 ± 0.02	182.4 ± 1.4	183.3 ± 2.1	115.0	3.00	5.35	0.50	1.00	0.55
GP	3	C_1	3.5 ± 0.03	143.4 ± 1.2	168.8 ± 1.6	115.0	8.00	6.00	0.50	1.00	0.55
GD	5	C_1	4.0 ± 0.02	150.2 ± 1.5	130.1 ± 2.1	118.9	10.8	5.58	1.50	0.30	5.51
GA	5	C_1	4.2 ± 0.02	157.6 ± 1.3	98.8 ± 2.0	123.0	7.00	5.32	1.48	0.39	4.21
GP	5	C_1	4.8 ± 0.03	136.3 ± 1.2	147.4 ± 1.2	120.1	6.22	6.00	1.50	0.21	7.82
GD	3	C_2	2.1 ± 0.02	148.3 ± 1.3	143.4 ± 2.5	117.9	5.88	5.35	0.50	1.00	0.55
GA	3	C_2	2.4 ± 0.02	152.3 ± 1.3	136.7 ± 1.3	119.0	4.00	4.66	0.50	1.00	0.55
GP	3	C_2	2.3 ± 0.02	177.4 ± 1.3	192.8 ± 1.6	115.0	3.49	5.57	0.50	1.00	0.55
GD	**5**	C_2	**2.2 ± 0.03**	**109.5 ± 1.3**	**137.7 ± 1.6**	**118.9**	**7.69**	**5.58**	**0.70**	**0.80**	**0.96**
GA	5	C_2	2.0 ± 0.02	119.8 ± 1.2	111.1 ± 2.1	121.0	7.00	5.24	0.97	1.15	0.93
GP	5	C_2	3.7 ± 0.02	154.8 ± 1.2	203.1 ± 1.6	115.0	3.00	5.50	1.09	1.00	1.20
SO	5	C_2	2.0 ± 0.03	499.9 ± 7.8	171.0 ± 1.3	135.0	- 6.00	5.00	1.00	1.06	1.04

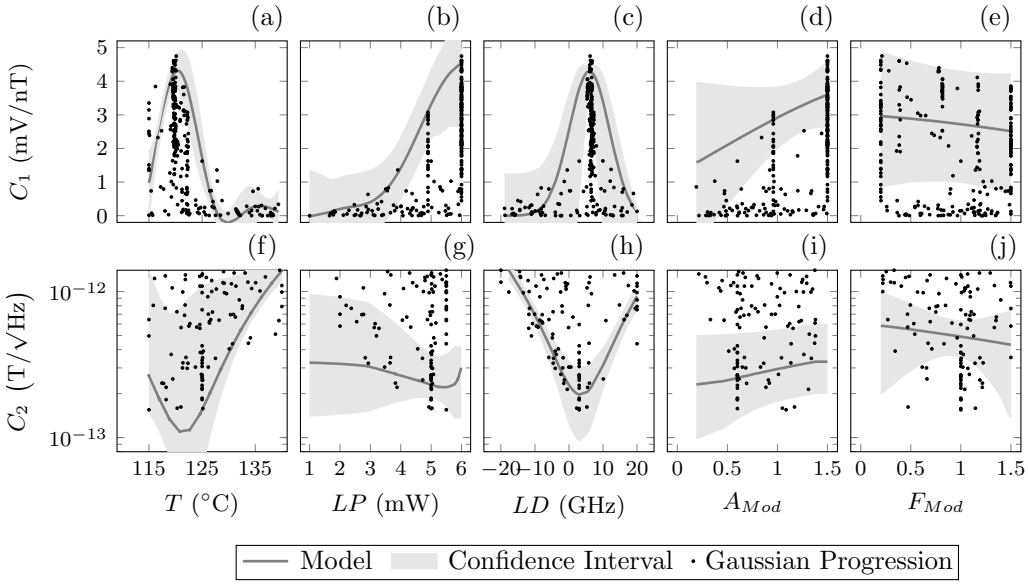

Figure 4.4: Data and models resulting from the Gaussian process regression model MLA, 5 parameter optimisation schemes ($M = 5$). The results on each row are taken from different optimisation schemes. the The 5 parameters optimised are cell temperature (T), laser power (LP), laser detuning (LD), modulation amplitude factor (A_{Mod}) and modulation frequency factor (F_{Mod}). Each part shows a parameter as a function of the cost. Row 1, (**a**–**e**), shows optimisation for cost function C_1, the demodulated line shape gradient (mV/nT). Row 2 , (**f**–**j**) optimisation for cost function C_2, calculated sensitivity ($\mathrm{T}/\sqrt{\mathrm{Hz}}$). Marks indicate measured values from optimisation, solid line indicates the Gaussian process predicted cost-landscape and shaded region indicates the model provided 95% confidence interval of the cost-landscape.

cost-landscape model is indicated with a line, and the 95% confidence interval generated by the model is indicated by the shaded region. Many measured points for all parameters lie outside the confidence interval due to the nature of multi-parameter optimisation, where the optimised value of one parameter may produce a poor cost value if other parameters are not optimised. The confidence interval shows the trust region of the models predictive landscape after all measurement has been completed.

4.3.1 ML optimisation of experimental parameters: Discussion

The sensitivity of the caesium OPM has been improved by all of the MLAs presented in comparison to human optimisation over comparable run-time. This comprehensive improvement indicates the suitability of automated optimisation methods for experimental parameter optimisation tasks in optically pumped magnetometry.

The use of 3 MLAs allowed for comparison of these techniques to aid recommendations for suitability. In this use case, all techniques appear capable, with no single technique standing out as significantly more favourable. Completing the MLA techniques for a differing number of parameters allows comparison of the robustness of the MLA techniques to the system complexity. Interestingly, the more simple MLAs (GA and GD) proved most successful for direct sensitivity optimisation C_2, with GD providing the optimal sensitivity value of 109.5 $\mathrm{fT}/\sqrt{\mathrm{Hz}}$. However, the Gaussian process regression model proved most effective for optimisation of C_1. This suggests that the Gaussian process regression model was more sensitive to the more stochastic nature of cost function C_2.

Increasing the complexity to $M = 5$ parameters, proved beneficial to both cost functions. As such, the amplitude and frequency of the applied magnetic modulation are tied to magnetometer performance due to their influence on light absorption. Optical noise has a large contribution in this sensor, and this noise decreases with increased absorption. Furthermore, low frequency 1/f noise decreases with increasing modulation frequency. Each five parameter optimisation scheme converged before the end condition, suggesting that, in multi-parameter systems with five parameters, all MLAs are suitable.

The implementation of two cost functions, C_1 and C_2, aids identification of the most suitable cost function for this purpose. Table 4.2 shows relative alignment of the best parameter values between cost functions. The peak sensitivity found indirectly (C_1) is 30 fT/$\sqrt{\text{Hz}}$ higher than through direct sensitivity optimisation (C_2). As such, C_1 acts as a reasonable proxy for sensitivity optimisation without specifically measuring sensitivity. C_1 requires less data collection and corresponding sensitivity measurements may be taken after the fact. C_2 takes longer experimentally and computationally and is more susceptible to extraneous environmental and technical noise. However, 5 parameter optimisation using C_1 optimised the modulation frequency to a much lower frequency. The subsequent modulation index for these optimised values are also far outside the expected range ($m_i > 5$). This highlights a key drawback of optimisation using C_1, that technical noise contributions are not considered.

A benefit of the implementation of the GP is the production of the cost-landscape model that defines how influential each parameter is on performance. From this model, Figure 4.4, clear trends can be seen that span across both cost functions; for example, the peak in temperature for C_1 aligns with the trough in C_2. Alignment of the trends indicates the parameter has a similar influence on both cost functions.

Figure 4.4 also shows mirrored trends for laser detuning, optimising at a similar value. However, a deviation between the laser power landscape between cost functions is also present. The peak laser power required for C_1 continues to increase beyond the defined range, whereas the optimum laser power for C_2 saturates at 5 mW. This could be due to the increasing laser power detrimentally affecting sensitivity due to intensity noise with increased laser power, which does not degrade C_1 to the same degree. These trends suggest that either cost function is suitable for optimisation if intensity noise is taken into consideration.

The predicted cost-landscapes for A_{Mod} and F_{Mod} (Figure 4.4) show broad trends with large confidence intervals, suggesting that the relationship between these parameters and the cost functions are not well-defined. Table 4.2 shows in the results for optimisation scheme 4 (C_2, $M = 5$) that the optimised values for modulation

amplitude and frequency gave a modulation index within the expected optimal values (m_i =0.5 − 1). While clear gains in sensitivity were provided by increasing the number of parameters optimised, C_2 is advised for directly optimising sensitivity while keeping modulation values within expected optimal conditions.

It is interesting to note that the optimal detuning parameter found is positively detuned from the optical absorption peak (Table 4.2), in direct contrast to the negatively detuned value selected by the skilled operator. It appears that the effect of the buffer gas introduces complex optical pumping dynamics in the atomic system, likely tied to depopulation of the $F = 3$ ground state. The results of the MLA techniques show that the detuning and power dependence are non-trivial. These results may vary depending on cell parameters such as the optical path length and buffer gas pressure.

4.4 ML optimisation of hardware

The ML techniques demonstrated in Section 4.2.2 are suitable for applications beyond experimentally controlled parameters, and can also be used to quickly characterise the sensitivity impacts of any hardware changes. In this section, a number of atomic vapour cells are characterised in an efficient and comprehensive manner utilising the demonstrated ML toolkit, to optimise the SERF magnetometer sensitivity. A range of cells with varying nitrogen buffer gas pressure were constructed [69], with each cell identical otherwise. Each cell had internal dimensions of 6 × 6 × 3 mm^3 and a buffer gas range of 95 − 225 Torr, at 85 °C [121], was utilised to allow the relationship between buffer gas pressure and sensitivity to be explored.

The relationship between buffer gas pressure and the relevant relaxation mechanism are well understood, as described in Section 2.5. There is an observable minimum point at which total relaxation, Γ_{Total}, is the smallest with respect to buffer gas pressure (shown by the dip in the solid line in Figure 4.5). This point is often cited as the optimum quantity of buffer gas required to optimise sensor performance. However, the relationship between buffer gas and magnetometer performance, particularly sensitivity, is not extensively explored within the literature

beyond the assertion of a relation to the total rate of relaxation.

In order to empirically quantify the effect of buffer gas pressure on magnetic linewidth and magnetometer sensitivity, a range of buffer gas pressures are analysed. Here, rapid testing is aided by the design of the portable sensor, described fully in Chapter 5. The portable sensor package is modular in construction which allows for easy component replacement, including the atomic vapour cell. In practice, changing the atomic vapour cell within the portable sensor takes less than 5 minutes. To isolate only the effect of buffer gas on sensitivity, all other components of the experimental set-up remain unchanged, including the optics, laser and driving electronics etc.

In total, five atomic vapour cells with distinct pressures are tested, spanning a range of nitrogen buffer gas pressures (95, 125, 185, 211 and 225 Torr). Each vapour cell is installed into the sensor sequentially and two distinct types of measurements, M, are taken:

M1: Firstly, the cell is heated to 90 °C to extract the intrinsic linewidth (through the methods described in Section 2.4.5). Direct measurement of the intrinsic linewidth allows for direct comparison of the experimentally found values (black crosses) with the modelled values (solid black line), which shows good agreement. This suggests that the definition of the relevant relaxation mechanisms is correct for the atomic vapour cell with respect to the atomic species, buffer gas pressure and geometry.

M2: The genetic algorithm, presented in Section 4.2.3, is applied to optimise the sensitivity of the single-beam caesium SERF OPM. The genetic algorithm automatically optimises all 5 operational parameters, described in Section 4.2.6. Here, optimisation is based on direct measurement of sensitivity across the defined frequency band of interest (5–20 Hz), cost function 2, C_2. Optimisation of all the operational parameters is required as the optimal values will vary depending on buffer gas pressure.

The results of both of these measurements for all atomic vapour cells are illustrated in Figure 4.5. The black crosses denote the measured relaxation, Γ, and the

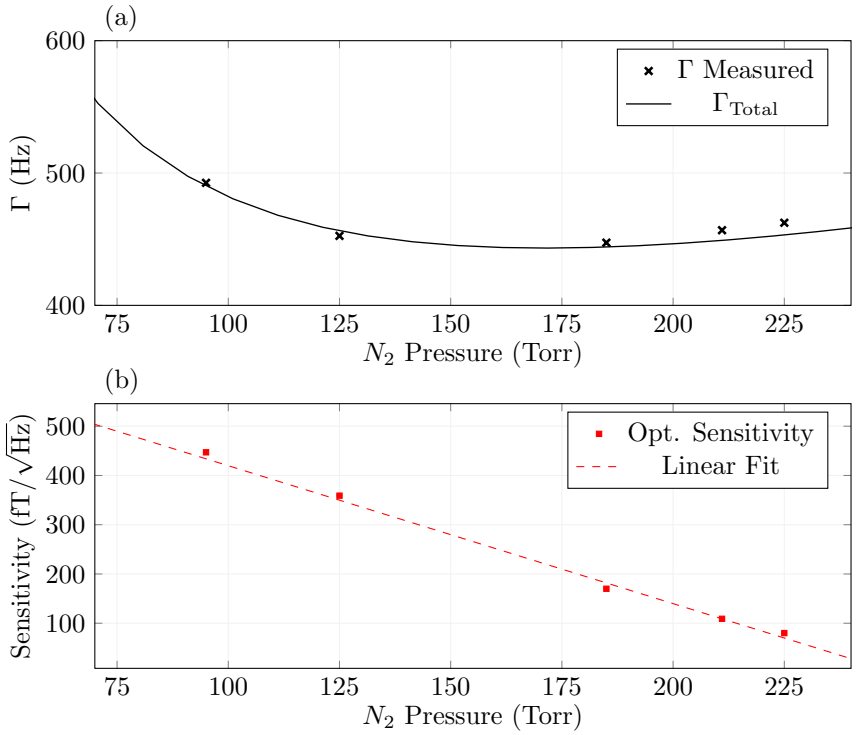

Figure 4.5: Intrinsic linewidth and sensitivity measured for a range of MEMS atomic vapour cells, with internal dimensions of $6 \times 6 \times 3$ mm^3. Five atomic vapour cells with distinct pressures are tested, spanning a range of nitrogen buffer gas pressures ($95, 125, 185, 211$ and 225 Torr). **a)** Intrinsic linewidth, Γ, extracted for each cell with the measured value, Γ Measured, indicated by crosses and the modelled response, Γ_{Total}, found using Equation (2.26). **b)** Optimised sensitivity of the caesium SERF OPM using a 250 loop 5 parameter genetic algorithm as the MLA. Linear fit (dashed) applied to measured optimal sensitivities (squares).

solid line represents the modelled relaxation rate, Γ_{Total}, (described in Section 2.4.5). The red dots and dashed line refer to the sensitivity measurements. The red dashed line indicated a linear model fit to the peak found sensitivity values with respect to buffer gas pressure, P, to a high accuracy ($R^2 = 0.974$). The linear model allows for the extraction of the derivative of sensitivity, S, with respect to pressure, P, such that $\frac{\delta S}{\delta P} = 3$ fT/$\sqrt{\text{Hz}}$ per Torr of buffer gas added to the atomic vapour cell.

4.4.1 ML optimisation of hardware: Discussion

The effect of nitrogen buffer gas pressure within caesium MEMS fabricated silicon cells with internal dimensions of $6 \times 6 \times 3$ mm^3 has been explored to better understand the consequences of buffer gas pressure on sensor sensitivity. Figure 4.5 allows for easy comparison of the total relaxation, Γ, with respect to buffer gas, and the measured optimal sensitivity with respect to buffer gas. The optimal sensitivity is found at 90 fT/$\sqrt{\text{Hz}}$, correlating to the atomic vapour cell with the highest pressure of nitrogen buffer gas (225 Torr). However, the smallest relaxation is measured in the atomic vapour cell with 185 Torr of nitrogen buffer gas. Thus, the assertion that the point of minimised total relaxation correlates to the point of optimal sensitivity has been proven incorrect through direct measurement.

The linear gain in sensitivity with respect to buffer gas, as indicated by the blue dotted line in Figure 4.5, highlights the need to characterise the sensitivity of atomic vapour cells with further increasing pressures of nitrogen buffer gas. A limit must exist in which buffer gas pressure begins to detrimentally effect the sensitivity of the magnetometer, which would be interesting to find and identify. To that end, further research here exists to locate the optimised pressure of nitrogen buffer gas for the caesium SERF magnetometer.

Chapter 5

A portable OPM for biomagnetic sensing

The production of an ultra-sensitive SERF OPM for the eventual use in biomagnetic sensing tailors the requirements for the sensor to target the shortcomings of classically used SQUID-based systems. SQUID-based systems are bulky and costly due to operationally required cryogenics. As such, SQUID-based systems lack adaptability due to fixed sensor placement, leading to the loss of signal intensity particularly for participants with smaller physiology. The participant is also unsecured with respect to the sensor which leads to movement artifacts during measurements. A required thermal isolation from the cryogenics sets a fixed minimum distance from sensors to the participant ($\simeq$ 2 cm for low T_c SQUIDs) [122, 123] which further increases the average distance between sensor and signal source, to the detriment of the signal amplitude.

The sensing head of the magnetometer used from biomagnetic measurements must be at a compact portable scale, to counter many of the issues of SQUID-based systems. Furthermore, portability is important to allow multiple sensors to be utilised simultaneously in arrays to provide spatial information of biomagnetic measurements, such as demonstrated for full head MEG [124, 125] and full chest MCG [126]. The portability of the OPM allows for use in a variety of settings, including both clinical and research environments. Small sized sensors allow for more

precise placement of the sensor with respect to the measured signal, such that positioning reduces the stand-off distance between the biomagnetic signal and the sensor, providing a superior SNR [127] in comparison to static SQUID-based systems. The reduced stand-off distance also means full head OPM systems require around half as many sensors than equivalent full head SQUID-based systems (typically requiring $\simeq 300$ sensors [128]).

In this chapter, the challenges of highly sensitive sensor design and operation will be discussed in the specific context of the portable sensor head package. The full sensor head design, construction and test is described here with particular focus on miniaturised and microfabricated component design. The portable sensor is built to the specifications driven by the use in biomagnetic measurements in real-life applications.

5.1 Introduction

Measurements of magnetic fields generated by the human body provide a critical diagnostic and research tool [129–136]. Biomagnetic signal amplitudes are 6-9 orders of magnitude smaller than the earth's magnetic field of 50 μT, e.g. cardiac signals ($\sim$100 pT) and neural activity (between 10-500 fT). Advances in OPMs [28, 29, 31, 137] have led to demonstrations of sensors that approach the sensitivity of SQUIDs, while providing new measurement modalities [138] due to their size and portability, as well as improved source localisation [139] due to better head coverage [**?**,124,140]. Zero-field OPMs do not require cryogenic cooling, and the relative simplicity of the sensor design lends the sensor to miniaturisation, demonstrated by the availability and widespread use of several commercial sensors [138, 141].

The OPM designed here, as described in Chapter 3, utilises an atomic vapour cell that contains a vapour of caesium as the sensing atom. MEMS fabrication techniques [69, 121] have been used to manufacture this alkali vapour cell. These techniques create a very compact vapour cell with outer dimensions $10 \times 10 \times 4$ mm^3, whose optical access allows it to reside in a planar stack of components along the optical path of the laser beam.

Since the measured magnetic field decays as an inverse function of the distance cubed [142], it is advantageous to place the sensor in close proximity to the signal source, with sensor to skin contact therefore being highly desirable. Optically pumped magnetometers using alkali vapour must create a sufficient density of atoms in order to operate in the SERF regime. As a result, the atomic vapour cell must be heated to achieve a vapour density of $\simeq 10^{14}$ cm^{-3}, as discussed in Section 2.6.1. The surface temperature of the sensor package is of great importance, especially when many sensors are operated in an array around the head, as in MEG. Here, the sensor must also be capable of operating next to participants' skin in order to take biomagnetic measurements, while maintaining high thermal uniformity across the cell. The Electrotechnical Commission have set a maximum external skin-safe temperature of 41 °C for a device that has contact with healthy skin of an adult [53]. In the sensor described here, the decision to use caesium as the sensing atom was informed by the expected operating temperature required to achieve optimal sensitivity, which is $\simeq$ 30 °C lower than that of rubidium, due to the higher vapour pressure of caesium. Effective insulation is also employed to attenuate the heat from the atomic vapour cell before reaching the sensors external face, discussed in Section 5.3.

OPMs of the type described here must operate close to zero-field. Typically much of the Earth's field is attenuated using shielding such as a MSR, which is commonly used for biomagnetic measurements in hospitals and research institutes. Approximately 10-50 nT of residual field remains in even high specification MSRs [72]. The remaining environment magnetic fields can be compensated within the sensor package using coil pairs that act on each axis.

This chapter will cover the design, development and testing of a caesium portable zero-field OPM, with particular focus on mircofabricated components to aid portability. This sensor has demonstrated biomagnetic measurements of the human heart and has broad applicability in the measurement of other small biomagnetic signals.

5.2 Portable sensing package design

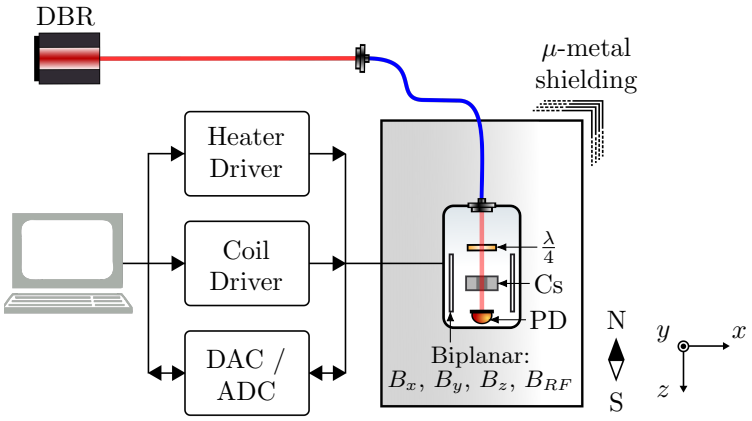

Figure 5.1: Experimental setup. Elliptically polarised light from a DBR laser close to the $F = 4 \rightarrow F' = 3$ hyperfine transition of the caesium D_1 line is fibre-coupled to pass through a micro-fabricated atomic vapour cell [69] filled with a saturated vapour of caesium and 211 Torr of nitrogen buffer gas. The cell is heated through resistive heating by square-wave modulated current provided by a custom high efficiency heater driver. Three pairs of coils, B_x, B_y, B_z, control the static magnetic field along each axis, and an additional modulation coil, B_{RF}, allows the application of an oscillating field along the y-axis. The static field coils are driven using a custom low-noise current driver [83]. The photodiode, photodetector (PD), measures light transmitted through the vapour cell. A low nT-level magnetic field environment is provided by a 5-layer μ-metal shield. Other components; $\lambda/4$, quarter waveplate; Cs, caesium vapour cell; ADC; digital-to-analog converter (DAC).

The topology of the prototype caesium portable sensor configuration is presented in Figure 5.1. The sensor head is enclosed in a five-layer mu-metal shield during development and testing, though due to its size and portability, it was easily moved to an MSR. Laser light from a DBR laser tuned to the caesium D_1 line, $\lambda = 895$ nm, is delivered to the sensor head via an optical fibre. The fibre-coupling port is labeled as FC and fits a non-magnetic fibre collimator (Schäfter Kirchhoff 60FC-4-M12-10-Ti), which is aligned within the package using a nylon retention screw. Figure 5.2(a) shows a photograph of the portable sensor head within the mu-metal shielding in the laboratory environment. The sensor is mounted, using custom 3D printed mounts in PLA, to align centrally in the shielding to reduce the effects caused by any remaining magnetisation of the inner shield.

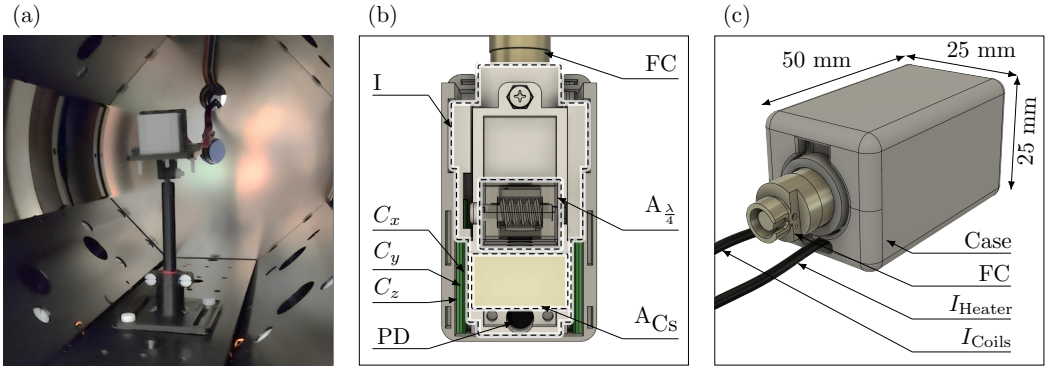

Figure 5.2: **a**) Photograph of the portable sensor inside a 5-layer magnetic shield. **b**) CAD model (top-view) of the sensor head. I: Insert containing optics and vapour cell; C_x, C_y, C_z: Bi-planar coils for uniform magnetic field control across each axis; PD: Photodiode, for detection of the light after it passes through the cell; A_{Cs}: MEMS cell heating assembly, containing caesium vapour cell, heating resistor and insulation; $A_{\frac{\lambda}{4}}$: Adjustable quarter-waveplate assembly; FC: non-magnetic fibre coupler with collimating lens. **c**) CAD model of the external faces of the sensor package. Case: 3D printed external package casing; I_{Heater}: Shielded cable for heating currents, I_{Coils}: shielded cable for coil currents and photodiode signal.

The driving and control electronics, including the DAQ unit, coil driver, and cell heater, are located outside the mu-metal shield. The control and detection signals are brought to the sensor-head on a cable bundle of individually shielded twisted pairs, as seen in the back of Figure 5.2(a).

To compensate for stray fields experienced at the cell, electromagnetic coils are placed within the sensor package to generate fields in three directions. It is of critical importance that the current does not generate excess magnetic field noise which would degrade the sensitivity of the sensor. These coils are driven using a custom ultra-low noise current driver, developed within the group and reported in [83].

The top-view diagram of the sensor head in Figure 5.2(b) shows several key components. The optical components are housed in a 3D-printed optical insert, I, which locates the vapour cell, fibre coupler with collimating lens (FC), the adjustable quarter-waveplate assembly ($A_{\frac{\lambda}{4}}$) and photodiode (PD). The optical insert allows for consistent alignment of optical components precisely with respect to the 5 mm diameter optical path through the sensor.

The external-view diagram of the sensor head in Figure 5.2(c) shows the 3D

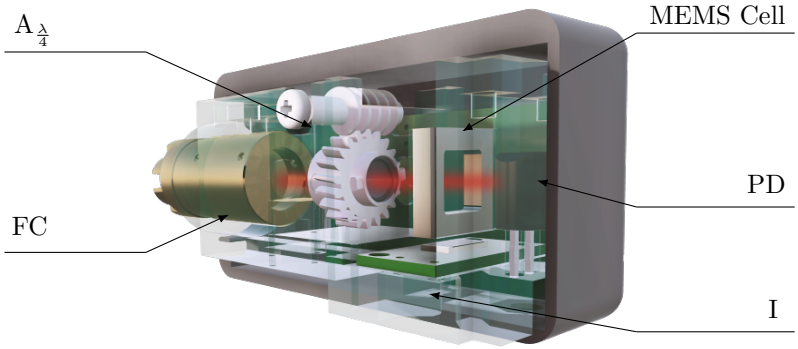

Figure 5.3: 3D Render of V1 the portable sensor from a cross-sectional view lengthways through the sensor. The red line indicates the path of the laser light. $A_{\frac{\lambda}{4}}$; adjustable quarter-waveplate. FC; fibre coupler with collimating lens. PD; photodiode. I; 3D-printed optical insert to align all optical components with respect to the laser light.

printed sensor case with external dimensions of $25 \times 25 \times 50\,\mathrm{mm}^3$. The interfacing cables for the heater current, I_{Heater}, and coil currents, I_{Coils}, are indicated with reference to the sensor package.

CAD modelling of the entire sensor and all components allows for the production of renderings that provide views of the sensor that are not possible with the physical package, as seen in Figure 5.3. Here, Figure 5.3 illustrates the path of the DBR laser light, indicated in red, from the fibre coupler, through the quarter waveplate assembly, $(A_{\frac{\lambda}{4}})$, through the atomic vapour cell and onto the PD, in a straight line. The alignment of all these critical optical components is ensured through the 3D-printed optical insert, I.

Furthermore, the exploded-view diagram of the sensor head in Figure 5.4 illustrates how the various components discussed are assembled within the sensor head. Each part will be discussed in the following sections. All components are aligned through push-fit retention, with the exception of the fibre coupler which utilises a nylon retention screw. The retention screw is also used to ensure the fibre coupler is consistently aligned if removed and replaced, as a screw-hole in the fibre coupler acts as a key-way when combined with the retention screw, to ensure consistent polarisation. By creating a sensor with non-permanent fasteners and retention

methods, I am quickly able to swap out any part of the sensor if required, such as for optimisation as discussed in Section 4.4.

5.3 Cell heating assembly

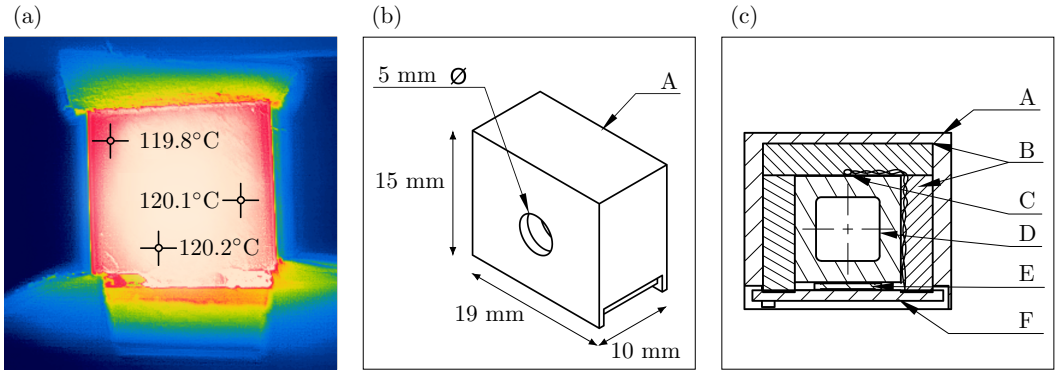

Figure 5.5: Design of the caesium MEMS cell heating assembly. **a**) Photograph of the caesium MEMS cell outside of the printed cell housing, only insulated on the top side, heated to 120 °C. Pictured with a thermal camera, colour indicates temperature from coolest (blue) to hottest (white/red). **b**) Drawing of the external cell oven assembly. **c**) Cross-section of oven, insulation and cell. A: 3D printed cell housing, B: Calcium-magnesium silicate thermal insulation, C: T-type thermocouple, D: caesium 3mm MEMS cell, E: Non-inductive SMD resistor, F: Heater interface PCB.

At the core of the portable sensor is a MEMS fabricated silicon cell (external dimensions $10 \times 10 \times 4$ mm^3), with 3 mm of silicon sandwiched between two layers of 0.5 mm borofloat glass, resulting in a 3 mm optical path length and 6×6 mm^2 optical aperture. The cell contains a vapour of caesium and nitrogen (N_2) buffer gas, which has been achieved by depositing droplets of caesium azide (CsN_3) in the vapour cell before the final glass bond is made in a nitrogen environment [121]. After sealing, the caesium azide is dissociated using UV. The resultant composition is a saturated caesium vapour and 225 Torr of nitrogen at 85 °C [121]. As discussed in Section 2.5, the presence of N_2 suppresses the rate of wall collisions and extends the lifetime of the atomic coherences by altering the mean free path of the alkali atoms, making their effective motion diffusive rather than ballistic with respect to the cell [143].

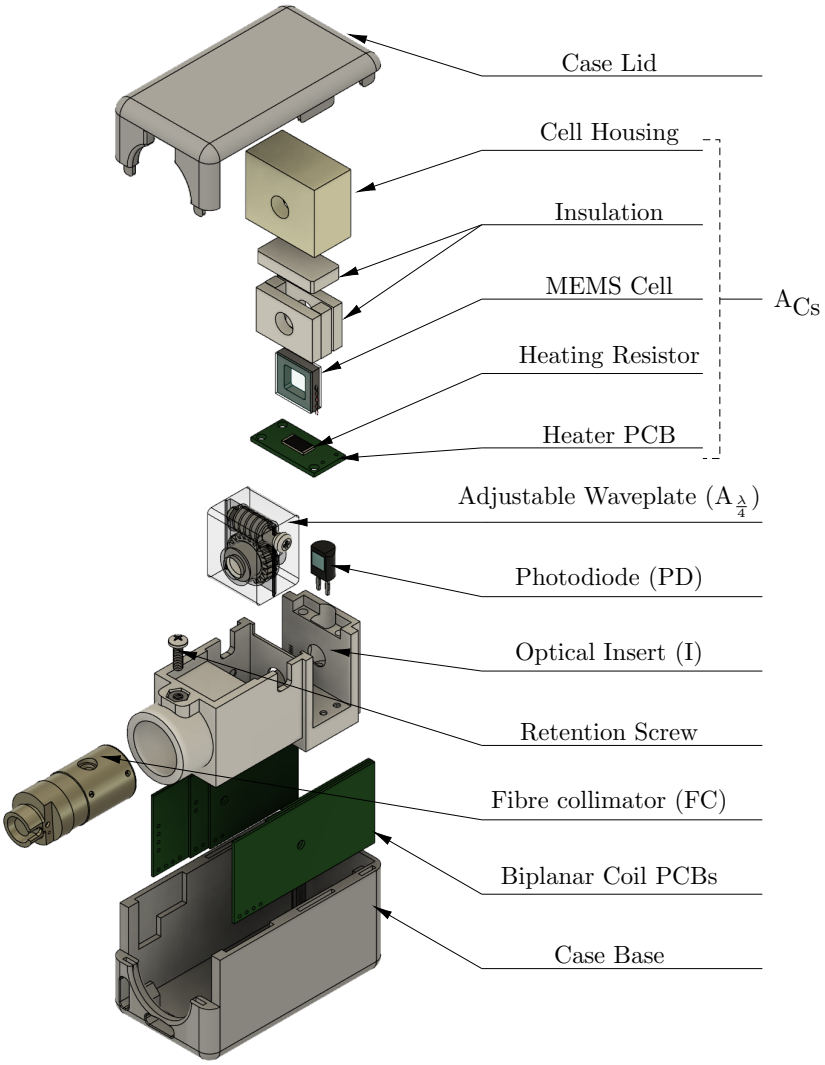

Figure 5.4: 3D Render of an exploded view of the portable sensor to illustrate assembly. The 3D printed case houses all the sensor components. Into the base fits the Bi-planar coils (C_x, C_y, C_z) for uniform magnetic field control across each axis. The optical components are housed in a 3D-printed optical insert, I, which locates the non-magnetic fibre collimator (FC) which is retained with a nylon retention screw, the adjustable quarter-waveplate ($A_{\frac{\lambda}{4}}$), the photodiode (PD), and the MEMS cell heating assembly (A_{Cs}). The MEMS cell heating assembly consists of the heating resistor, soldered to a custom heater PCB, and thermally bonded to the MEMS cell. The cell is insulated with custom cut insulation on all sides, leaving a 5-mm diameter aperture for optical axis, through the cell. The insulation is housed in the 3D printed cell housing.

For optimal sensitivity, the sensor must operate in the SERF regime which is achieved through heating of the atoms to a sufficiently high atomic density to suppress the effect of spin-exchange relaxations, as discussed in Section 2.6. Typical atomic vapour pressures, to achieve the SERF regime are $\simeq 10^{14}$ cm^{-3}, which in caesium corresponds to 100 - 120 °C [29, 30, 51, 92].

The vapour cell is heated ohmically through direct contact with an aluminum nitride non-magnetic thin-film resistor (PN: PCNM2512K8R20FST5) as a heating element (Figure 5.5(c)), thermally bonded to the MEMS cell surface using boron nitrate paste and driven by a high efficiency AC driver at 274.699 kHz, a frequency chosen in order to avoid aliasing with respect to the mains frequency, far outside the bandwidth of interest of the OPM. The heating element covers a total heating surface area of 20.2 mm^2 equating to 67% coverage of the MEMS cell bottom-edge surface and resulting in rapid heating. Figure 5.5(a) demonstrates the high thermal uniformity (<0.5 °C thermal gradient) across the cell achieved through the described ohmic-heating methods, as pictured with a thermal camera (Seek SKU: LW-AAA).

The vapour cell is insulated with calcium-magnesium silicate thermal insulating sheets (3-mm thick) across all faces and housed in a 3D printed enclosure to create an insulated oven (Figure 5.5(b)). The printed enclosure is manufactured using a Formlabs printer in High-Temperature V2 resin with a heat deflection temperature of 238 °C at 0.45 MPa, ensuring that even at an operating temperature of 120 °C, the oven will not deform. Closed loop temperature feedback allows for stable heating, using a non-magnetic T-type thermocouple mounted to the top of the cell (Figure 5.5(c)) for temperature monitoring and a PID controller for temperature control, as discussed in Section 3.2.4. The distance from the sensing area inside the cell to the outside of the package measures 12 mm.

To test the requirement of a skin safe external sensor surface, the atomic vapour cell is ohmically heated to a set temperature of 120 °C that is maintained for long periods through closed-loop PID temperature control. The temperature of the cell, T_{Cell}, and the external face of the sensor, T_{Outer}, are measured directly using two T-type thermocouples. Figure 5.6 shows the measured temperature responses. The

time period shown here, >90 minutes, simulates sustained sensor operation.

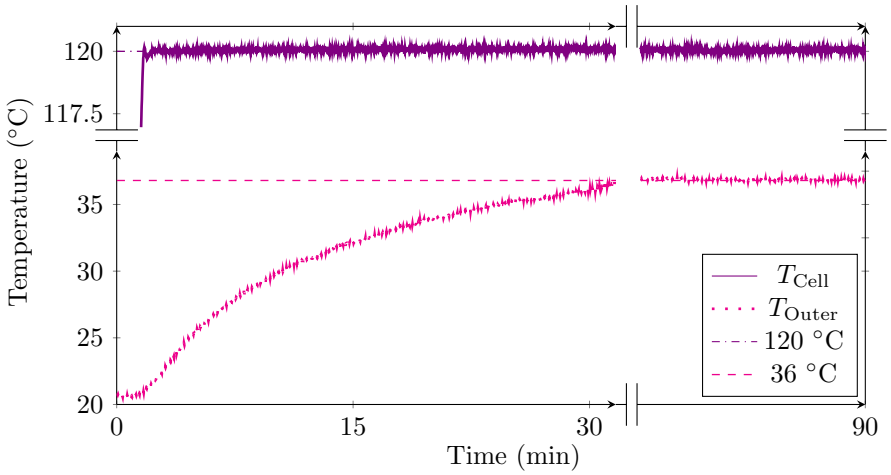

Figure 5.6: Temperature measurement (via T-type thermocouple) of the portable caesium sensor for 90 minutes of cell heating, at the desired cell temperature ($T_{\text{Cell}} \simeq 120$ °C). Ambient temperature $\simeq$ 22 °C. The initial cell temperature $T_{\text{Cell}} \simeq 25$ °C and the initial external face of the sensor temperature $T_{\text{Outer}} \simeq 21$ °C. Measured temperature of caesium MEMS cell (T_{Cell}), (solid line) and external face of 3D printed case of the sensor T_{Outer}, (dotted). Set temperature (dot-dashed) and saturation temperature of sensor external face (dashed).

The PID heating system quickly reaches the cell set temperature in ∼100 seconds and maintains a consistent (±0.5 °C) temperature throughout 90 minutes duration once the set temperature is reached. The tuned PID parameters achieve an overshoot of $\leq$ 0.5 °C.

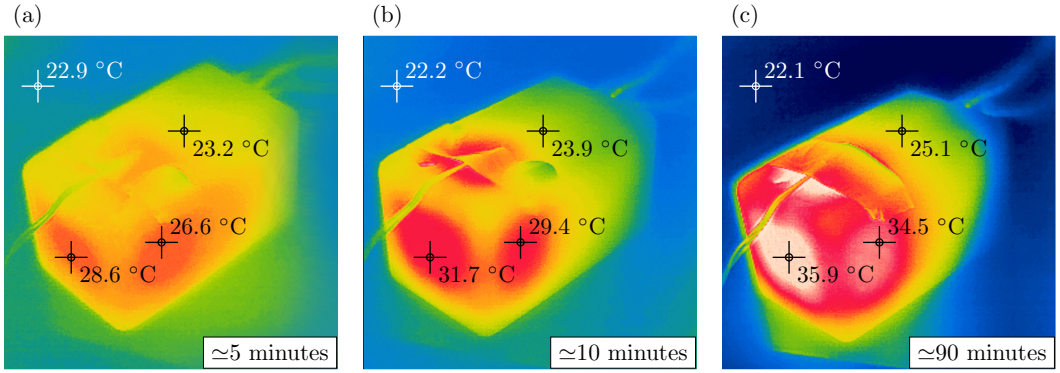

Figure 5.7: Temperature testing of the portable caesium sensor for 90 minutes of cell heating, at the desired cell temperature (120 °C). The sensor external faces are pictured with a thermal camera, colour indicates temperature from coolest (blue) to hottest (red), at various points during the heating test. **a)** $\simeq$ 5 minutes, **b)** $\simeq$ 10 minutes and **c)** $\simeq$ 90 minutes.

The sensor package's outer surface saturates at a temperature of 36 °C, indicated by the pink dashed line in 5.6(a), within 30 minutes. Figure 5.7 shows the sensor external faces pictured with a thermal camera (Seek SKU: LW-AAA) at various times during the heating test ($\simeq$ 5, $\simeq$ 10 and $\simeq$ 90 minutes), where the hot-spots of the portable sensor's surfaces are indicated in red and white.

5.4 Angular control of a quarter waveplate

Typically single-beam zero-field sensors require a circular component of polarisation for efficient optical pumping [57]. However, we have experimentally found that the sensor signal is improved through the use of elliptically polarised light. A quarter-waveplate is used to convert linearly polarised light from the fibre to elliptically polarised light before passing through the MEMS cell. To allow for investigation of the optimal angle of the quarter waveplate, the sensor was designed to allow for precise rotation of the waveplate. A custom design was required for the adjustable mechanism for rotation because an appropriate commercial equivalent at a compact scale, constructed from non-magnetic material, does not currently exist.

5.4.1 Adjustable waveplate design

The adjustable waveplate achieves rotation by utilising a geared mechanism. The selection of the gear type depends on the required configuration of the drive gear and driven gear. In this use-case, access to any rotation mechanism once inside the sensor package is constrained to only be accessed at 90 ° to the driving gear. Worm gears are most suited to this orientation and provide high rotation precision for a small footprint. The worm gear ratio, i, quantifies the resolution or precision of the rotation and is defined by the number of gear teeth of the worm gear, n_1, and the number of helical threads that span the length of the shaft of the worm drive gear, n_2, where $i = \frac{n_1}{n_2}$.

Figure 5.8 shows the full adjustable quarter-waveplate design ($A_{\frac{\lambda}{4}}$). Here, the waveplate is a 5-mm diameter quarter-waveplate. Figure 5.8(b) shows the worm drive gear which has a single helical thread such that one turn of the worm drive causes an advance of one tooth of the worm gear, $n_2 = 1$, controlled through the turning of a nylon screw embedded along its length. The worm gear is a 20 toothed gear, $n_1 = 20$, with an external diameter of 10 mm. The subsequent gear ratio, $i = 20{:}1$, equates to 5 turns of the worm drive to give a $\pi/2$ retardation, moving from fully linear to fully circular polarisation.

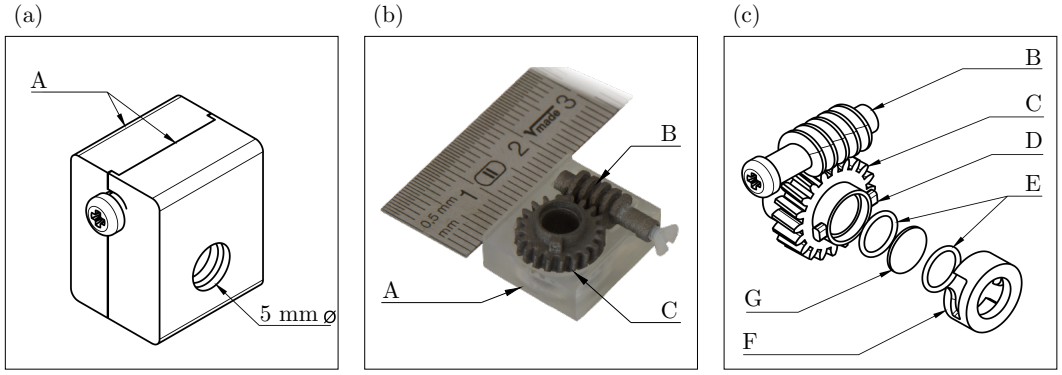

Figure 5.8: Design of adjustable quarter-waveplate ($A_{\frac{\lambda}{4}}$) **a**) isometric, **b**) part assembled and **c**) exploded views. **b**) Photograph of titanium printed rotating waveplate mechanism. A: 3D printed enclosure consisting of two push-fit parts with external dimensions ($17 \times 14 \times 12$ mm^3). B: Worm drive gear. C: Worm gear where $n_2 = 20$ and external diameter = 10 mm. D: Locating extrusions for retention cap. E; 5.2 mm diameter O-rings. G; 5 mm diameter quarter-waveplate. F: Waveplate retention cap.

Figure 5.8(a) shows external faces of rotating quarter-waveplate assembly with total external dimensions of $17 \times 14 \times 12$ mm^3. The enclosure for all rotating components consists of two push-fit parts. In Figure 5.8c all internal components can be seen, exploded along the optical axis. The waveplate and gears must be insensitive to movement as vibration of the waveplate can couple as polarisation noise into the sensing atoms. To dampen vibration, two O-rings (5.2 mm external diameter) are used to sandwich the quarter-waveplate into an internal ledge carved into the worm gear, this is all secured by a retention cap that is notched to correspond with 2 locator notches added to the worm gear.

All components (Figure 5.8c) of the adjustable quarter-waveplate design must be entirely non-magnetic due to their close proximity to the sensing atoms within the sensor package. The worm gear and drive gear require the highest accuracy, robustness and finest resolution, as the minimum tooth resolution is defined by the production method. These components are produced using titanium 3D printing (25 μm minimum print resolution) by a commercial supplier. The choice of titanium means wear and tear of the gear teeth is not a concern. The enclosure and retention cap are 3D printed in Formlabs Grey Pro engineering resin (50 μm minimum print

resolution).

5.4.2 Fine polarisation control

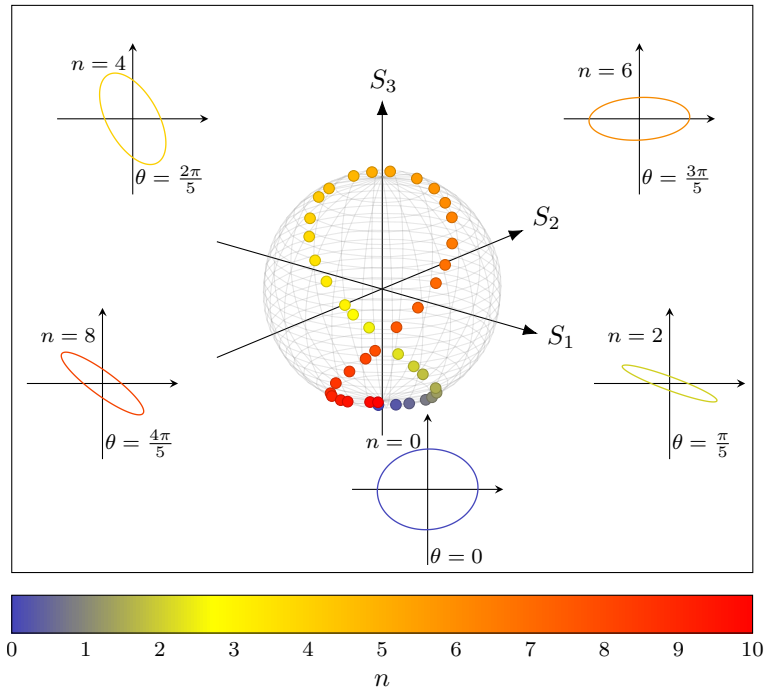

Figure 5.9: Light polarisation corresponding to number of worm drive gear turns (n) and angle (θ) between the waveplates axis and the plane of polarisation. Measured state of polarisation mapped onto the Poincaré Sphere, based on measured Stokes parameters (S_1, S_2, S_3) [144]. Colour indicates the number of turns of the worm gear (n). Inset are polarisation ellipses, constructed for 0, 2, 4, 6 and 8 turns,

The performance of the fabricated design described in Section 5.4 is seen in Figure 5.9. To test the polarisation, the rotating waveplate is mounted external to the sensor package to allow a laser source to pass directly through the assembly optical aperture. The resultant light is measured using a commercial polarisation analyser (Schaefter-Kirchoff SK010PA-VIS). In quarter-turn increments, the worm drive gear is rotated using a nylon screw embedded along the length of the titanium worm gear drive, and the Stokes parameters (S_1, S_2, S_3) [144] and degree of polarisation, p, are recorded at each point.

Figure 5.9 shows polarisation changes smoothly and reliably with rotation of the

worm drive gear, with varying ellipticity. The polarisation ellipses at 0, 2, 4, 6 and 8 turns are displayed as insets, to demonstrate shifting ellipticity with respect to worm gear and waveplate rotation. The polarisation, starting at $\theta = 0$, is expected to wrap back around to this polarisation at $\theta = \pi$ which is demonstrated through the measured polarisation with respect to rotations of the worm drive gear, $n = 10$. Thus, the gear ratio ($i = 20{:}1$) is demonstrated.

The adjustable rotating waveplate assembly, once installed into the caesium portable sensor, is operated through manually turning the worm drive screw. Due to the small size of the sensor package, it is not possible to measure the polarisation of the laser light inside the sensor with a commercial polarisation analyser. As such, selection of the optimal polarisation is aided through interrogation of the direct response of the atoms. This is achieved by continually sweeping the transverse Hanle resonance, as described in Section 2.6.3, and measuring the resonance peak signal amplitude, A_0, with respect to the background signal, C, (Equation (2.38)). The measured amplitude $(A_0 - C)$ is optimised by slowly turning the worm gear drive in the direction that maximises this value, correlating to the optimal polarisation. Experimentally we find the optimal polarisation is elliptical [57, 145].

5.5 Small footprint coil design

The SERF OPM sensor requires three-axis control of the magnetic field in the region of the cell to maintain a zero-field environment. The coils described here are designed as a custom component for assembly within the sensor package to occupy as small a footprint within the sensor as possible without obscuring the beam path.

In order to minimize the footprint of the required coils, a deviation from the typical Helmholtz configuration is necessary as 3-axis Helmholtz can be obstructive to the beam axis and require a large footprint, as illustrated in Figure 5.10.

Bi-planar coils allow multi-axis magnetic field control while all coils are oriented in a single plane. As such, bi-planar coils occupy a smaller footprint than a traditional Helmholtz design. Bi-planar coils have been utilised in zero-field sensing both within an OPM sensor package [73] and external to the sensor through ac-

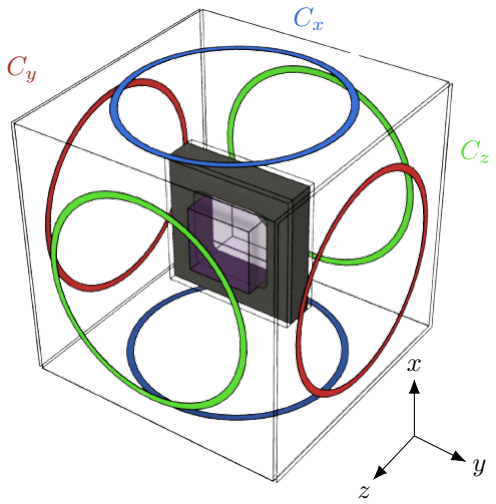

Figure 5.10: Helmholtz coil pairs C_x, C_y and C_z, indicated by colour (blue, red and green respectively), apply homogeneous fields across the x, y and z axes. Each coil pair is separated by distance 20 mm. A defined homogeneous sensing region (shown in purple) is centered between the coils which requires high homogeneity throughout, shown with respect to a caesium MEMS Cell (external dimensions, $11 \times 11 \times 5$ mm^3).

tive field control inside a MSR [72]. However, while the calculation of the magnetic field produced by the Helmholtz coil configuration is relatively straightforward using Equation (3.1), the calculation of fields and wire routing for bi-planar coils is much more complex. In such cases, open source software called bfieldtools [146, 147], a specialised python package designed for calculating the current loops required to create a B-field in complex geometries based on the specific constraints on the user, can be a valuable tool. Bfieldtools can be used to define current loops, through a well defined process [73], discussed further in Section 5.5.1, that produce a magnetic field in the desired direction across a specified sensing region. For this use-case, bfieldtools is used to create the coils C_x and C_z. A Helmholtz configuration is used for C_y due to the relative computational ease required to produce a good solution with the desired field and homogeneity. Circular geometry Helmholtz coils were selected as curves are more manufacturable to PCB than geometries with right angles.

Figure 5.11(a) shows all three bi-planar coils with respect to the caesium MEMS cell and a defined sensing area (shaded square), where red and blue indicate opposing current directions, either clockwise or anti-clockwise. Each coil pair is positioned

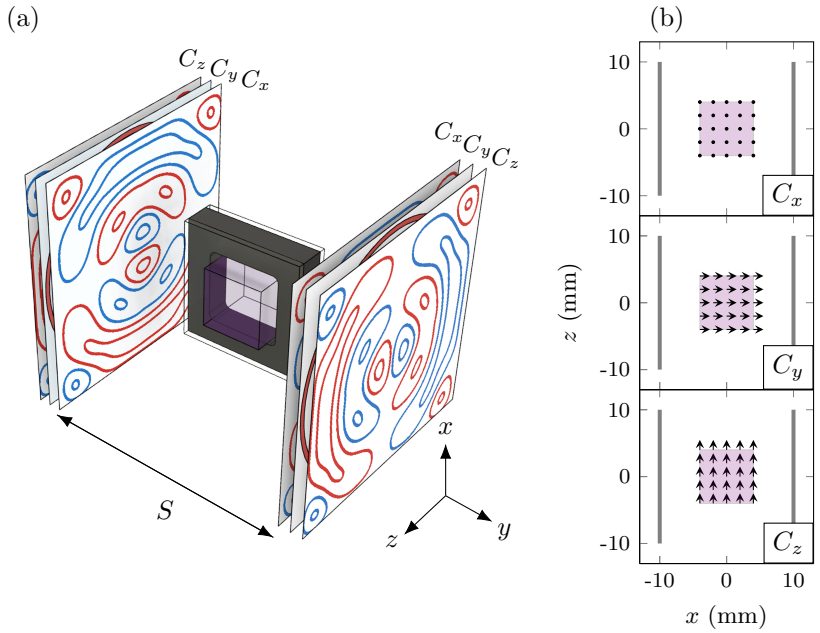

Figure 5.11: Coil pairs C_x, C_y and C_z apply homogeneous fields across the x, y and z axes respectively. Each coil pair is separated by distance $S = 20$ mm, red and blue indicate opposing current directions. Coils are designed for a defined homogeneous sensing region (shown in purple) centered between the coils which requires high homogeneity throughout. **a**) All three coil pairs location with respect to caesium MEMS Cell (external dimensions, $11 \times 11 \times 5$ mm^3). **b**) Coil pair location is indicated by grey lines, vector arrows across the sensing region show individual coil pair magnetic field direction.

symmetrically about the sensing area. The details of each coil will be given shortly, in Section 5.5.2. Figure 5.11(b) illustrates the direction (indicated by the vector arrow) of the homogeneous magnetic field produced by each coil (C_x, C_z and C_y) across the sensing area (in purple), between a coil pair separated by distance S across the yz-plane.

5.5.1 Bi-planar coil design process

The process for designing a coil using bfieldtools involves the following steps, demonstrated by the prototype seen in Figure 5.12:

1. Specifying the geometry, sensing area, and field direction of the coil.

2. Using bfieldtools stream-function optimisation to generate a surface current

map, Figure 5.12(a).

3. Converting the surface into current loops, with the number of loops, N, determining the complexity of the design, Figure 5.12(b) where $N = 4$.

4. Extracting the field-to-current ratio, β_{Modelled}, and homogeneity of the design. Homogeneity of the modelled field is illustrated in Figure 5.12(c) by the vectors indicating field direction and amplitude across a central cubic sensing area.

5. Combining the individual loops into a single coil current path that can be produced through wire or PCB. A 3D modelled coil former for coil winding is illustrated in Figure 5.12(d).

6. Fabricating the optimised coil design. A photograph of the hand wound coil using the coil former is shown in Figure 5.12(e) using 22 american wire gauge (AWG) wire.

7. Testing and evaluating the coil's performance to ensure it meets the desired specifications, Figure 5.12(f). In this example a high precision fluxgate (Bartington, Mag-13MS60) was utilised to confirm B-field magnitude across all axes. In the sensor package, the homogenity will ultimately be tested by the atoms.

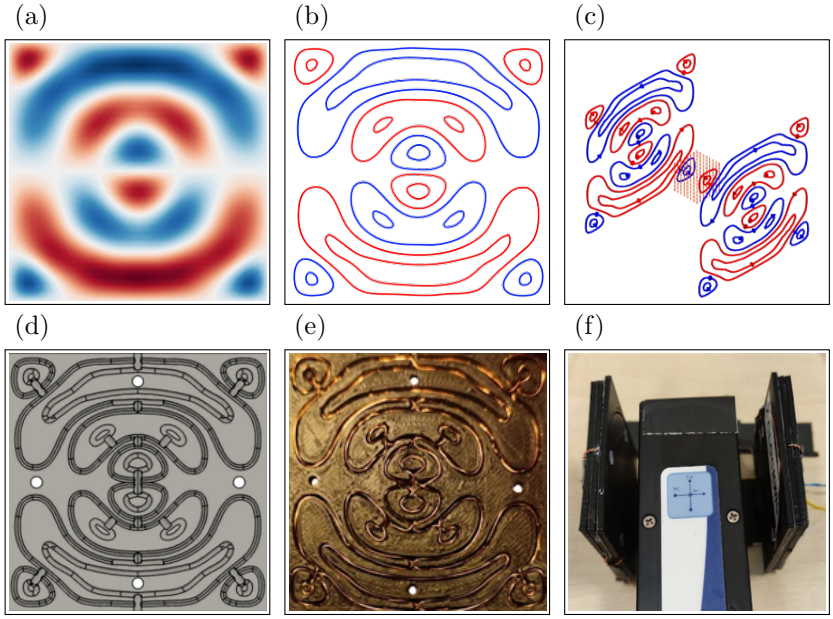

Figure 5.12: The process for designing bi-planar coils using bfieldtools. Red and blue indicate opposing current directions. **a**) A surface current map generated using bfieldtools stream-function optimisation. **b**) Current loops derived from the surface current map. The number of loops, N, determines the complexity of the design, $N = 4$. **c**) The field-to-current ratio extracted from the current loops allows for estimation of field homogeneity across the sensing region. The vectors indicate field direction and amplitude across a central cubic sensing area. **d**) A 3D modelled coil former design for hand winding the individual current loops with a single wire. **e**) A photograph of the hand wound coil, using 22 AWG wire, in the coil former, 3D printed in PLA. **f**) A photograph of the testing setup to measure the coils field magnitude using a high precision fluxgate (Bartington, Mag-13MS60).

5.5.2 Bi-planar PCB

Field control across 3-axis of the portable caesium sensor is achieved through bi-planar coils seen in Figure 5.13, which sit on the yz-plane of the portable sensor, either side of the MEMS cell. By utilising the process described in Section 5.5.1, the bfieldtools package was used to design the coils along x-axis and z-axis, and a Helmholtz configuration was used on the remaining y-axis.

The current contours (Figure 5.13 (a),(d) & (g)) provide a homogeneous magnetic field across the defined sensing area in the desired direction. The homogeneity of the magnetic field produced across the sensing region for each coil design (C_x, C_y and

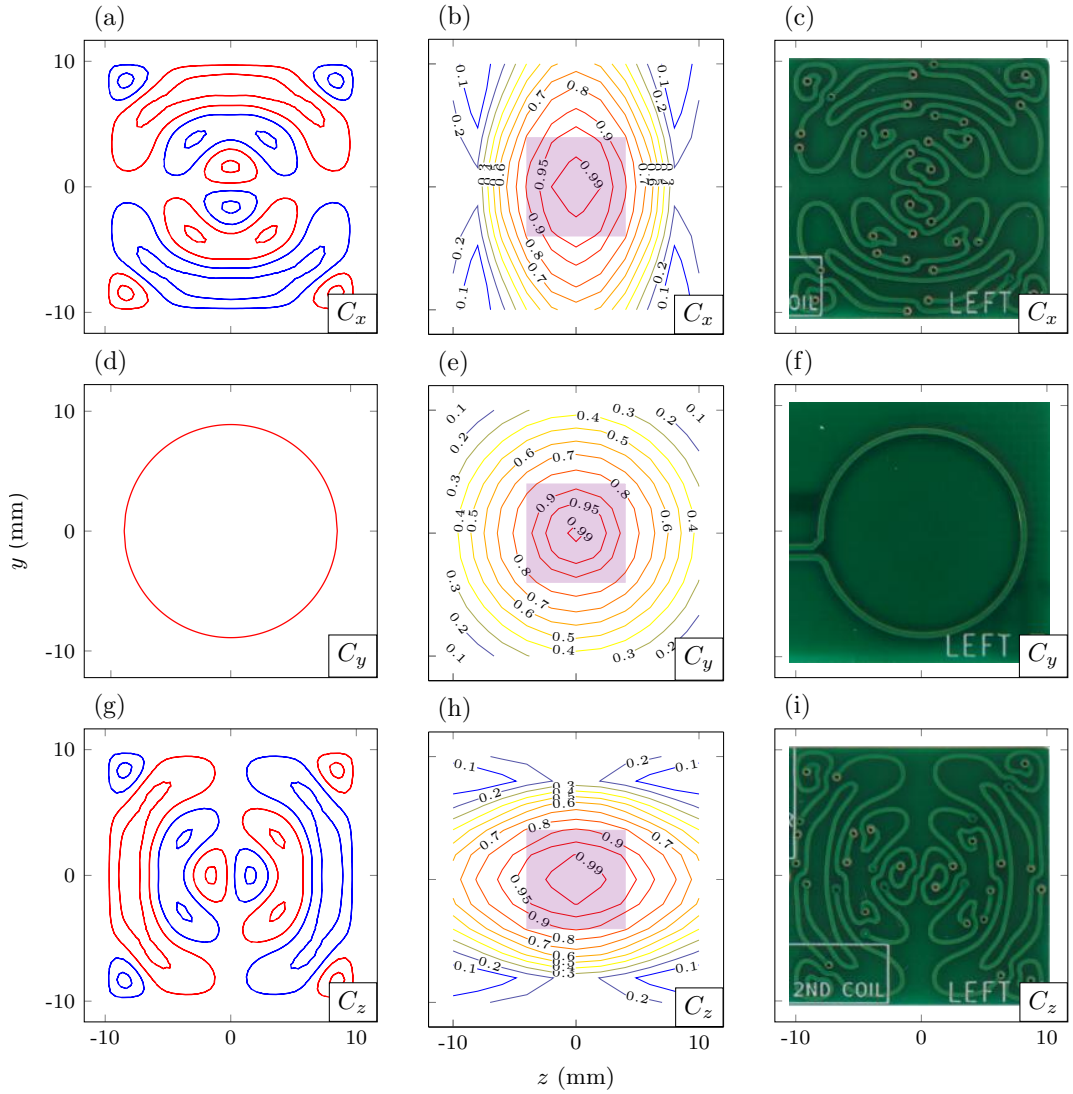

Figure 5.13: Version 1: 3-axis bi-planar coils assembled across the yz-plane of the portable sensor. Each axis (x,y and z) has a respective unique coil design C_x, C_y and C_z, indicated in each subplot. **a,d,g**) bfieldtools current contours ($N = 4$) produced for the specified desired field, red and blue indicate opposing current directions. **b,e,h**) modelled magnetic field homogeneity, based on the bfieldtools current contours, calculated across the full region between coil pairs, with sensing regions highlighted in purple. **c,f,i**) Photograph of manufactured PCB designed based on bfieldtools current loops shown in a,d,g.

C_Z) is modelled to verify the coil design suitability. Figure 5.13 (b),(e) & (h) show the modelled magnetic field homogeneity, based on the bfieldtools current contours, across the full region between the coil pairs on the yz-plane, where the sensing region (MEMS cell) is highlighted in purple.

PCBs are designed for each coil in KiCAD, in accordance with PCB design practices and manufacturer tolerances, as seen in Figure 5.13 (c),(f) & (i). An individual PCB is designed for each coil pair, with the coil contained within a 20×20 mm^2 area on the PCB. Each coil design is manufactured on a 0.4-mm thick 2-layer PCB. The coil pairs are installed in the portable sensor package in a configuration where 3 coils are stacked on each side of the sensor. Wire routing between corresponding coil pairs is achieved through manual wiring of 26 AWG twisted wire pairs. The expected magnetic field and homogeneity of PCB coils is confirmed through calibration by comparison of the measured magnetic resonance (through sweeping the magnetic field across one axis) with a well-calibrated external set of coils [148]. All coils produced fields within 1% of expected calculated values, Table 5.1 (described as V1 coils).

The PCB bi-planar coils shown in Figure 5.13, hereby referred to as V1, act as a proof of concept for the design and manufacture of the bi-planar coils. The results taken with the portable SERF OPM sensor throughout this thesis are taken with the sensor that uses the V1 coils. However, the field-to-current ratio, β_{Modelled}, is relatively low (Table 5.1). The current noise introduced by the coil driver is in the nA regime, leading to a maximum of $\simeq 40$ fT/$\sqrt{\text{Hz}}$ contribution in magnetic noise (for a 1 μT applied field), for the V1 coils. To reduce the effect of current noise, the field-to-current ratio can be improved by increasing the number of contours, N, in the bfieldtools definition (for the Helmholtz coil, N is the number of turns). Figure 5.14 illustrates the linearity of β_{Modelled} with respect to N, with the insets showing the coil designs for various numbers of contours, $N = 2, 4, 10$ and 20. The β_{Modelled} here is modelled for coils of equal geometry and sensing area, using bfieldtools. The insets of Figure 5.14 illustrate the a trade-off between complexity and manufacturability, as the higher contour designs (such as $N = 20$) are more intricate. In the context of

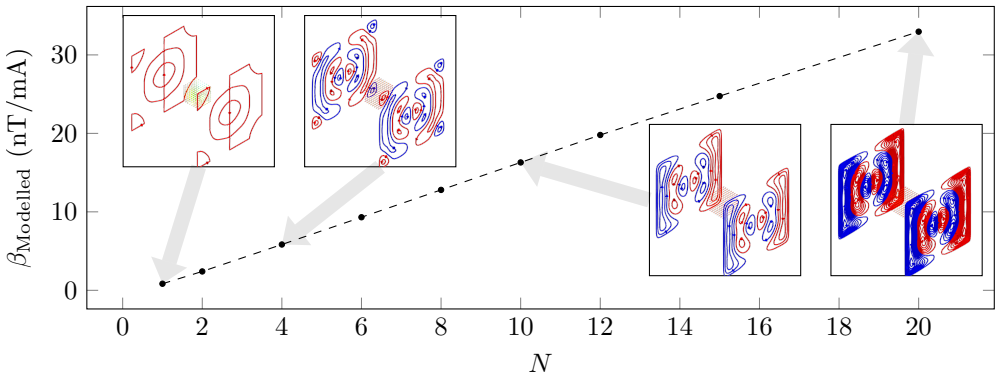

Figure 5.14: Bfieldtools generated current loops for coils of external dimensions, 20×20 mm^2, across a sensing region of $8 \times 8 \times 8$ mm^3. Each coil pair is separated by distance $S = 20$ mm, red and blue indicate opposing current directions. The coils were generated with a varying number of contours, N and the corresponding field-to-current ratio, β_{Modelled}, modelled. Insets show the current contours and vector field experienced across the sensing area for $N = 2, 4, 10$ and 20.

producing PCBs, these high complexity designs require smaller tracks to accommodate the increase of contours, which is ultimately restricted by minimum track width and minimum track separation capabilities of the PCB manufacturer. As such, the geometry and manufacturer of the PCBs heavily dictates the manufacturability, in this case $N = 10$ is the maximum complexity achievable for the small size of the PCBs (20×20 mm^2) based on the feasibility of track width.

Table 5.1: Bi-planar coil field to current ratios. Axis; Direction of B-field. Version; PCB coil version. Expected; modelled field-to-current ratio (nT/mA) from bfield-tools. Measured; experimentally measured field-to-current ratio (nT/mA) using the well-calibrated SERF OPM. Homogeneity (%); Average deviation across the sensing region with respect to the expected field-to-current ratio, from numerical simulation.

Axis	Version	Expected (nT/mA)	Measured (nT/mA)	Homogeneity (%)
x	V1	9	9.0	$\simeq$93
y	V1	12	11.9	$\simeq$88
z	V1	9	9.0	$\simeq$93
x	V2	27	27.1	$\simeq$97
y	V2	36	36.0	$\simeq$94
x	V2	27	27.0	$\simeq$97

Based on the complexity investigation carried out in Figure 5.14, version 2 of

the bi-planar PCB coils, referred to as V2, is based on $N = 10$ for the x and z-axes, and $N = 3$ for the Helmholtz coil on the y-axes. The full design of the contours, homogeneity and PCB designs can be seen in Figure 5.15. The V2 coils were validated in the same method as the V1 coils, through direct measurement. As summarised in Table 5.1 the V2 coils have a proven 3 times increase in field-to-current ratio, and an overall improvement in homogeneity across the sensing region.

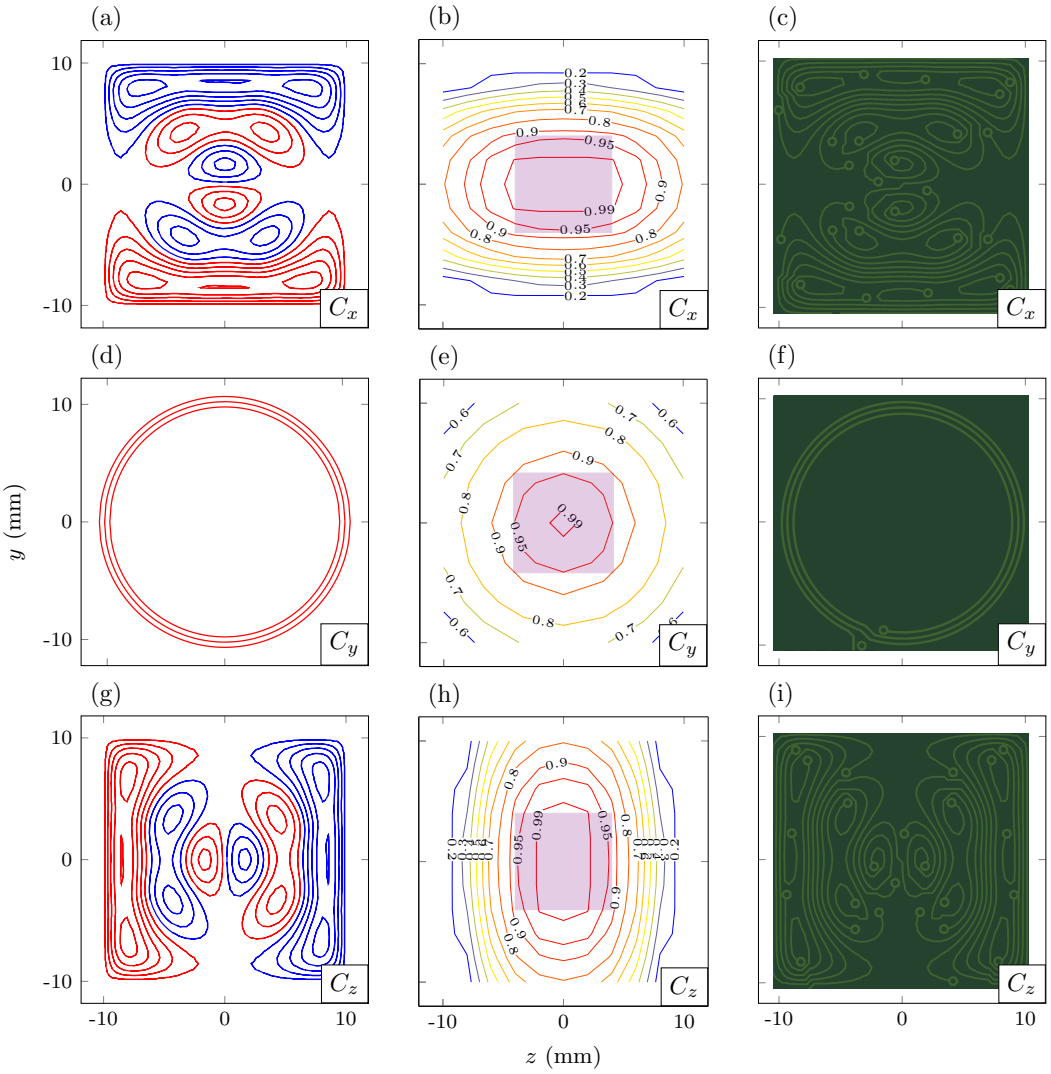

Figure 5.15: Version 2: 3-axis bi-planar coils assembled across the yz-plane of the portable sensor. Each axis (x,y and z) has a respective unique coil design C_x, C_y and C_z, indicated in each subplot. **a,d,g**) bfieldtools current contours ($N = 10$) produced for the specified desired field, red and blue indicate opposing current directions. **b,e,h**) modelled magnetic field homogeneity, based on the bfieldtools current contours, calculated across the full region between coil pairs, with sensing regions highlighted in purple. **c,f,i**) Photograph of manufactured PCB designed based on bfieldtools current loops shown in a,d,g.

Table 5.2: Definition of all optimised operational parameters (p), with corresponding units. Optimised Value (p), the optimised value for each parameter, found using the methods described in Chapter 4.

Parameter	**Optimised Value (p)**	**Unit**
Temperature (T)	115	°C
Laser power (LP)	5.6	mW
Laser detuning (LD)	6.7	GHz
Modulation amplitude (B_{Mod})	226	nT
Modulation frequency (ω_{Mod})	365	Hz

5.6 Sensor operation

Up to now, this chapter has described a portable version of the sensor hardware from Chapter 3. The system control and signal extraction is the same as described there, in Section 3.3. The zero field magnetometer utilises the Hanle effect to detect changes in the magnetic field through an absorption measurement, as discussed in Chapter 2. The Hanle effect is used to detect and cancel the residual magnetic fields in three axes through application of the magnetic field values required to cancel any static residual fields (B_{x0}, B_{y_0}, and B_{z0}). In the same method as discussed in Chapter 3, magnetic modulation across the sensitive axis, and a lock-in detection scheme allows for measurement of the atomic response as a time domain series, from which frequency domain information can also be extracted. Some biomagnetic signals are observed in the frequency domain (MEG) and others in the time domain (MCG), both of which will be measured in the following sections.

All operational parameters, summarised in Table 5.2, for the prototype sensor were optimised for sensitivity performance using the methods described in Chapter 4. Operation at these parameters results in an estimated magnetic resonance linewidth where Γ= 170 nT.

The bandwidth of the sensor is characterised, as shown in Figure 5.16, through recovery of the amplitude of an applied sine wave across the sensitive axis, at 1 nT scale, for a logarithmic range of frequencies between 1 Hz and 40 kHz. The operational parameters in Table 5.2 were used, however the modulation frequency was

increased to $\simeq$ 1100 Hz, without any change to the measured linewidth or significant loss in sensitivity, as we expected this frequency to be outside the expected bandwidth. A 2nd order low-pass filter response was fit to the measured data, with a 3db point of $\simeq$ 1600 Hz. The region of linear response with respect to frequency of the sensor occurs up to $\simeq$ 900 Hz. The photodiode has a 16 kHz hardware low-pass filter, which manifests as a higher order response at $>$ 16 kHz as seen in Figure 5.16.

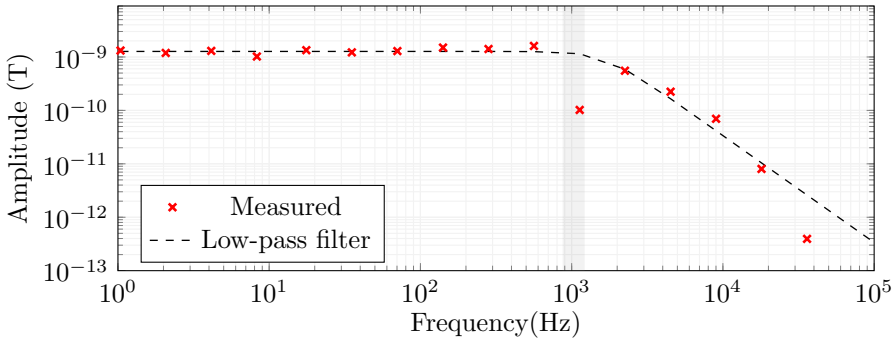

Figure 5.16: Measured bandwidth, characterised through recovery of the amplitude of an applied sine wave, applied at 1 nT magnitude, at various frequencies. The applied modulation frequency $\pm$10 % is indicated by the gray shaded area, recovered test signal data within this region has greater uncertainty due to proximity to the modulation frequency. A 2nd order low-pass filter was fit to the measured data, with a 3 db point at $\simeq$ 1600 Hz.

5.7 Bio-magnetism measurements

This section will discuss practical implementation of the described portable sensor, to test the suitability of the device for measuring real biomagnetic signals. The University of Nottingham provided access to their MSR facilities at the Sir Peter Mansfield Centre, allowing for biomagnetic measurements of multiple participants for MCG and MEG. The experimental paradigms and results of these biomagnetic measurements are discussed in the following sections. Use of the portable sensor in this setting, outside of a controlled laboratory environment, highlighted a number of ways to improve both the sensor design, mounting and control, which will be discussed in more detail at the end of this section.

5.7.1 Magnetocardiography

To demonstrate the practical nature of the prototype sensor, a biomagnetic measurement was made in which the magnetic signal of the human heart was measured. MCG has gained research interest due to functional and clinical benefits pertaining to cardiac source location accuracy in comparison to electrocardiography [149, 150]. MCG measurements with SERF OPMs have been widely used as a viable demonstration of OPM portability, sensitivity and suitability for biomagnetic measurements for both single [151] and multichannel systems [126, 127, 152, 153].

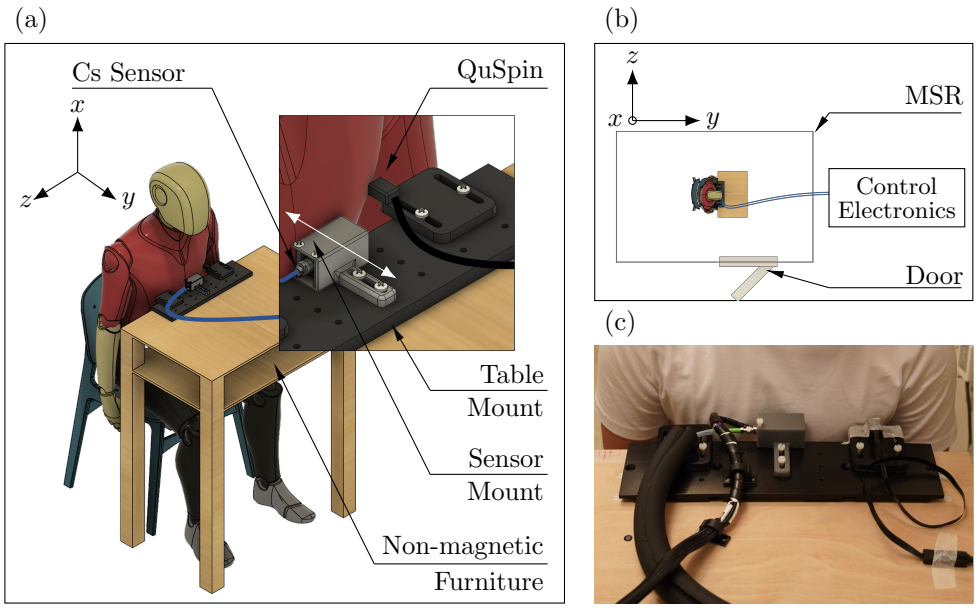

Figure 5.17: Magnetocardiogram setup for the prototype caesium portable sensor. **a**) The participant is seated on non-magnetic furniture with their chest close to the prototype sensor. A commercial sensor (QuSpin QZFM Gen-2) is mounted 10 cm from the prototype sensor. Inset shows both sensor locations, the sensitive axis of the prototype sensor indicated with a white arrow and the 3D printed table/ sensor mounts. **b**) Participant with respect to MSR and sensor control electronics (housed external to MSR). **c**) Photograph of participant leaning against the stationary sensors with the prototype sensor central with respect to their chest.

Figure 5.17 shows the MCG setup for the caesium portable sensor. A magnetocardiogram measurement from a human subject was taken. Four participants (named Participant 0 to 3) took part in the study. The participants gave written, informed consent, and the study was approved by the University of Nottingham

Medical School Research Ethics Committee. The MCG measurement took place inside a MSR (Vacuumschmelze Ak3b with two layers of MuMetal and one layer of copper).

The experimental setup of the measurement of the MCG measurement is as follows; the participant to be measured sits within the MSR on non-magnetic furniture. The prototype caesium sensor is mounted to the non-magnetic furniture with 3D printed table and sensor mounts, seen in Figure 5.17(a) inset. A commercial sensor (QuSpin QZFM Gen-2) is mounted 10 cm from the prototype sensor, to facilitate concurrent measurement for signal verification. The QuSpin has a sensitivity of < 15 fT/$\sqrt{\text{Hz}}$ in the band between 3-100 Hz. The participant placed their chest close to the stationary sensors to align with their approximate heart location, Figure 5.17(c).

The portable sensor cabling, which comprises of control signals, detection and optical fibre, were routed through a small hatch in the MSR. All control electronics are housed outside of the MSR, Figure 5.17(b), including the laser driver, coil driver, transimpedance amplifier, heater driver, and data acquisition unit. Physically shielding the sensor from the driving electronics signals reduces the noise contributions and improves the sensitivity of the sensor.

The prototype caesium portable sensor has been successfully used for MCG for all participants. The MCG measured response, after the application of a 30 Hz low-pass filter, for Participant 0 using the portable caesium prototype sensor and QuSpin QZFM Gen-2 sensor over a 60 s time period is shown in Figure 5.18. A low frequency oscillation ($\simeq$ 0.1 Hz) due to breathing is expected [154, 155] and visible in the responses of both sensors. The deviation in alignment of the breathing oscillation in the two responses is likely due to the movement of the chest varying with respect to the offset of the placement of the sensors.

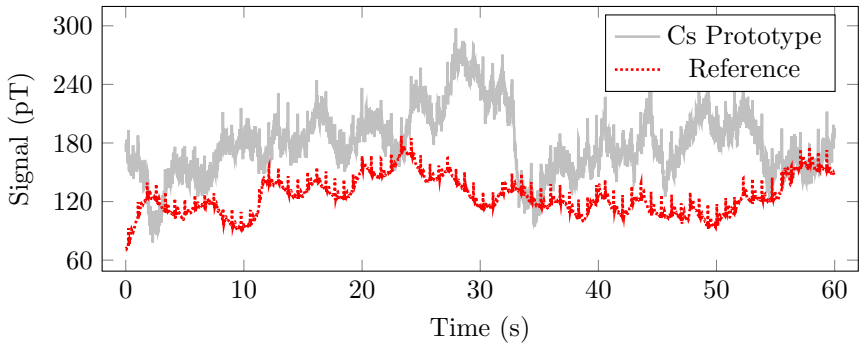

Figure 5.18: Magnetocardiogram measured of Participant 0 using the portable caesium prototype sensor and QuSpin QZFM Gen-2 sensor inside a MSR over a 60 s time period. Low frequency oscillation ($\simeq 0.1$ Hz) due to breathing is visible in the responses of both sensors.

The cardiac signal is resolvable in both sensors responses, without any averaging, as shown in Figure 5.19(a). The SNR of the caesium prototype sensor signal is improved by averaging over multiple heartbeats, shown in Figure 5.19(b), after triggering the signal with respect to the QuSpin peak. To understand the effect of averaging, we must quantify the SNRs for both sensors.

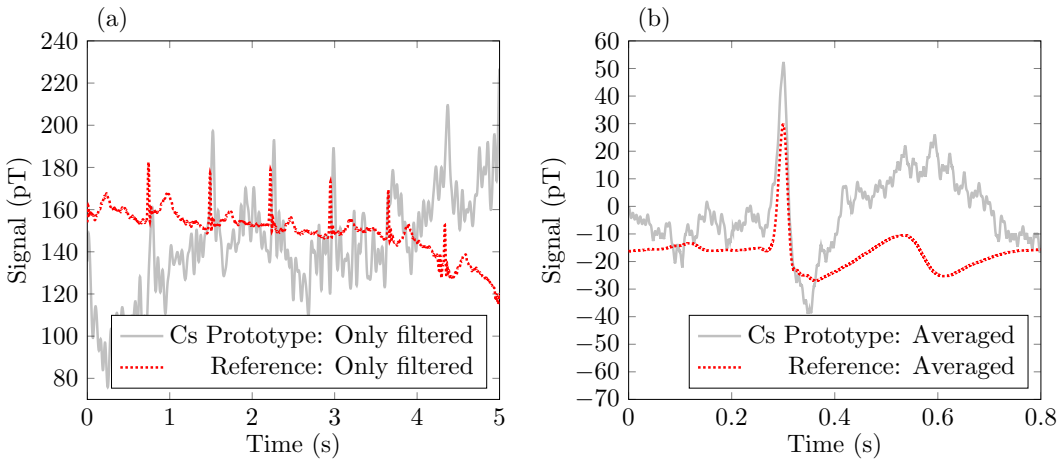

Figure 5.19: Magnetocardiogram measured using the portable caesium prototype sensor and QuSpin QZFM Gen-2 sensor inside a MSR, using a band-pass filter from 1-40 Hz. **a**) Real-time responses of both sensors, without averaging. **b**) Both responses averaged across 60 heartbeats.

An approximation of the SNR can be extracted from the measured response [156], through estimation of the peak-to-peak amplitude of the R peak to the S peak, $A_{\mathrm{R-S}}$,

in the QRS complex [157], as illustrated in Figure 5.20(a), such that;

$$\mathrm{SNR} = \frac{\mathrm{A_{R-S}}}{\sigma_{\mathrm{Noise}}} \ , \tag{5.1}$$

where σ_{Noise} denotes the standard deviation of the noise.

Figure 5.20 shows a single cardiac trace extracted from the MCG measurement taken of Participant 0, after the application of a more narrow 1-25 Hz band-pass filter, to aid identification of lineshape features. The QuSpin QZFM Gen-2 sensor measurement for a single cardiac trace averaged across 10 heartbeats is shown in Figure 5.20(a), where the P-QRS-T features [158] of the cardiac signal are also indicated. From Figure 5.20(a), an approximation of the SNR for the QuSpin sensor $\mathrm{SNR_{QuSpin}}$, can be extracted, where $A_{\mathrm{R-S}} \simeq 40$ pT and $\sigma_{\mathrm{Noise}} \simeq 2$ pT, such that $\mathrm{SNR_{QuSpin}} \simeq 20$. The caesium portable sensor measurement for a single cardiac trace with various amounts of averaging are shown in Figure 5.20(b). Averaging of the caesium portable sensor MCG signal was achieved by synchronising the R peak of the QuSpin waveform, using sequentially recorded heartbeats from the MCG data. From Figure 5.20(b), using the trace without averaging, an approximation of the SNR for the caesium sensor $\mathrm{SNR_{Cs}}$, can be extracted, where $A_{\mathrm{R-S}} \simeq 90$ pT and $\sigma_{\mathrm{Noise}} \simeq 10$ pT, such that $\mathrm{SNR_{Cs}} \simeq 9$. It is likely that the laser and the fibre coupling the light to the sensor head contribute a large amount of uncorrelated noise to the measurement over the measurement window for the caesium portable sensor.

The SNR of the caesium prototype sensor, $\mathrm{SNR_{Cs}}$, improves with averaging such that $\mathrm{SNR_{Cs}} \simeq 30$ for the average of 60 heartbeats, as shown Figure 5.20(b). The SNR improvement is largely due to the noise, σ_{Noise}, decreasing with the higher-number of averages. However, the peak-to-peak amplitude of the R peak to the S peak, $A_{\mathrm{R-S}}$, is also attenuated through the use of more averages. Figure 5.20(b) demonstrates that the R and S peaks are resolvable from the caesium prototype sensor response without any averaging. Furthermore, the P-QRS and T peaks are visible and resolvable from the caesium prototype sensor response with the use of any averaging, including for only 10 heartbeats.

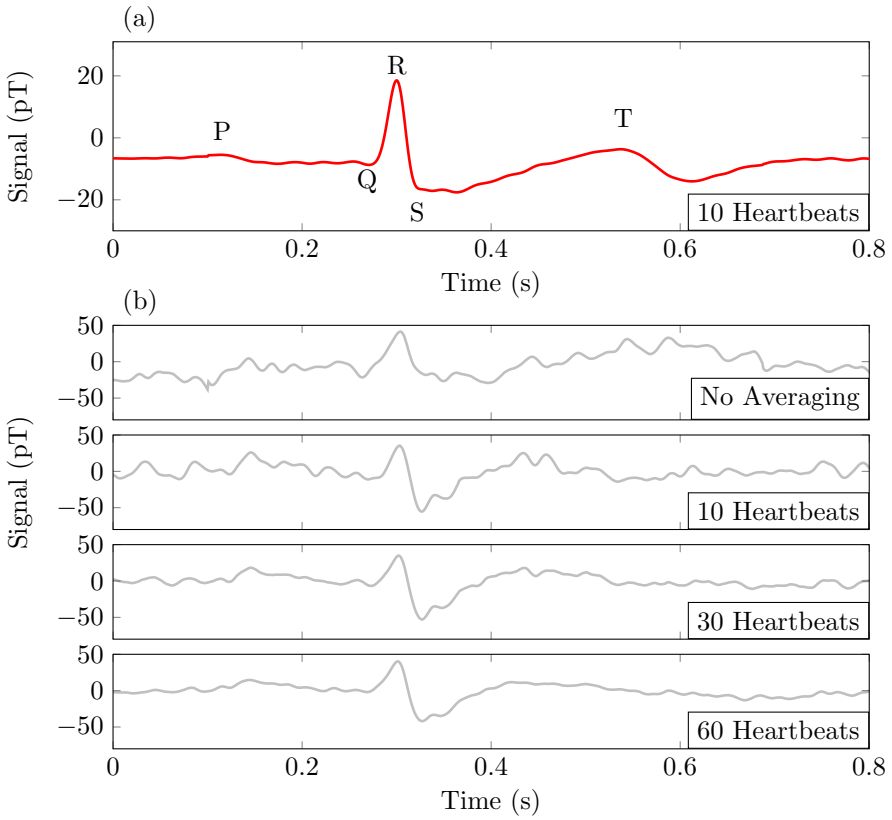

Figure 5.20: Magnetocardiogram measured using the portable caesium prototype sensor (indicated in grey) and QuSpin QZFM Gen-2 sensor (indicated in red) inside a MSR, for a single participants (Participant 0). All responses are filtered, using a band-pass filter from 1-25 Hz. **a**) QuSpin response without averaging. **b**) Portable sensor response, averaged across a range of number of heartbeats: 0 (No Averaging), 10, 30 and 60.

The MCG measurements taken for the remaining participants (1,2 and 3) show good alignment between the recordings taken using the portable caesium prototype sensor and QuSpin QZFM Gen-2 sensor, illustrated in Figure 5.21. The recorded signals for Participant 1, Figure 5.21(a), shows an apparent delay between the R and S peaks in the cardiac traces found from the separate sensors. This deviation in cardiac line shape is presumably caused by the positioning of the sensors relative to the dipole field of the heart [126, 159]. The measurements of Participant 2, Figure 5.21(b), shows good alignment between the two sensor recordings, however

there is a decrease in SNR comparative to Participant 0, likely due to the standoff distance between the participants chest and the sensor. In future measurements, a mechanism or mount to ensure a constant stand-off distance between the sensor and signal is advisable, particularly to ensure consistency between participants. Finally, the recorded MCG for Participant 3 Figure 5.21(c) is a much lower amplitude than the other participants for both sensors, which is again likely due to both placement and stand-off distance of the sensors to the signal.

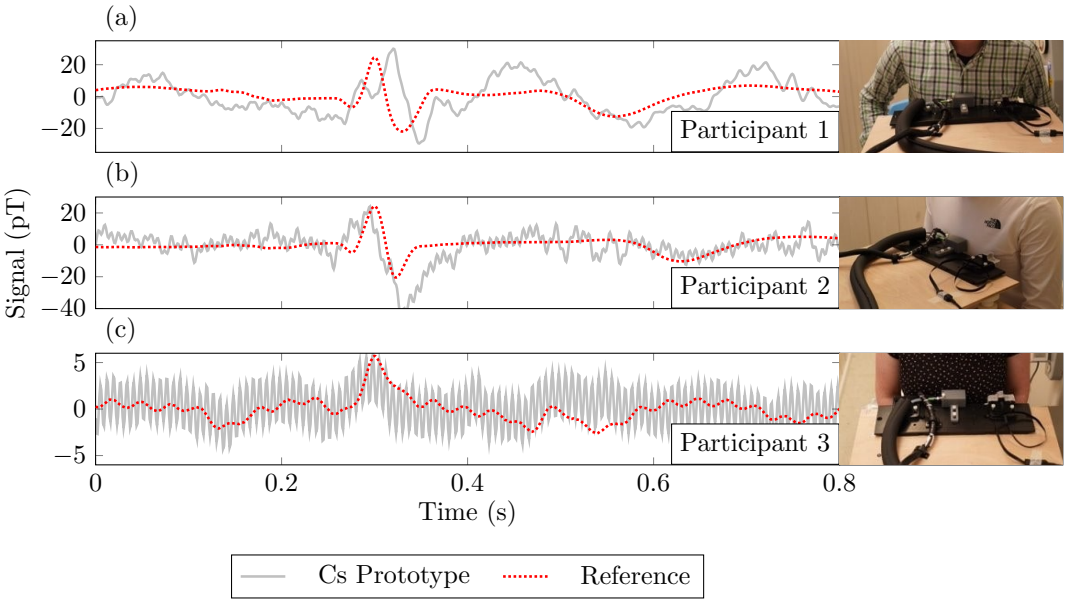

Figure 5.21: Magnetocardiogram measured using the portable caesium prototype sensor (indicated in grey) and QuSpin QZFM Gen-2 sensor (indicated in red), inside a MSR, for a multiple participants (1,2 and 3). All responses are averaged across 20 heartbeats, using a band-pass filter from 1-40 Hz. **a**,**b**,**c**) Illustrate the measured MCG and photograph of the measurement, for participants 1, 2 and 3 respectively.

5.7.2 First trials of magnetoencephalography

To further demonstrate the practical nature of the prototype sensor, a biomagnetic measurement was made in which the magnetic signal of the human brain was measured. Neural signals caused by electric currents flowing in neurons in the brain occur with an estimated peak-to-peak amplitude of $\simeq 120$ mV in pulses within the human brain [9]. The oscillation frequency, typically ranging from 0.2 to 100 Hz, is

linked to different neural functions [160]. Alpha-band oscillations, 8–13 Hz [3], were chosen for this measurement due to these signals being among the largest amplitude recorded from the brain.

MEG has gained research interest due to functional and clinical benefits pertaining to neural source location accuracy [87, 161] in comparison to EEG. Direct detection of neural signals through EEG has shown poor spatial resolution due to participant's movements and signal distortion as electrical fields pass through inhomogeneous biological media of the brain tissue and skull [9]. MEG techniques measure the corresponding biomagnetic fields of post-synaptic volume currents where these magnetic fields are not subject to deformation by biological media surrounding the brain. As such, spatial resolution for MEG is typically better than EEG [18] whilst maintaining high (ms) temporal resolution [9, 21]. MEG measurements with SERF OPMs have been widely used as a viable demonstration of OPM portability, sensitivity and suitability for biomagnetic measurements for both single [51] and multichannel systems [124, 125, 162–166]

Figure 5.22 shows the MEG setup for the caesium portable sensor. A magnetoencephalogram alpha-band measurement from a human subject was taken. A single participant (Participant 4) took part in the study. The participant gave written, informed consent, and the study was approved by the University of Nottingham Medical School Research Ethics Committee. The MEG measurement took place inside the same MSR as the MCG measurement.

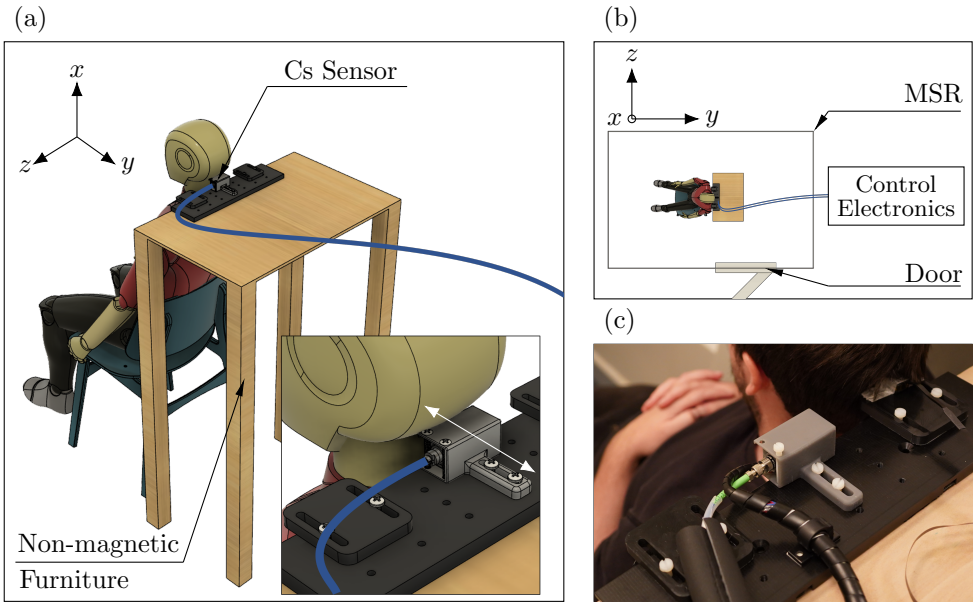

Figure 5.22: Magnetocardiogram setup for the prototype caesium portable sensor. **a**) The participant is seated on non-magnetic furniture with the base of their head close to the prototype sensor. The commercial SERF sensor (QuSpin QZFM Gen-2) or the prototype sensor are used in this position sequentially. Inset show the portable sensor location with respect to the participants head, the sensitive axis of the prototype sensor indicated with a white arrow and the 3D printed table/ sensor mounts. **b**) Participant with respect to MSR and sensor control electronics (housed external to MSR). **c**) Photograph of Participant 4 leaning against the stationary commercial sensor, central with respect to the base of their head.

The experimental paradigm of the MEG measurement is as follows; the participant to be measured sits within the MSR on non-magnetic furniture. The prototype caesium sensor is mounted to the same non-magnetic furniture and 3D printed table and sensor mounts as the MCG measurement, seen in Figure 5.22(a) inset. The location of the sensor with respect to the head is of high importance for MEG measurements, and needs to accurate to mm-level [18]. The commercial sensor (QuSpin QZFM Gen-2) cannot be mounted closer than 10 cm to the prototype sensor, due to sensor cross-talk, which rules out the possibility of concurrent measurement for signal verification. The measurements were taken sequentially, first for the QuSpin sensor, followed by the caesium portable sensor. The participant placed the base of their head close to the stationary sensors to align with their approximate alpha-

band signal location, Figure 5.22(c). The participants neural activity is measured for 180 s with their eyes open, followed by 180 s with their eyes closed, to stimulated alpha-band neural oscillations [167].

As with the MCG measurement, all control electronics are housed outside of the MSR, Figure 5.22(b); physically shielding the sensor from the driving electronics signals reduces the noise contributions and improves the sensitivity of the sensor.

The MEG measured response, after the application of a 2-25 Hz band-pass filter, for Participant 5 measured over 180 s with eyes open and 180 s with eyes closed is shown in Figure 5.23, where the alpha frequency-band of interest (8–13 Hz) is highlighted in grey. The PSD is utilised to provide frequency information, using the methods described in Chapter 3, where 18 s of data is averaged 10 times for each state (eyes open or closed). The response using the portable caesium prototype sensor, is shown in Figure 5.23(a) and the QuSpin QZFM Gen-2 sensor, Figure 5.23(b). In this format, we expect a typical alpha-band response to manifest as an increase in signal amplitude, when the eyes are closed, at several points across the alpha-band frequency range [85, 168, 169]. It appears the two sensors have measured similar frequency trends with eyes closed versus eyes open across the alpha frequency-band, with a clear spike at $\simeq 8$ Hz for both sensors when the participant had their eyes closed. However, without repetition of this measurement or simultaneous recording, it cannot be definitively stated whether an alpha-band MEG signal is measured with either sensor. Both sensors show the same noise spikes at $\simeq 4$ Hz and $\simeq 7$ Hz, that appear to be location specific to the Nottingham MSR.

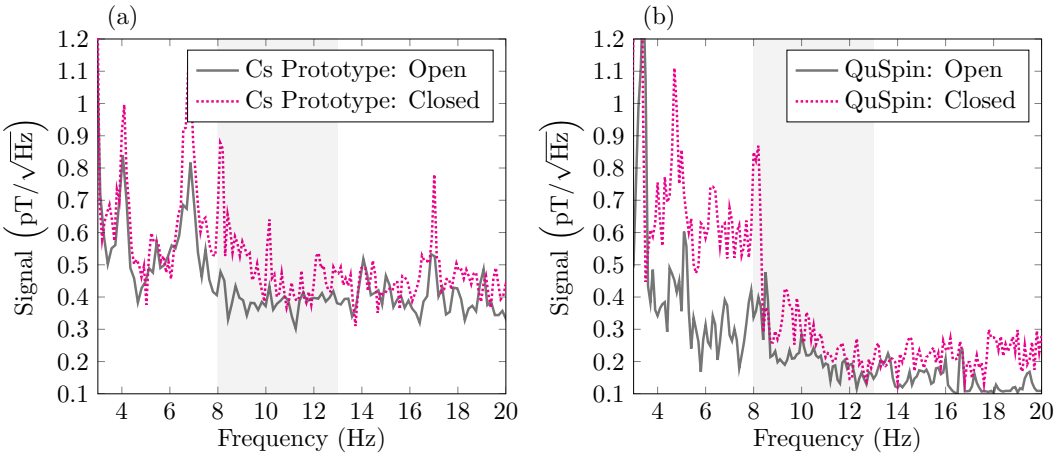

Figure 5.23: Magnetoencephalogram illustrated through an average $\sqrt{\mathrm{PSD}}$ produced by averaging 18 s of data 10 times. Alpha-band frequency (8–13 Hz), highlighted by shaded gray area. The participant kept their eyes open for 180 s, followed by 180 s when their eyes were closed. The Cs portable sensor MEG is illustrated in **a**), and the QuSpin QZFM Gen-2 sensor is illustrated in **b**).

The noise floor and sensitivity of the caesium portable sensor, at the point of development during the biomagnetic measurements, also acted as a inhibiting factor to this measurement. The noise floor, measured in a quiet magnetically shielded environment while no external signals are introduced, over 1 s intervals, allows the inherent noise of the sensor to be assessed. The geometric mean over the defined frequency-band of interest (5-20 Hz) produces a sensitivity figure of merit, as discussed in Chapter 2. Figure 5.24 shows the noise floor and sensitivity estimates for the caesium sensor in two states, 1) pre-optimised and 2) optimised. The pre-optimised sensor, with an estimated 440 $\mathrm{fT}/\sqrt{\mathrm{Hz}}$ sensitivity, was taken at the point of development in which the MEG measurements were taken. The sensitivity limit can be seen in Figure 5.23(a), manifesting as an elevated base level of noise in contrast to the commercial sensor in Figure 5.23(b).

The optimised sensor sensitivity of 90 $\mathrm{fT}/\sqrt{\mathrm{Hz}}$, Figure 5.24, was found through optimisation activities, using the methods described in Chapter 4. With this improved sensitivity, we would expect to be able to distinguish features in a similar alpha-band MEG measurement to much greater clarity.

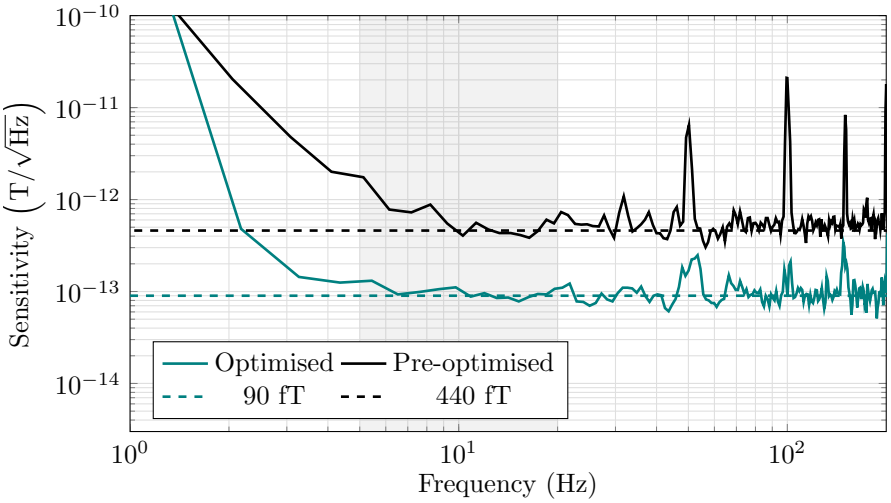

Figure 5.24: Measured magnetic noise floor of the sensor, dashed line indicates geometric mean calculated in the frequency-band of interest (5-20 Hz). This measurement was taken in a 5-layer mu-metal shield (Magnetic Shields Limited).

5.7.3 Practical biomagnetic measurements: Lessons learned

Use of the portable sensor in the MSR facilities at the Sir Peter Mansfield Centre, outside of a controlled laboratory environment, highlighted the following points:

- **Temperature stabilisation**

  The opening and closing of the MSR door between measurements caused influential temperature drifts, ≤ 5 °C, of the cell temperature. This is an issue that I had not encountered in the laboratory environment as the sensor is typically shielded from any air currents when inside the magnetic shields. As such, the temperature drifts highlighted the need for quicker temperature stabilisation methods, inspiring the research discussed in Section 3.2.4.

- **Zero-field identification and correction**

  The prototype sensor taken to Nottingham still utilised the exhaustive 2D mechanism for identifying the zero-field points across the x-axis and z-axis, which took around $\simeq 2$ minutes. During practical measurement, the shield doors opened and the participant changed regularly, which required frequent

identification of zero-field that ultimately accumulated into a lot of measurement time across the day. As such, I developed the quick zero-field identification method on return to the laboratory, as discussed in Section 3.3.1, reducing the total time required to identify zero-field to 8 s.

- **Alignment of the sensitive axis**

  The orientation of the sensor with respect to both the cardiac and neural measurements was not consistent between measurements or participants. This is highlighted in the variance of MCG line-shapes seen in Figure 5.21 between participants. This demonstrates the need for the development of signal specific mounts to be produced that ensure a consistent stand-off and alignment to the signal source for future measurements, as seen for MEG helmets [125] or MCG chest mounts [126].

- **Other hardware and software improvements**

  A number of smaller further hardware improvements were also highlighted, such as the cabling used on the prototype introducing pickup of noise during measurement, leading to the use of different shielded cable for the next prototype. Software improvements were also highlighted, such as the need for live data monitoring for sensor to assist alignment of the sensor.

5.8 Portable sensor: Discussion

I have presented the design of a prototype single-beam caesium portable sensor and proved its suitability for use in biomagnetic measurements through a demonstrated MCG measurement. Key miniature and microfabricated elements of a prototype portable sensor were presented and shown to have been successfully implemented.

The heating, temperature control and insulation methods can maintain the required cell temperature for prolonged timescales (> 90 minutes) while the package outer remains at skin safe temperatures (< 37 °C). This supports both the use of these heating and insulation methods, and also the use of caesium in this application due to lower heating requirements compared to other alkalis and subsequent lower

external temperature.

Miniaturized bi-planar coils are implemented to provide 3-axis fields with a very small footprint within the sensor, with a high degree of field homogeneity across the sensing area. Future improvements to the coil design will increase the field to current ratio of the coils, to allow for greater field control.

While the prototype portable sensor is larger than similar commercial sensors, there is scope for further miniaturisation using many of the design techniques implemented here. Bi-planar PCB coils can be made for any future custom geometry in the same method as presented above. All 3D printed components (such as high temperature optical inserts) are designed and manufactured fully in-house. A professional product designer would be able to make reductions of $\geq$ 10 % on each dimension through improvements such as reduced wall thicknesses, optimised positioning of components and compact waveplate mount design. However, we note that the development of MEMS cell production in-house is still progressing. Ultimately, the target is a footprint of 20 mm^2,

The caesium single beam prototype sensor has a peak sensitivity of 90 $fT/\sqrt{Hz}$. Limitations to sensitivity are predominantly due to laser noise. As such, future improvements include the reduction of common mode noise using differential measurement [51, 170], for which the sensor package has been designed. Transition to an on-package laser source such as a vertical-cavity surface-emitting laser (VCSEL) would also aid optical noise, especially noise introduced due to the optical fibre.

The single beam prototype sensor has a measured bandwidth of $\simeq$ 1600 Hz with a linear response up to $\simeq$ 900 Hz, illustrated in Figure 5.16. This marks a considerable improvement on the reported bandwidth of commercial rubidium sensors, with a linear frequency response up to $\simeq$ 130 Hz [87, 140].

The prototype portable single-beam caesium SERF sensor described here is a step towards the development of a sensor with suitable sensitivity and bandwidth for a range of biomagnetic measurements if further development with regards to noise characterisation and miniaturisation are realised. This sensor serves as a test-bed for novel and improved components.

Chapter 6

Summary and conclusions

6.1 Summary of work

This thesis presents a single-beam SERF magnetometer using caesium as the sensing alkali within a microfabricated atomic vapour cell. SERF magnetometry was a novel endeavor for the Experimental Quantum Optics and Photonics group at the University of Strathclyde. Hence, all aspects of the project, including its development, have been built entirely from scratch over the course of the past four years. The main aims for this work, 1) operating at a lower temperature and 2) obtaining a higher bandwidth sensor, were both motivated by the stipulations for human biomagnetic measurements, particularly magnetoencephalography. The work in this thesis demonstrates how I have achieved both of these aims.

The designed and constructed prototype single-beam Cs sensor is suitable for use in biomagnetic measurements as proven through a demonstrated MCG measurement. Miniature and microfabricated elements of the sensor have been successfully employed to created a sensor package with portable scale external dimensions of $25 \times 25 \times 50$ mm^3, reaching the goal of a portable package with a footprint of $\simeq$ 625 mm^3, less than a square inch. Miniaturised bi-planar coils provide 3-axis static magnetic field control and an additional oscillating magnetic field across the $y-$axis, with a very small footprint within the sensor and a high degree of field homogeneity across the sensing area. An improved design of the coils has also

been proposed that provides more field for less current, with view of decreasing the amount of current noise experienced by the sensing atoms. High efficiency (> 90 %) AC heating of a MEMS vapour cell has also been successfully achieved with automatic and stable temperature control. Combination of the efficient cell heating and the insulation methods maintain the required cell temperature for prolonged timescales (> 1 hour) whilst maintaining a skin-safe (< 41 °C) external face of the sensor.

The optimised sensitivity of the sensor was achieved through careful selection and intelligent optimisation of constituent components and operational parameters. A number of automated machine learning methods were designed and implemented that significantly improved the sensitivity of the SERF magnetometer, from $\simeq 500$ fT/$\sqrt{\text{Hz}}$ to 109 fT/$\sqrt{\text{Hz}}$ across a frequency band of 5 to 20 Hz. The machine learning techniques were thus proven as suitable for application within a magnetometry experiment with multi-parameters related by complex dynamics. Through development of the machine learning toolkit, the digitally selectable parameters were successfully optimised including cell temperature, laser power and frequency, and the modulation depth and frequency. Furthermore, the machine learning toolkit allowed for optimisation of physical experimental changes provided by the quick benchmarking of the optimised sensitivity after implementing the hardware change. This hardware optimisation is demonstrated through the testing of multiple atomic vapour cells with varying buffer gas pressures to quantify the effect of nitrogen buffer gas pressure on the measured optimised sensitivity. Here I proved that increasing nitrogen buffer gas pressure linearly increased sensitivity capabilities such that an approximate 3 fT/$\sqrt{\text{Hz}}$ sensitivity gain is provided for every 1 Torr of buffer gas added to the atomic vapour cell in the range tested. A focus of work in the immediate future will be to investigate the extent of this performance increase. The machine learning optimisation of atomic vapour cell buffer gas pressure lead to the selection of an atomic vapour cell with 225 Torr of nitrogen buffer gas that produced an optimised sensitivity of 90 fT/$\sqrt{\text{Hz}}$ in the frequency band of 5 to 20 Hz.

A primary motivator for the work in this thesis was to prove the effectiveness

of caesium as the sensing alkali in a SERF magnetometer for detecting biomagnetic signals. The significant advantage of the use of caesium over other typically used alkali's, such as rubidium, is the reduced cell temperature required to reach the desired atomic density in an atomic vapour cell of the equivalent volume. The external surface of the portable sensor never exceeds 37 °C, eliminating the requirement for a stand-off distance between the sensor and the participants skin during biomagnetic measurements. Stand-off distances are regularly employed for rubidium based SERF sensors due to high external package temperatures (far exceeding skin-safe guidance). The stand-off distance, reported at $\simeq 5$ mm for a commercial rubidium based sensor [171], reduces the measured magnetic field as an inverse function of the distance cubed. For the caesium based SERF magnetometer the reduction in stand-off distance may compensate for the slightly reduced sensitivity capabilities.

The use of caesium as the sensing alkali has additionally led to increased bandwidth capabilities. The demonstrated bandwidth of $\simeq 1600$ Hz, accompanied by a linear response up to $\simeq 900$ Hz, signifies a notable advancement compared to commercially available rubidium sensors. This increase in bandwidth provides the opportunity for the sensor to be used in measurement schemes where the frequency of the biomagnetic signal is expected to be far above 100 Hz.

Overall, the prototype portable single-beam caesium SERF sensor demonstrated in this thesis is a step towards developing a sensor with suitable sensitivity and bandwidth for a range of biomagnetic measurements. Through careful component selection and intelligent design, the external dimensions of the prototype sensor could be reduced by ≥ 10 % in each dimension. Additionally, further development of the portable caesium SERF magnetometer could be pursued to improve its sensitivity through further optimisation of hardware (such as through use of an atomic vapour cell with nitrogen buffer pressure > 225 Torr) and reduction of optical and technical noise sources. Ultimately, this research lays the groundwork for the development of non-invasive diagnostic tools for biomagnetic medical imaging and monitoring techniques with the use of caesium atoms.

6.2 Future work

Future work for this research will involve expanding the types of biomagnetic signals detected beyond cardiac signals. With the proven sensitivity of the caesium SERF magnetometer, it should be possible to measure a range of biomagnetic signals such as neural activity through MEG, and muscle measurements in through magnetomyography. Figure 6.1 illustrates a proposed setup for a magnetomyography measurement using the portable caesium SERF sensor in the current prototype package, and using the shielding and equipment described throughout this thesis. A measurement in this scheme would require participant involvement specifically through the tensing of the participants fist in regular intervals. The measured biomagnetic signal will manifest as heightened activity across a wide range of frequency bands during the periods of tension due to multiple oscillating biomagnetic signals being triggered by the clenching of a fist.

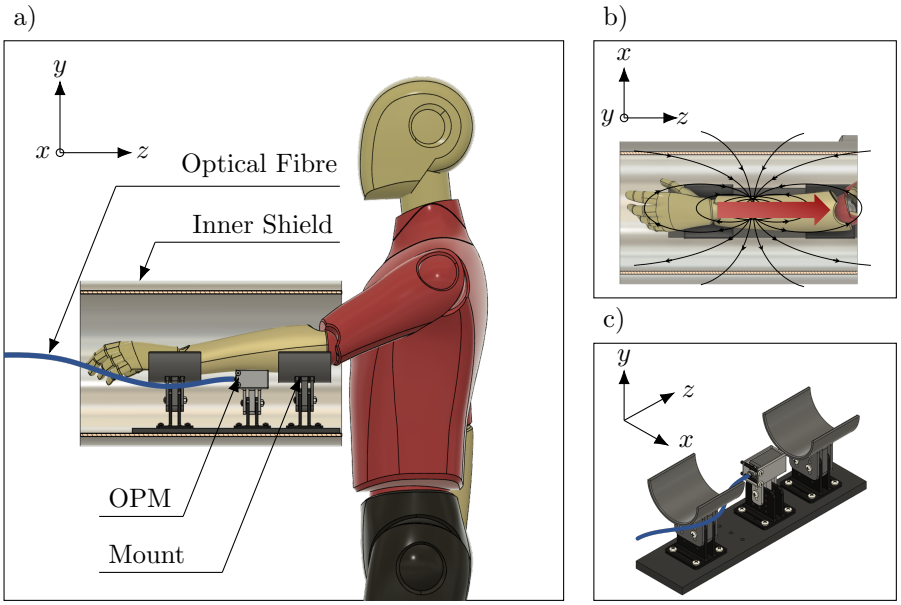

Figure 6.1: A proposed setup for a magnetomyography measurement of the forearm of a participant, using the portable sensor in the current prototype package. The sensor is housed and mounted inside a 5 layer shield in the laboratory environment. **a**) The participant is stood at the opening of the shield, with their arm close to the prototype sensor. **b**) The expected magnetic signal and field lines with respect to the participants arm. **c**) Model of the 3D printed mounts and arms rests that will ensure alignment of the arm and sensor through the measurement

Future work will also involve repeating biomagnetic measurements that were presented in this thesis. I plan to repeat the magnetoencephalography trials at the magnetically shielded room at the Sir Peter Mansfield Centre, in collaboration with the University of Nottingham. With the proven sensitivity improvements of the sensor since the last trials, and the planned improvements in the mounting and measurement schemes, we are hopeful that alpha-band measurements will be achievable within these trials.

There are other aspects of the sensor design and operation that warrant further exploration. A systematic cross axis projection error arises during measurement along the sensitive axis of the sensor, caused by the presence of multi-axis static magnetic fields, [43] which can be minimised through active control of the static magnetic fields across all axes. I plan to investigate an operational scheme aimed at minimising cross axis projection error through magnetic modulation of each axis at a unique frequency.

Finally, we plan to utilise the techniques and systems designed for the sensor produced in this research to explore other magnetometer schemes, particularly gradiometric configurations.

Appendix A

Operational parameter calibration setting

Laser driver calibration

The laser driver controller requires commands in terms of laser current and TEC temperature, calibration allows for conversion. The desired laser power P_L is converted to laser current I_L through the following conversion;

$$I_L = 0.0221 P_L + 62.064 \ . \tag{A.1}$$

The desired laser frequency f_{Set} is converted to TEC temperature T_{TEC} and passed to the laser drive, through the following conditional conversion;

$$T_{\mathrm{TEC}} = -\frac{f_{Set}}{20.555} + \begin{cases} (-0.0230 I_L + 32.128) & \text{if } I_L \leq 72.05 \\ (-0.0275 I_L + 33.659) & \text{otherwise .} \end{cases} \tag{A.2}$$

where the DBR laser mode hop is accounted for by using separate models based on the selected laser current with respect to the mode hop threshold $I_L \leq 72.05$.

Heater driver calibration

The desired temperature of the cell T_{Set} is converted to a PWM phase offset value θ through the following conversion (derived through measured phase to temperature calibration);

$$\theta = -0.0082T_{Set}^2 + 0.1676T_{Set} + 135.13 \ , \tag{A.3}$$

which in turn is passed to the heater driver, as discussed in Section 3.2. The laser parameters are implemented very quickly, however heating of the cell temperature is the slowest process.

Coil driver calibration

The coils are driven by the current driver which requires an input of count number N_{Count}, related to the coil current driver full current range I_{Range} by;

$$N_{\mathrm{Count}} = \left| ((B \times C) + I_{\mathrm{Range}}) * \frac{65535}{2I_{\mathrm{Range}}} \right| \ , \tag{A.4}$$

where the applied magnetic field $B = B_x$, B_y or B_z depending on the axis of the coil (x, y or z). The calculated value of current to field C (mA/nT) depends on coil geometry for each individual coil, such that $C = C_x$, C_y or C_z for the corresponding axis.

Appendix B

Automated Machine Learning Strategies for Multi-Parameter Optimisation of a Caesium-Based Portable Zero-Field Magnetometer

Appendix B. Automated Machine Learning Strategies for Multi-Parameter Optimisation of a Caesium-Based Portable Zero-Field Magnetometer

sensors

MDPI

Article

Automated Machine Learning Strategies for Multi-Parameter Optimisation of a Caesium-Based Portable Zero-Field Magnetometer

Rach Dawson *, Carolyn O'Dwyer *, Edward Irwin, Marcin S. Mrozowski, Dominic Hunter, Stuart Ingleby, Erling Riis and Paul F. Griffin

Department of Physics, Scottish Universities Physics Alliance SUPA, University of Strathclyde, Glasgow G4 0NG, UK

* Correspondence: rachel.dawson@strath.ac.uk (R.D.); carolyn.odwyer@strath.ac.uk (C.O.)

Abstract: Machine learning (ML) is an effective tool to interrogate complex systems to find optimal parameters more efficiently than through manual methods. This efficiency is particularly important for systems with complex dynamics between multiple parameters and a subsequent high number of parameter configurations, where an exhaustive optimisation search would be impractical. Here we present a number of automated machine learning strategies utilised for optimisation of a single-beam caesium (Cs) spin exchange relaxation free (SERF) optically pumped magnetometer (OPM). The sensitivity of the OPM ($T/\sqrt{Hz}$), is optimised through direct measurement of the noise floor, and indirectly through measurement of the on-resonance demodulated gradient (mV/nT) of the zero-field resonance. Both methods provide a viable strategy for the optimisation of sensitivity through effective control of the OPM's operational parameters. Ultimately, this machine learning approach increased the optimal sensitivity from 500 $fT/\sqrt{Hz}$ to < 109 $fT/\sqrt{Hz}$. The flexibility and efficiency of the ML approaches can be utilised to benchmark SERF OPM sensor hardware improvements, such as cell geometry, alkali species and sensor topologies.

Keywords: magnetometry; atomic; optimisation; machine learning; SERF; caesium

check for updates

Citation: Dawson, R.; O'Dwyer, C.; Irwin, E.; Mrozowski, M.S.; Hunter, D.; Ingleby, S.; Riis, E.; Griffin, P.F. Automated Machine Learning Strategies for Multi-Parameter Optimisation of a Caesium-Based Portable Zero-Field Magnetometer. *Sensors* **2023**, *23*, 4007. https://doi.org/10.3390/s23084007

Academic Editor: Etienne Labyt

Received: 27 February 2023
Revised: 11 April 2023
Accepted: 13 April 2023
Published: 15 April 2023

Copyright: © 2023 by the authors. Licensee MDPI, Basel, Switzerland. This article is an open access article distributed under the terms and conditions of the Creative Commons Attribution (CC BY) license (https://creativecommons.org/licenses/by/4.0/).

1. Introduction

OPMs have shown impacts across many fields of magnetic sensing, with the potential perhaps being most transformative in the field of magnetoencephalography (MEG). The flexible placement of sensing volumes and favourable operating temperature provide significant advantages over superconducting quantum interference devices (SQUIDs) in many contexts. The sensitivity of commercial OPMs approaches that of SQUIDs while providing functional [1] and longitudinal [2] studies with an important new tool. SERF magnetometers demonstrate sensitivities that approach the low-femtoTesla regime, making this type of zero-field sensor ideal for MEG, although recent work has also demonstrated finite-field sensors attaining the requisite sensitivity for these measurements in the Earth's field [3,4]. The majority of reported work in SERF sensors for MEG utilise rubidium as the sensing species. Cs is attractive for MEG as the temperature needed to achieve a comparable vapour pressure is lower than that of other commonly used alkalis, rubidium or potassium. To date, few SERF sensors reported in the literature use Cs [5,6] and only a single sensor is known by the authors that operates in a single-beam configuration [7]. As such, the optimal operation parameters of the sensor are not known a priori.

The optimal signal from the SERF sensor has intrinsic complex dynamics in at least five-dimensions contained within the parameters of cell temperature, laser power, laser detuning, modulation frequency and modulation depth. Some experimental parameter configurations have been well-described in the literature [8,9] and others may be modelled accurately [10]. In general, sensitivity is improved by elevating the temperature of the cell

Appendix B. Automated Machine Learning Strategies for Multi-Parameter Optimisation of a Caesium-Based Portable Zero-Field Magnetometer

to the increase atomic density and subsequently increase spin exchange (SE) collisions. A threshold exists at which the opacity of the cell reduces the transmission of the light through the cell and hence the signal amplitude. Increasing laser power raises the optical pumping efficiency, at the cost of higher intensity noise and broadening of the magnetic resonance (and subsequent reduction of sensitivity). In order to ascertain the best operational parameters for the sensor described here, we have taken an automated approach to optimising the primary experimental parameters with a view to maximising the sensitivity of this device.

Here we present three automated optimisation techniques that have been used independently to assess the best operation parameters based on experimental performance quantified through a chosen cost function C. The techniques include a genetic algorithm, a simplified form of gradient ascent optimisation and an open-source machine-learning package that utilises predictive modelling. We present these automated optimisation techniques in the context of a Cs SERF magnetometer to demonstrate use as a generic routine for finding the optimal operating point for a complex sensor.

Beyond the realms of computer science, automated optimisation and machine learning have been utilised across many disciplines [11–16], and have found success in quantum and particle physics [17–19]. Machine learning has been adopted for the optimisation of experimental parameters for complex systems [20–22], where traditional human-intuition-based experimental control is laborious, inefficient, and may not result in the optimal configuration [23].

The optimisation approach applied here has yielded previously unknown configurations of parameters leading to operation of the magnetometer blue-detuned from the optical absorption peak rather than at peak absorption [24]. It has allowed us to create a robust, flexible and fast test environment for benchmarking cells of various buffer gas pressures and different alkali species, which aids sensor development.

2. Materials and Methods

2.1. Experimental Set-Up

The experimental setup is displayed in Figure 1. A distributed Bragg reflector (DBR) laser close to the $F = 4 \rightarrow F' = 3$ hyperfine transition of the Cs D_1 line is fibre coupled to the sensor package using a non-magnetic fibre coupler (Schäfter Kirchhoff 60FC-4-M12-10-Ti). Laser power and detuning is controlled by a digital butterfly laser diode controller (Koheron CTL200) through direct control of laser current and TEC temperature. Light polarisation is selected with a miniaturised quarter waveplate ($\lambda/4$) that can be manually controlled to allow fine adjustment of polarisation. The beam is incident on a micro-fabricated atomic vapour cell [25], which contains Cs vapour and 211 Torr nitrogen gas. The OPM sensor head [26] consists of all sensing components (cell, optics, PD and coils) in a portable package with external dimensions of 25 mm $\times$ 25 mm $\times$ 50 mm, which is mounted within a 5-layer μ-metal shield (10^5 shielding factor) to attenuate the Earth's magnetic field.

Efforts have been made to reduce the number of magnetic components close to the cell. The cell is mounted on a printed circuit board (PCB), which drives a single 8 Ω non-magnetic aluminium nitride heating resistor. Resistive heating is realised by the application of square-wave current modulation at 274.699 kHz, a frequency far outside the bandwidth of the sensor. The temperature is varied by changing the phase offset of the two square waves that drive a full-bridge class D amplifier. A T-type thermocouple is mounted close to the cell in order to provide temperature feedback.

Appendix B. Automated Machine Learning Strategies for Multi-Parameter Optimisation of a Caesium-Based Portable Zero-Field Magnetometer

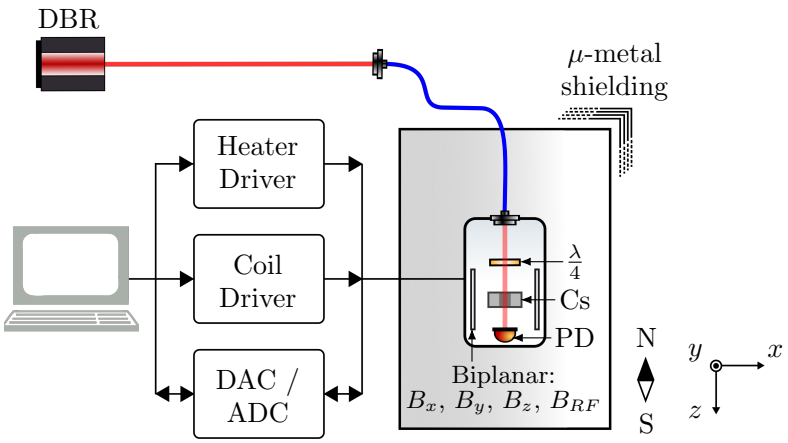

Figure 1. Experimental setup. Elliptically polarised light from a distributed Bragg reflector (DBR) laser close to the $F = 4 \rightarrow F' = 3$ hyperfine transition of the Cs D_1 line is fibre-coupled to pass through a micro-fabricated atomic vapour cell [25,26] filled with a saturated vapour of Cs and 211 Torr of nitrogen buffer gas. The cell is heated through resistive heating by square-wave modulated current provided by a custom high efficiency heater driver. Three pairs of biplanar coils, B_x, B_y, B_z, control the static magnetic field along each axis, and an additional modulation coil, B_{RF}, allows the application of an oscillating field along the y-axis. The static field coils are driven using a custom low-noise current driver [27]. The photodetector (PD) measures light transmitted through the vapour cell. A low nT-level magnetic field environment is provided by a 5-layer μ-metal shield. $\lambda/4$, quarter waveplate; Cs, caesium vapour cell; ADC, analog-to-digital converter; DAC, digital-to-analog converter.

The cell is mounted at the centre of three biplanar-configuration coil pairs designed using open source coil design package "bfieldtools" [28,29], which control the static magnetic field along each axis. Additionally, a modulation coil along the y-axis allows application of an oscillating magnetic field. The static-field coils are driven using a custom low-noise current driver [27]. The light transmitted through the vapour cell is detected using a photodetector with a custom transimpedance amplifier and the signal is digitised via a 16-bit data acquisition system (National Instruments NI USB-6366).

2.2. Hanle Resonance

The magnetometer derives its measurement of the magnetic field through the transverse zero-field Hanle resonance [10,30], which manifests as a peak in light transmission through the cell when the atoms experience zero magnetic field, seen in Figure 2a. The static magnetic field on each axis may be swept independently in order to null residual fields [10]. B_x, B_y, and B_z denote the magnetic field values that are swept along the x, y and z axes, respectively. B_{x0}, B_{y_0}, and B_{z0} denote the magnetic field values that are applied, respectively, to cancel residual static fields and achieve zero-field. The magnetometer is designed to be operated in the SERF regime, which requires elevated temperatures and a low-field environment such that the spin-exchange collision rate sufficiently exceeds the Larmor frequency.

Appendix B. Automated Machine Learning Strategies for Multi-Parameter Optimisation of a Caesium-Based Portable Zero-Field Magnetometer

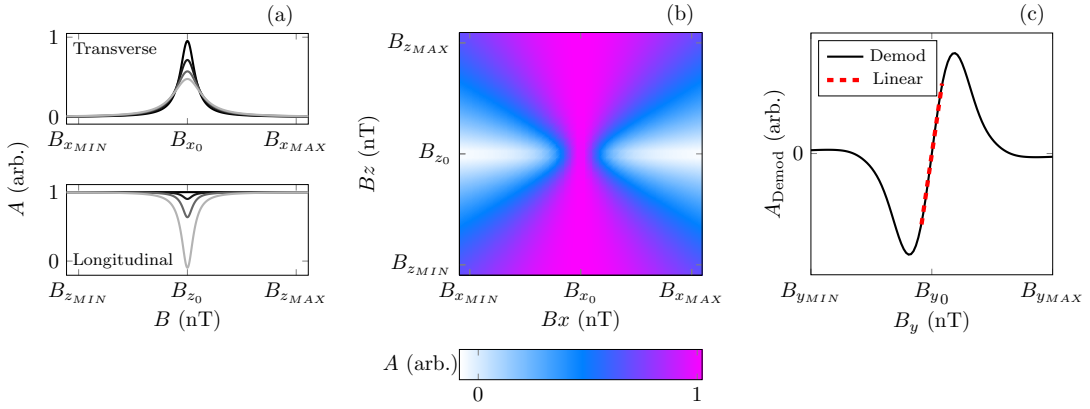

Figure 2. (**a**) (top), Hanle resonances, showing transmission, A, across the transverse axis as a function of longitudinal magnetic field; far detuned from zero-field (light line) to zero field, B_{z_0} (darkest line). (**a**) (bottom), Hanle resonances, showing transmission, A, across the longitudinal axis as a function of the transverse magnetic field; far detuned from zero-field (light line) to zero field, B_{x_0} or B_{y_0} (darkest line). (**b**), Hanle resonances across two axes. The transverse and longitudinal magnetic fields, B_x & B_z, are swept across the x- and z-axes to generate a 2D landscape of the Hanle resonance. Colour indicates the measured light transmission amplitude (A) on the photodetector, normalised with respect to the maximum (1) and minimum (0) transmission. (**c**), modulation of the magnetic field is applied across the y-axis as the transverse field, B_y, is swept from $B_{y_{MIN}}$ to $B_{y_{MAX}}$. The resultant photodiode signal is demodulated and the demodulated amplitude with respect to (B_y) is shown by the black solid line, the linear sensing region is shown by the red dashed line.

The experimental procedure of the magnetometer is as follows: the magnetic field is swept across the x- and z-axes to generate a series of longitudinal Hanle resonances with respect to the transverse field, seen in Figure 2b. This two-dimensional "2D" Hanle landscape is fit using Equation (1), which describes the longitudinal Hanle resonance as a function of the field applied in the transverse, in this case x, direction [10];

$$S_{2D} = A\left(\frac{\Gamma^2 + (B_x + B_{x0})^2}{\Gamma^2 + (B_z + B_{z0})^2}\right) - V_0\,, \tag{1}$$

where V_0 is the constant background offset voltage, A is the signal amplitude, and Γ is the full-width at half-maximum (FWHM). The point at which the transverse resonance is the sharpest indicates the value of the applied transverse and longitudinal field at which the atoms experience close to zero-field. These fields, B_{x0} and B_{z0}, are applied, effectively zeroing the field in the x- and z-axes. The final stage steps the field along the y-axis to generate a single one-dimensional "1D" transverse Hanle resonance, seen in Figure 2a and [10]. The 1D resonance is fit to the model described as:

$$S_{1D} = A\left(\frac{\Gamma^2}{\Gamma^2 + (B_y - B_{y_0})^2}\right) + V_0\,. \tag{2}$$

Subsequently, the magnetic field across the $y-$axis is swept, with an additional field modulation applied along the same axis at an amplitude (A_{mod}) and frequency (F_{mod}) determined from Γ. For each value of B_y, the signal is demodulated. The demodulated line shape, as seen in Figure 2c, shows the linear sensing region (red dashed line), and the gradient (mV/nT) is used to generate the first cost function, Equation (3).

Finally, a free-running measurement of the magnetic field is carried out, allowing the sensor noise floor and hence sensitivity to be characterised. The calculated B_{x0}, B_{y_0}

and B_{z0} fields are applied, effectively zeroing the remaining magnetic field experienced by the sensing atoms across all three axes. Modulation is again applied to the magnetic field along the y-axis, and the response of the atoms is measured through the photodetector. Analysis of this measurement through the square root of the power spectral density (PSD) may be scaled by the measured demodulated gradient (mV/nT) to assess the noise floor of the sensor. The power in the noise spectrum across the defined frequency band of interest (5–20 Hz) is calculated, and this serves as the second cost function (Equation (4)) for optimising the OPM.

Machine Learning

Machine learning works to identify a global maximum or minimum within a parameter space. Here, we will demonstrate and compare multiple machine learning algorithms (MLAs) that implement supervised learning. Supervised learning refers to providing the MLA with a quantitative measure of performance known as cost [20]. For all techniques, the MLA and experiment are contained within a closed loop where the MLA controls the experiment, which in turn gathers and returns cost information to the MLA. More specifically, the MLA selects the experimental parameters, which are translated to the experiment through control instrumentation. The experiment automatically completes the zero-field resonance measurements in both 2D and 1D, and calculates cost according to the cost function $C(\rho)$. The cost associated with each parameter set is used by the MLA to inform the next set of parameters to sample.

We define two cost functions, $C_1(\rho)$ and $C_2(\rho)$, to optimise in two distinct ways in order to assess which cost function is most effective. $C_1(\rho)$, measured in (mV/nT), is the gradient of the demodulated lineshape as seen in Figure 2c and given by:

$$C_1(\rho) = \frac{\delta A_{\text{Demod}}}{\delta B_y}, \tag{3}$$

where δA_{Demod} and δB_y are, respectively, the change in amplitude and magnetic field of the demodulated lineshape within the linear range. C_1 has been selected as this corresponds to a "sharp" 1D resonance line-shape, that is, a high amplitude with narrow width, which is a good indicator of OPM performance. Thus, C_1 must be maximised to increase line-shape sharpness and as such a global maximum of C_1 is desired.

$C_2(\rho)$ is a sensitivity approximation measured directly through analysis of the noise floor. A $\sqrt{PSD}$ is taken to extract a series of frequency dependent amplitude values ($X(k)$) that are scaled by the demodulated gradient (C_1) to provide frequency response as a function of magnetic field. The geometric mean of the noise spectrum within our band of interest (5 to 20 Hz) constitutes $C_2(\rho)$, where

$$C_2(\rho) = \left(\prod_{5 \leq k \leq 20}^{n} \frac{\delta A_{\text{Demod}}}{\delta B_y} X(k) \right)^{\frac{1}{n}}. \tag{4}$$

By minimising C_2, which is a measure of the intrinsic noise of the magnetometer in the frequency band of interest, we optimise the magnetic sensitivity. Thus, the location of a global minimum of C_2 across the parameter space is desired.

Both defined cost functions aim to improve sensitivity, where C_2 will achieve this directly and C_1 indirectly.

2.3. Optimisation Techniques

For the total number of experimental parameters, M, a single set of experimental settings (temperature, laser power, etc.) is defined as $X = (x_1, \ldots x_M)$. For each individual set, X_i, an associated cost $C(X_i)$ and uncertainty $U(X_i)$ are found experimentally. All optimisation techniques selected are examples of online optimisation (OO) in which optimisation is implemented concurrently with experimental testing. We employ two evolutionary OO

Appendix B. Automated Machine Learning Strategies for Multi-Parameter Optimisation of a Caesium-Based Portable Zero-Field Magnetometer

algorithms, a gradient ascent OO and a predictive model-based machine learning algorithm. All optimisation methods continue until 250 sets of parameters are tested, known as the end condition, $N_{end} = 250$.

2.3.1. Evolutionary Algorithms

Evolutionary algorithms are heuristic search-based approaches to solving problems. The processes of evolutionary algorithms are inspired by nature and biological systems [31], the scheme is shown here in Figure 3. This includes the evaluation of the performance of individuals within a population to inform the selection of a new population mimicking "survival of the fittest", a crossover of high-performing individuals to imitate reproduction and mutation. Mutation introduces a stochastic component and aims to drive optimisation to a global maximum or minimum. Evolutionary algorithms are commonly used across many types of optimisation problems [32], due to their robust convergence to a solution. However, this convergence time increases with the system complexity. Here, we will implement two evolutionary algorithms, (a) genetic algorithm (GA) and (b) differential evolution (DE) algorithm. The GA process is displayed in Figure 3a. The GA first randomly creates the initial population, $X(t)$, of N sets of experimental parameters

$$X(t) = \{X_1, \dots X_N\}\,, \tag{5}$$

where t denotes the generation of the population, initially $t = 0$.

All parameters chosen are selected within predefined parameter space limits. Next, we automatically and iteratively evaluate each parameter set, X_i, through experimental testing and find associated cost $C(t)$ and uncertainty $U(t)$ of the entire population, where, $C(t) = (C_1, \dots C_N)$ and $U(t) = (U_1, \dots U_N)$. The selection of the new generation population, $X(t)$ where $t = t + 1$, is based on the best performing sets of experimental parameters from the previous generation $X(t-1)$. To achieve this, $X(t-1)$ is ranked by $C(t-1)$ with respect to $U(t-1)$ and the best performing $\frac{N}{2}$ sets of parameters are added to $X(t)$. The remaining $\frac{N}{2}$ sets of parameters are created through a crossover. Crossover occurs between sets of parameters from the previous generation to create sets for the new generation, shown in Figure 3a and given by:

$$X(t)_j = \{x | x \in X_a(t-1) \text{ if } x_i \leq CP, x \in X_b(t-1) \text{ if } x_i > CP\} \tag{6}$$

$$X(t)_k = \{x | x \in X_b(t-1) \text{ if } x_i \leq CP, x \in X_a(t-1) \text{ if } x_i > CP\}\,, \tag{7}$$

where $X(t)_j$ and $X(t)_k$ are "children" sets of "parent" $X_a(t-1)$ and $X_b(t-1)$. The crossover point, CP, refers to an individual element, x_i, of the parent sets. The final step is to introduce random mutation to prevent optimisation for a local minimum or maximum. The new population, $X(t)$, is then evaluated experimentally and the algorithm continues until the end condition is met.

The process of DE deviates from GA as shown in Figure 3b, while maintaining the same evolutionary elements. The initial population of sets of parameters is created as defined in Equation (5) and similarly evaluated to find the associated cost $C(t)$ and uncertainty $U(t)$ of the entire population. The mutation element is incorporated through creation of a new set, V, where $V = X_c + (X_a - X_b)$ and X_a, X_b and X_c are randomly selected parameter sets. Crossover occurs between V and a randomly selected target set X_T to produce an additional set Q. Q is evaluated experimentally and replaces X_T in the new generation where $t = t + 1$, if C_Q outperforms C_T. Lastly, three random sets and a target set are selected from the new population, $X(t)$. The algorithm continues until the end condition is met.

Appendix B. Automated Machine Learning Strategies for Multi-Parameter Optimisation of a Caesium-Based Portable Zero-Field Magnetometer

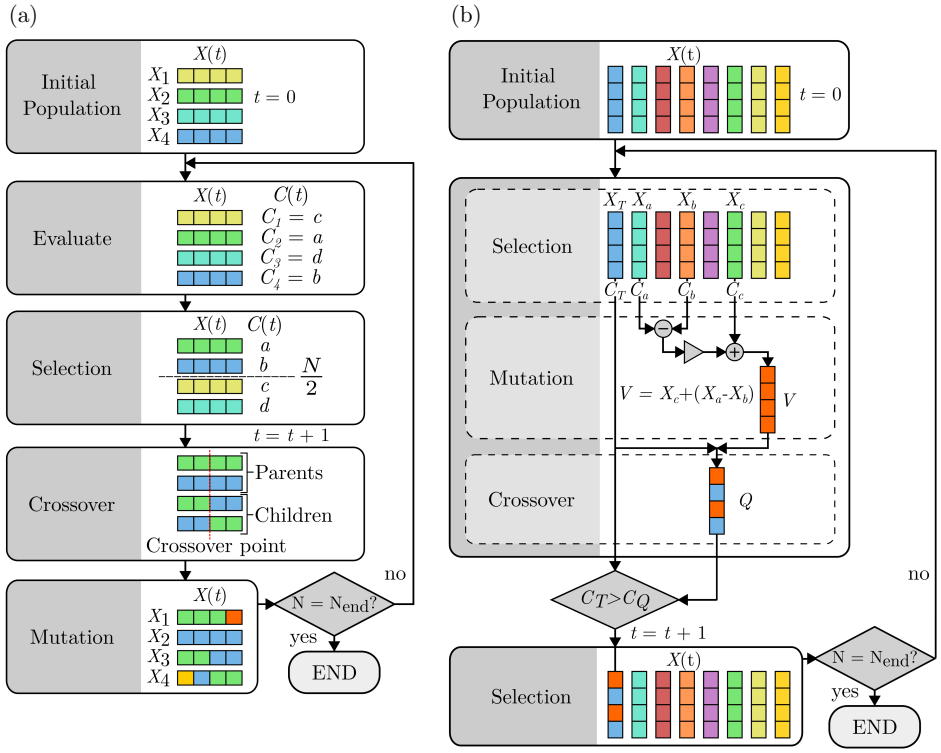

Figure 3. Two evolutionary algorithm processes. (**a**,**b**) share evolutionary elements of initial population formation, selection, crossover and mutation. For both algorithms, the initial population $X(t)$ contains a population of N sets of parameter settings. The colour indicates each set of parameter settings. t, generation or loop number; $t = t + 1$, the next generation; and $C(t)$, measured cost. Both algorithms repeat until the end condition is met, where the number of sets of parameters tested N is equal to 250 (N_{end}). (**a**) Genetic algorithm (GA) process. The initial population is generated and evaluated for cost, with individual costs denoted as C_i. $\frac{N}{2}$ parameter sets are selected for the next generation based on ranked cost. The best performing $\frac{N}{2}$ are used as "parents" to produce "children" sets during crossover with respect to the crossover point. Mutation of individual parameter values randomly occurs in the new population. (**b**) Differential evolution (DE) process. The initial population is generated and evaluated for cost where three random sets X_a, X_b & X_c and a target set X_T are selected. A new set V is created during mutation from the randomly selected sets, and used in a crossover with the target set to make a new set Q. C_Q, the cost of Q, is evaluated and measured against C_T, the cost of the target set. The target set is replaced in a new generation if $C_Q > C_T$ (for C_1) or $C_Q < C_T$ (for C_2).

2.3.2. Gradient Ascent

Gradient ascent algorithms are a first-order process. As such, the differential of the changing cost $C(\rho)$ is used to inform the learning process [33]. Here, we implement a form of batch gradient algorithm, displayed in Figure 4. Small batches of data are tested to find the optimal parameters based on the gradient of the cost across the batch. Learning occurs between iterations of batches. Batch gradient algorithms guarantee convergence to a local or global maximum or minimum. However, as the batch sizes are pre-defined, some

points tested may be redundant, especially compared to stochastic gradient processes with a higher learning rate [34–36].

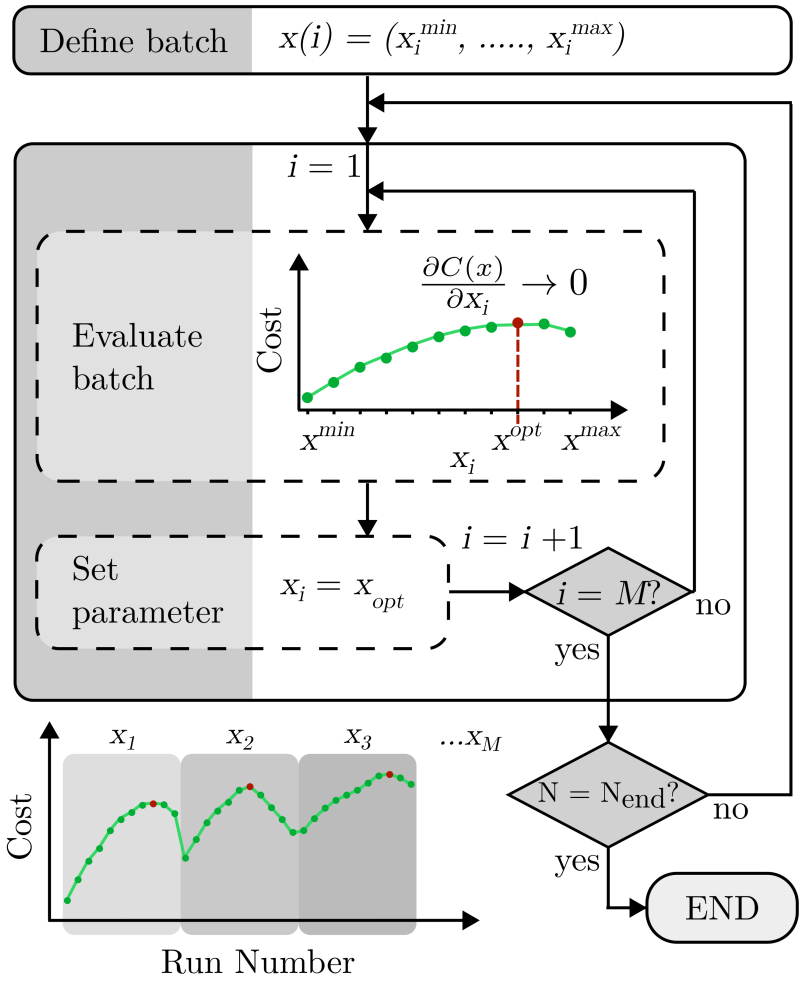

Figure 4. Gradient ascent algorithm process. $x(i)$, a vector value for a single parameter x_i ranging from minimum x_i^{min} to maximum x_i^{max} as defined by parameter space range. i, the individual parameter selected. Initially, the first parameter is selected for the first batch $i = 1$. All other parameters are kept constant. The batch is evaluated based on cost, indicated in green, to find where the gradient tends to zero, $\frac{\partial C(\rho)}{\partial x} \rightarrow 0$ indicated in red. The corresponding parameter value x^{opt} is then set for this parameter for the next batch, $i = i + 1$. This continues until all parameters are used as batches, for a total number of parameters M. The segmented graph shows this process as a function of the run number. This process in turn repeats until the end condition is met, where the number of sets of parameters tested N is equal to 250 (N_{end}).

In this context, each batch $x(i)$ is defined as a broad sweep of a single parameter across the full range for that parameter in regular intervals as follows:

$$x(i) = (x_i^{min}, x_i^{min} + n, ..x_i^{max}) \,, \tag{8}$$

Appendix B. Automated Machine Learning Strategies for Multi-Parameter Optimisation of a Caesium-Based Portable Zero-Field Magnetometer

where i denotes the individual parameter, n is the interval for the parameter, and x_i^{max} and x_i^{min} are the maximum and minimum values of the specific parameter from the defined parameter range. The first batch targets the first parameter only, where $i = 1$. The non-target parameter values are kept constant throughout the batch testing at the previously found optimum, or initially selected randomly. Evaluation of the batch experimentally finds the associated cost for each element of $x(i)$. The cost curve of the batch is used to find where the gradient tends to zero, $\frac{\partial C(\rho)}{\partial x} \rightarrow 0$. The value of x_i is set to the corresponding parameter value, x_{opt}, for the next batch iteration. Each iteration changes the target parameter used for the batch, where $i = i + 1$ after each batch, up to the total number of M parameters. One full process of the gradient algorithm occurs after all parameters have been selected as the target parameter, which in turn loops until the end condition is met.

2.3.3. Gaussian Process Regression

The Gaussian process (GP) regression OO method creates a model defining how each experimental parameter relates to the experimentally found cost, known as the cost-landscape. The cost-landscape is formed through training the MLA with data collected by DE for $2M$ sets of parameters. The model generates correlation lengths to indicate how sensitive the cost is to each parameter, where the correlation length is inversely proportional to its influence on cost. The cost-landscape model informs the selection of new parameter values to test. Each iteration informs the model and contributes to defining the noise level of "expected cost" to "found cost", i.e., the variance of the cost if measured at the same set of parameters many times. For this method, we utilise M-LOOP (Machine Learning Online Optimization Package), an open-source Python-based machine learning toolkit [20], which utilises DE and GP during optimisation. While GP regression is the most sophisticated MLA we employ, Gaussian processes lose efficiency in high dimensional spaces and the computational time required scales with the cube of the number of tests.

2.4. Parameters

The parameters, p, selected for optimisation are: (1) Cell Temperature T, (2) Laser Power LP and (3) Laser Detuning LD. These parameters are intrinsically linked with complex dynamics as described in Section 4. Each parameter is directly controlled through experimental hardware.

A further two parameters are defined, namely (4) Modulation Amplitude B_{Mod} and (5) Modulation Frequency ω_{Mod}. Both amplitude and frequency of the applied modulated magnetic field influence light absorption and magnetometer performance. These parameters are not directly selected, rather dimensionless factors A_{Mod} and F_{Mod} are defined that are tied to the magnetic resonance line width of the magnetometer response, defined as:

$$A_{Mod} = \frac{B_{Mod}}{\Gamma} \tag{9}$$

$$F_{Mod} = \frac{\omega_{Mod}}{\Gamma\gamma}, \tag{10}$$

where total relaxation Γ is equal to the HWHM width extracted from magnetic resonance and γ is the gyromagnetic ratio ($3.5 \times 2\pi$ Hz/nT for Cs). B_{Mod} and ω_{Mod} are dependent factors, and the modulation index, m_i, defines this dependency:

$$m_i = \frac{\gamma B_{Mod}}{q(P)\omega_{Mod}}, \tag{11}$$

where $q(P)$ is the nuclear slowing-down factor at high polarisation [37]. It has been shown that the optimal modulation index occurs when $m_i = 0.5 - 1$ [38]. All control parameter ranges are defined in Table 1.

Appendix B. Automated Machine Learning Strategies for Multi-Parameter Optimisation of a Caesium-Based Portable Zero-Field Magnetometer

Table 1. Definition of all controlled parameters (p) used for optimisation, with corresponding units. Min (p), the minimum value for each parameter. Max (p), the maximum value for each parameter. Default (p), chosen default value if parameter is not directly optimised during optimisation.

Parameter	Min (p)	Max (p)	Default (p)	Unit
Temperature	115	140	-	°C
Laser Power	0.5	6	-	mW
Laser Detuning	−20	20	-	GHz
A_{Mod}	0.2	1.5	0.5	dimensionless
F_{Mod}	0.2	1.5	1	dimensionless

3. Results

We applied the MLAs presented in Section 2.3 to optimise the sensitivity of a single-beam Cs SERF OPM. Two cost functions (C_1, C_2) are utilised to investigate cost function suitability. The number of parameters optimised ($M = 3$: LD, LP, T, $M = 5$: LD, LP, T, A_{Mod}, F_{Mod}) is varied to demonstrate MLA robustness with respect to optimisation complexity. In total, four independent optimisation schemes are measured:

Scheme 1. Cost = C_1, $M = 3$
Scheme 2. Cost = C_1, $M = 5$
Scheme 3. Cost = C_2, $M = 3$
Scheme 4. Cost = C_2, $M = 5$

Three MLAs are used per optimisation scheme: (1) Genetic Algorithm (GA), (2) Gradient Descent algorithm (GD) and (3) Gaussian Process Regression (GP). The full parameter space used for all optimisation schemes is defined in Table 1. For equality between optimisation schemes, all methods are initialised with a random set of parameter values, often initially producing no magnetic resonance signal. Each MLA ran until the end condition, requiring 250 sets of experimental settings to be tested, $N_{end} = 250$, taking approximately 4 h in total per MLA. Both cost functions were measured during each technique, regardless of the selected cost function, to allow comparison.

To benchmark the optimised sensitivity of all MLAs and optimisation schemes, we first manually optimised through human-intuition-based experimental control. During human optimisation, the operational parameters are manually selected and the subsequent measured sensitivity informs the selection of the next parameters based on intuition. The human optimisation process found an optimal sensitivity of 500 fT/$\sqrt{\text{Hz}}$, in approximately 4 h.

The results of all optimisation schemes for all MLAs are shown in Figure 5. Each row in Figure 5 displays the results for an individual optimisation scheme, with Cost Function $C(\rho)$ and the number of parameters (M) indicated accordingly. Progression of each technique can be seen in Figure 5a,d,g,j, where cost is a function of the experimental run number and the moving maximum (for C_1) or minimum (for C_2) throughout optimisation run is indicated by the solid line for each MLA. Figure 5b,e,h,k show the corresponding FFT for the optimal parameters found per MLA, with the sensitivity shown as a function of frequency (Hz) in the bandwidth of interest (5 to 20 Hz). Figure 5c,f,i,l depict the corresponding demodulated line shape for the optimal parameters found per MLA.

Appendix B. Automated Machine Learning Strategies for Multi-Parameter Optimisation of a Caesium-Based Portable Zero-Field Magnetometer

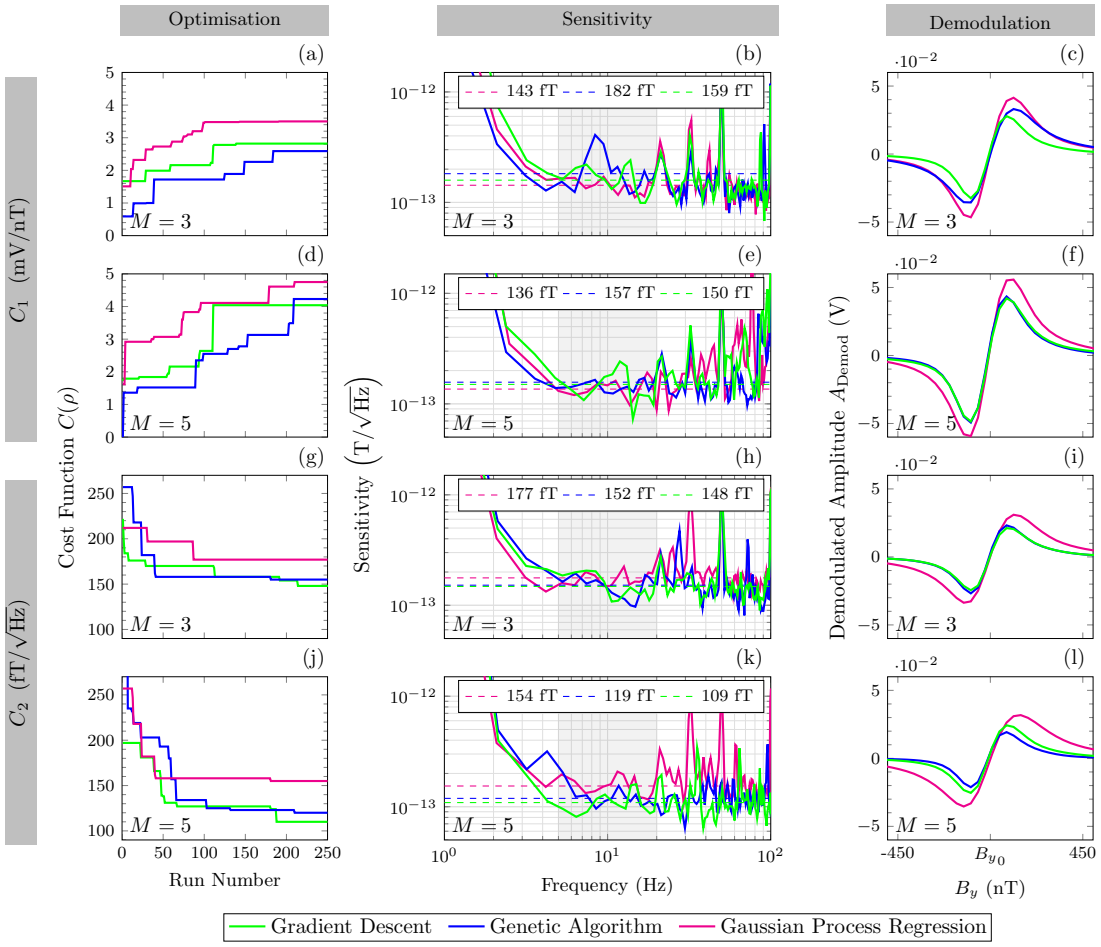

Figure 5. All figure parts contain the following optimisation techniques, gradient descent algorithm in green , genetic algorithm in blue and Gaussian process regression model in pink. M, the number of parameters optimised. Row 1 & 3, (**a–c,g–i**), optimisation of 3 parameters ($M = 3$). Row 2 & 4, (**d–f,j–l**) optimisation of 5 parameters ($M = 5$). Row 1 & 2, (**a–f**), optimise for maximising cost function C_1 the demodulated line shape gradient (mV/nT). Row 3 & 4, (**g–l**), optimise for minimising cost function C_2, calculated sensitivity ($\mathrm{T}/\sqrt{\mathrm{Hz}}$). Column 1 "Optimisation", (**a,d,g,j**), show Cost function as a function of run number. The solid line indicates the moving maximum per optimisation technique. Column 2 "Sensitivity", (**b,e,h,k**), shows corresponding FFT for the optimal parameters found per optimisation technique. Sensitivity is shown as a function frequency (Hz), raw data are shown by solid lines. The frequency band of interest (5 to 20 Hz) is highlighted in grey. Averaged sensitivity in this band is shown by the dashed line (value represented in the key). Column 3, "Demodulation", (**c,f,i,l**), shows a corresponding demodulated line shape for the optimal parameters found per optimisation technique.

The optimised cost for each MLA and optimisation scheme with corresponding optimal parameter settings can be seen in Table 2. All optimisation schemes resulted in large cost improvement throughout optimisation. Convergence of optimised values occurred within each optimisation scheme. The mean and standard deviation across all ML techniques within each scheme are summarised below:

Appendix B. Automated Machine Learning Strategies for Multi-Parameter Optimisation of a Caesium-Based Portable Zero-Field Magnetometer

Scheme 1. C_1. All MLAs converged at 2.5 ± 1 mV/nT, equating to a measured sensitivity of 163 ± 20 fT/$\sqrt{\text{Hz}}$.

Scheme 2. C_1. All MLAs converged at 4.4 ± 0.4 mV/nT, equating to a measured sensitivity of 147 ± 11 fT/$\sqrt{\text{Hz}}$.

Scheme 3. C_2. All MLAs converged at a measured sensitivity of 163 ± 15 fT/$\sqrt{\text{Hz}}$, equating to a demodulated gradient of 2.2 ± 0.15 mV/nT.

Scheme 4. C_2. All MLAs converged at a measured sensitivity of 132 ± 23 fT/$\sqrt{\text{Hz}}$, equating to a demodulated gradient of 2.8 ± 0.9 mV/nT.

Table 2. Optimal parameters found for the following optimisation techniques, Genetic Algorithm (GA), Gradient Descent algorithm (GD) and Gaussian process (GP). The number of parameters tested, M, is specified for each optimisation run. T, cell temperature ($^\circ C$). LP, laser power (mW). LD, laser detuning (GHz). A_{Mod}, modulation amplitude factor (dimensionless). F_{Mod}, modulation frequency factor (dimensionless). m_i, modulation index (dimensionless). $C(\rho)$ defines the cost function implemented. C_1 is the demodulated lineshape gradient (mV/nT), with uncertainty taken as the geometric standard deviation across the frequency band of interest. C_2 is the calculated sensitivity (fT/$\sqrt{\text{Hz}}$), with uncertainty taken as the linear fitting error across demodulated linear region. Γ is the full-width at half-maximum (FWHM) of the magnetic resonance (nT), with uncertainty taken as the fit error to Equation (2). Values in grey indicate parameters that were not optimised during operation.

MLA	M	$C(\rho)$	C_1	C_2	Γ	T	LD	LP	A_{Mod}	F_{Mod}	m_i
GD	3	C_1	2.82 ± 0.03	158.62 ± 1.3	132.51 ± 1.5	119.41	8.24	6.00	0.50	1.00	0.55
GA	3	C_1	2.59 ± 0.02	182.39 ± 1.4	183.27 ± 2.1	115.00	3.00	5.35	0.50	1.00	0.55
GP	3	C_1	3.50 ± 0.03	143.40 ± 1.2	168.83 ± 1.6	115.00	8.00	6.00	0.50	1.00	0.55
GD	5	C_1	4.04 ± 0.02	150.24 ± 1.5	130.06 ± 2.1	118.85	10.77	5.58	1.50	0.30	5.51
GA	5	C_1	4.23 ± 0.02	157.62 ± 1.3	98.81 ± 2.0	123.00	7.00	5.32	1.48	0.39	4.21
GP	5	C_1	4.75 ± 0.03	136.30 ± 1.2	147.36 ± 1.2	120.13	6.22	6.00	1.50	0.21	7.82
GD	3	C_2	2.10 ± 0.02	148.28 ± 1.3	143.36 ± 2.5	117.94	5.88	5.35	0.50	1.00	0.55
GA	3	C_2	2.35 ± 0.02	152.30 ± 1.3	136.66 ± 1.3	119.00	4.00	4.66	0.50	1.00	0.55
GP	3	C_2	2.31 ± 0.02	177.40 ± 1.3	192.81 ± 1.6	115.01	3.49	5.57	0.50	1.00	0.55
GD	5	C_2	2.22 ± 0.03	109.59 ± 1.3	137.70 ± 1.6	118.85	7.69	5.58	0.70	0.80	0.96
GA	5	C_2	1.95 ± 0.02	119.76 ± 1.2	111.05 ± 2.1	121.00	7.00	5.24	0.97	1.15	0.93
GP	5	C_2	3.65 ± 0.02	154.81 ± 1.2	203.05 ± 1.6	115.00	3.00	5.50	1.09	1.00	1.20

The optimum sensitivity of 109 fT/$\sqrt{\text{Hz}}$ was identified by the gradient descent algorithm (with an uncertainty of ± 1 fT/$\sqrt{\text{Hz}}$ taken from the geometric standard deviation across the frequency band of interest) using five parameters ($M = 5$) and direct optimisation of sensitivity (C_2). The optimum demodulated gradient of 4.75 mV/nT was identified (with an uncertainty of ± 0.03 mV/nT, taken as the linear fitting error across demodulated linear region) by the Gaussian process regression model using five parameters and direct optimisation of demodulated gradient (C_1).

The GP model is the most sophisticated MLA demonstrated in this paper. Due to the nature of the optimisation method, as described in Section 2.3.3, a cost-landscape depicting how each parameter affects the measured cost is produced throughout the optimisation process. Figure 6 shows the measured data for each parameter as a function of cost, for optimisation schemes 2 and 4 (5 parameter optimisations). The parameter cost-landscape model is indicated with a line, and the 95% confidence interval generated by the model is indicated by the shaded region. Many measured points for all parameters lie outside the confidence interval due to the nature of multi-parameter optimisation, where the optimised value of one parameter may produce a poor cost value if other parameters are not optimised. The confidence interval shows the trust region of the models predictive landscape after all measurement has been completed.

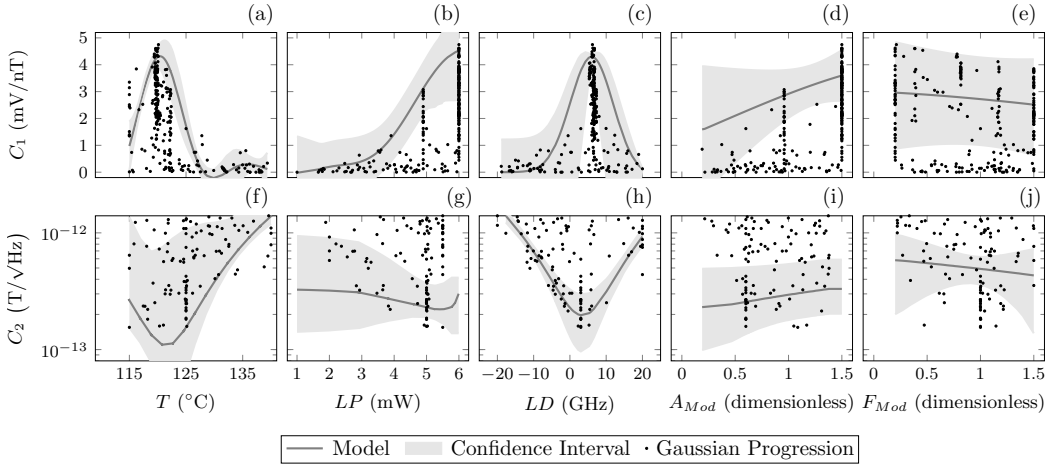

Figure 6. Data and models resulting from the Gaussian process regression model MLA, from a 5 parameter optimisation scheme ($M = 5$). The 5 parameters optimised are cell temperature (T), laser power (LP), laser detuning (LD), modulation amplitude factor (A_{Mod}) and modulation frequency factor (F_{Mod}). Each part shows a parameter as a function of the cost. Row 1, (**a–e**), shows optimisation for cost function C_1, the demodulated line shape gradient (mV/nT). Row 2 , (**f–j**) optimisation for cost function C_2, calculated sensitivity (T/$\sqrt{\text{Hz}}$). Marks indicate measured values from optimisation, solid line indicates the Gaussian process predicted cost-landscape and shaded region indicates the model provided 95% confidence interval of the cost-landscape.

4. Discussion

The sensitivity of the Cs OPM has been improved by all of the MLAs presented in comparison to human optimisation over comparable run-time. This comprehensive improvement indicates the suitability of automated optimisation methods for experimental parameter optimisation tasks in optically pumped magnetometry.

The use of 3 MLAs allowed for comparison of these techniques to aid recommendations for suitability. In this use case, all techniques appear capable, with no single technique standing out as significantly more favourable. Completing the MLA techniques for a differing number of parameters allows comparison of the robustness of the MLA techniques to the system complexity. Interestingly, the more simple MLAs (GA and GD) proved most successful for direct sensitivity optimisation C_2, with GD providing the optimal sensitivity value of 109 fT/$\sqrt{\text{Hz}}$. However, the Gaussian process regression model proved most effective for optimisation of C_1. This suggests that the Gaussian process regression model was more sensitive to the more stochastic nature of cost function C_2.

Increasing the complexity, $M = 5$, proved beneficial to both cost functions. As such, the amplitude and frequency of the applied magnetic modulation are tied to magnetometer performance due to their influence on light absorption. Optical noise has a large contribution in this sensor, and this noise decreases with increased absorption. Furthermore, low frequency 1/f noise decreases with increasing modulation frequency. Each five parameter optimisation scheme converged before the end condition, suggesting that, in multi-parameter systems with five parameters, all MLAs are suitable.

The implementation of two cost functions, C_1 and C_2, aids identification of the most suitable cost function for this purpose. Table 2 shows relative alignment of the best parameter values between cost functions. The peak sensitivity found indirectly (C_1) is 30 fT/$\sqrt{\text{Hz}}$ higher than through direct sensitivity optimisation (C_2). As such, C_1 acts as a reasonable proxy for sensitivity optimisation without specifically measuring sensitivity. C_1 requires less data collection and corresponding sensitivity measurements may be taken after the fact. C_2 takes longer experimentally and computationally and is more susceptible

Appendix B. Automated Machine Learning Strategies for Multi-Parameter Optimisation of a Caesium-Based Portable Zero-Field Magnetometer

to extraneous environmental and technical noise. However, 5 parameter optimisation using C_1 optimised the modulation frequency to a much lower frequency. The subsequent modulation index for these optimised values are also far outside the expected range ($m_i > 5$). This highlights a key drawback of optimisation using C_1, that technical noise contributions are not considered.

A benefit of the implementation of the GP is the production of the cost-landscape model that defines how influential each parameter is on performance. From this model, Figure 6, clear trends can be seen that span across both cost functions, for example, the peak in temperature for C_1 aligns with the trough in C_2. This is likely due to the increased sensitivity gained when the temperature of the cell has increased atomic vapour density sufficiently to reach the SERF regime. As cell temperature is increased, we see a subsequent improvement of sensitivity up to 120 °C, after which the opacity of the cell is increased by the increasing atomic density, allowing less light to reach the detector.

Figure 6 also shows mirrored trends for laser detuning. However, a deviation between the laser power landscape between cost functions is also present. The peak laser power required for C_1 continues to increase beyond the defined range, whereas the optimum laser power for C_2 saturates at 5 mW. This could be due to the increasing laser power detrimentally affecting sensitivity due to intensity noise with increased laser power, which does not degrade C_1 to the same degree. These trends suggest that either cost function is suitable for optimisation if intensity noise is taken into consideration.

The predicted cost-landscapes for A_{Mod} and F_{Mod} (Figure 6) show broad trends with large confidence intervals, suggesting that the relationship between these parameters and the cost functions are not well-defined. Table 2 shows in the results for optimisation scheme 4 (C_2, $M = 5$) that the optimised values for modulation amplitude and frequency gave a modulation index within the expected optimal values (m_i =0.5 − 1). While clear gains in sensitivity were provided by increasing the number of parameters optimised, C_2 is advised for directly optimising sensitivity while keeping modulation values within expected optimal conditions.

It is interesting to note that the optimal detuning parameter found is positively detuned from the optical absorption peak (Table 2). It appears that the effect of the buffer gas introduces complex optical pumping dynamics in the atomic system, likely tied to depopulation on the $F = 3$ ground state. The results of the MLA techniques show that the detuning and power dependence are non-trivial. These results may vary depending on cell parameters such as the optical path length and buffer gas pressure. The techniques shown here will allow future cells to be characterised in an efficient and comprehensive manner.

With an optimised sensitivity of 109 fT/$\sqrt{\text{Hz}}$, the ML methods here have aided the tuning of operational parameters of a SERF OPM to facilitate a sensitivity suitable for use in magnetoencephalography.

Author Contributions: Conceptualisation, R.D., C.O., E.R., P.F.G. and S.I.; methodology, R.D.; software, R.D., C.O., M.S.M. and E.I.; validation, R.D., D.H., C.O.; formal analysis, R.D.; investigation, R.D.; resources, E.R. and P.F.G.; data curation, R.D.; writing—original draft preparation, R.D.; writing—review and editing, R.D., C.O., S.I., D.H, P.F.G., and E.R.; visualization, R.D.; supervision, E.R., P.F.G., S.I. and C.O.; project administration, E.R., P.F.G., S.I. and C.O.; funding acquisition, E.R. and P.F.G. All authors have read and agreed to the published version of the manuscript.

Funding: This research was funded by UKRI grant number EP/T001046/1.

Institutional Review Board Statement: Not applicable.

Informed Consent Statement: Not applicable.

Data Availability Statement: All data created during this research are openly available from Pure Data. DOI: https://doi.org/10.15129/e31fe899-cfa6-47a3-8960-fad048c43d23, accessed on 14 February 2023.

Appendix B. Automated Machine Learning Strategies for Multi-Parameter Optimisation of a Caesium-Based Portable Zero-Field Magnetometer

Acknowledgments: The authors acknowledge and thank James P. McGilligan, David P. Burt and Kelvin Nanotechnology for the manufacture and supply of the atomic vapour cell used within this research.

Conflicts of Interest: The authors declare no conflict of interest. The funders had no role in the design of the study; in the collection, analyses, or interpretation of data; in the writing of the manuscript, or in the decision to publish the results.

References

1. Boto, E.; Holmes, N.; Leggett, J.; Roberts, G.; Shah, V.; Meyer, S.S.; Muñoz, L.D.; Mullinger, K.J.; Tierney, T.M.; Bestmann, S.; et al. Moving magnetoencephalography towards real-world applications with a wearable system. *Nature* **2018**, *555*, 657–661. [CrossRef] [PubMed]
2. Hill, R.M.; Boto, E.; Holmes, N.; Hartley, C.; Seedat, Z.A.; Leggett, J.; Roberts, G.; Shah, V.; Tierney, T.M.; Woolrich, M.W.; et al. A tool for functional brain imaging with lifespan compliance. *Nat. Commun.* **2019**, *10*, 1–11. [CrossRef] [PubMed]
3. Limes, M.E.; Foley, E.L.; Kornack, T.W.; Caliga, S.; McBride, S.; Braun, A.; Lee, W.; Lucivero, V.G.; Romalis, M.V. Portable magnetometry for detection of biomagnetism in ambient environments. *Phys. Rev. Appl.* **2020**, *14*, 011002. [CrossRef]
4. Zhang, R.; Xiao, W.; Ding, Y.; Feng, Y.; Peng, X.; Shen, L.; Sun, C.; Wu, T.; Wu, Y.; Yang, Y.; et al. Recording brain activities in unshielded Earth's field with optically pumped atomic magnetometers. *Sci. Adv.* **2020**, *6*, 8792–8804. [CrossRef]
5. Ledbetter, M.P.; Savukov, I.M.; Acosta, V.M.; Budker, D.; Romalis, M.V. Spin-exchange-relaxation-free magnetometry with Cs vapor. *Phys. Rev. At. Mol. Opt. Phys.* **2008**, *77*, 1–7. [CrossRef]
6. Sheng, J.; Wan, S.; Sun, Y.; Dou, R.; Guo, Y.; Wei, K.; He, K.; Qin, J.; Gao, J.H. Magnetoencephalography with a Cs-based high-sensitivity compact atomic magnetometer. *Rev. Sci. Instrum.* **2017**, *88*, 094304. [CrossRef] [PubMed]
7. Chen, Y.; Chen, Y.; Zhao, L.; Zhang, N.; Yu, M.; Ma, Y.; Han, X.; Zhao, M.; Lin, Q.; Yang, P.; et al. Single beam Cs-Ne SERF atomic magnetometer with the laser power differential method. *Opt. Express* **2022**, *30*, 16541–16552. [CrossRef]
8. Fang, J.; Li, R.; Duan, L.; Chen, Y.; Quan, W. Study of the operation temperature in the spin-exchange relaxation free magnetometer. *Rev. Sci. Instrum.* **2015**, *86*, 73116. [CrossRef]
9. Li, Q.; Zhang, J.; Li, L.; Zeng, X.; Sun, W. The effects of phase retardation of wave plate on cesium magnetometer sensitivity. *Proc. Appl. Mech. Mater.* **2012**, *203*, 263–267. [CrossRef]
10. Castagna, N.; Weis, A. Measurement of longitudinal and transverse spin relaxation rates using the ground-state Hanle effect. *Phys. Rev. At. Mol. Opt. Phys.* **2011**, *84*, 1–11. [CrossRef]
11. Recknagel, F. Applications of machine learning to ecological modelling. *Ecol. Model.* **2001**, *146*, 303–310. [CrossRef]
12. Rajkomar, A.; Dean, J.; Kohane, I. Machine Learning in Medicine. *N. Engl. J. Med.* **2019**, *380*, 1347–1358. [CrossRef] [PubMed]
13. Chen, J.; Wu, Z.; Bao, G.; Chen, L.Q.; Zhang, W. Design of coaxial coils using hybrid machine learning. *Rev. Sci. Instrum.* **2021**, *92*, 045103. [CrossRef] [PubMed]
14. Horvitz, E.; Mulligan, D. Data, privacy, and the greater good. *Science* **2015**, *349*, 253–255. [CrossRef] [PubMed]
15. Deans, C.; Griffin, L.D.; Marmugi, L.; Renzoni, F. Machine Learning Based Localization and Classification with Atomic Magnetometers. *Phys. Rev. Lett.* **2018**, *120*, 033204. [CrossRef]
16. Meng, X.; Zhang, Y.; Zhang, X.; Jin, S.; Wang, T.; Jiang, L.; Xiao, L.; Jia, S.; Xiao, Y. Machine Learning Assisted Vector Atomic Magnetometry. *arXiv* **2022**, arXiv:2301.05707.
17. Carleo, G.; Troyer, M. Solving the quantum many-body problem with artificial neural networks. *Science* **2017**, *355*, 602–606. [CrossRef]
18. Seif, A.; Landsman, K.A.; Linke, N.M.; Figgatt, C.; Monroe, C.; Hafezi, M. Machine learning assisted readout of trapped-ion qubits. *J. Phys. At. Mol. Opt. Phys.* **2018**, *51*, 174006. [CrossRef]
19. Nakamura, I.; Kanemura, A.; Nakaso, T.; Yamamoto, R.; Fukuhara, T. Non-standard trajectories found by machine learning for evaporative cooling of 87 Rb atoms. *Opt. Express* **2019**, *27*, 20435. [CrossRef]
20. Wigley, P.B.; Everitt, P.J.; Van Den Hengel, A.; Bastian, J.W.; Sooriyabandara, M.A.; Mcdonald, G.D.; Hardman, K.S.; Quinlivan, C.D.; Manju, P.; Kuhn, C.C.; et al. Fast machine-learning online optimization of ultra-cold-atom experiments. *Sci. Rep.* **2016**, *6*, 25890. [CrossRef]
21. Tranter, A.D.; Slatyer, H.J.; Hush, M.R.; Leung, A.C.; Everett, J.L.; Paul, K.V.; Vernaz-Gris, P.; Lam, P.K.; Buchler, B.C.; Campbell, G.T. Multiparameter optimisation of a magneto-optical trap using deep learning. *Nat. Commun.* **2018**, *9*, 00654. [CrossRef] [PubMed]
22. Wu, Y.; Meng, Z.; Wen, K.; Mi, C.; Zhang, J.; Zhai, H. Active Learning Approach to Optimization of Experimental Control. *Chin. Phys. Lett.* **2020**, *37*, 11804. [CrossRef]
23. Barker, A.J.; Style, H.; Luksch, K.; Sunami, S.; Garrick, D.; Hill, F.; Foot, C.J.; Bentine, E. Applying machine learning optimization methods to the production of a quantum gas. *Mach. Learn. Sci. Technol.* **2020**, *1*, 015007. [CrossRef]
24. Shah, V.; Knappe, S.; Schwindt, P.D.; Kitching, J. Subpicotesla atomic magnetometry with a microfabricated vapour cell. *Nat. Photonics* **2007**, *1*, 649–652. [CrossRef]
25. Dyer, S.; Griffin, P.F.; Arnold, A.S.; Mirando, F.; Burt, D.P.; Riis, E.; Mcgilligan, J.P. Micro-machined deep silicon atomic vapor cells. *J. Appl. Phys.* **2022**, *132*, 134401. [CrossRef]

Appendix B. Automated Machine Learning Strategies for Multi-Parameter Optimisation of a Caesium-Based Portable Zero-Field Magnetometer

26. Dawson, R.; O'Dwyer, C.; Mrozowski, M.S.; Irwin, E.; McGilligan, J.P.; Burt, D.P.; Hunter, D.; Ingleby, S.; Griffin, P.F.; Riis, E. A Portable Single-Beam Caesium Zero-Field Magnetometer for Biomagnetic Sensing. 2023, *in press*.
27. Mrozowski, M.S.; Chalmers, I.C.; Ingleby, S.J.; Griffin, P.F.; Riis, E. Ultra-low noise, bi-polar, programmable current sources. *Rev. Sci. Instrum.* **2023**, *94*, 1–9. [CrossRef]
28. Zetter, R.; Mäkinen, A.J.; Iivanainen, J.; Zevenhoven, K.C.J.; Ilmoniemi, R.J.; Parkkonen, L. Magnetic field modeling with surface currents. Part II. Implementation and usage of bfieldtools. *J. Appl. Phys.* **2020**, *128*, 063905. https://doi.org/10.1063/5.0016087.
29. lMakinen, A.J.; Zetter, R.; Iivanainen, J.; Zevenhoven, K.C.J.; Parkkonen, L.; Ilmoniemi, R.J. Magnetic-field modeling with surface currents. Part I. Physical and computational principles of bfieldtools. *J. Appl. Phys.* **2020**, *128*, 063906. https://doi.org/10.1063/5.0016090.
30. Breschi, E.; Weis, A. Ground-state Hanle effect based on atomic alignment. *Phys. Rev. A* **2012**, *86*, 053427. [CrossRef]
31. Siddique, N.; Adeli, H. Nature Inspired Computing: An Overview and Some Future Directions. *Cogn. Comput.* **2015**, *7*, 706–714. [CrossRef]
32. Slowik, A.; Kwasnicka, H. Evolutionary algorithms and their applications to engineering problems. *Neural Comput. Appl.* **2020**, *32*, 12363–12379. [CrossRef]
33. Ruder, S. An overview of gradient descent optimization algorithms. *arXiv* **2016**, arXiv.1609.04747.
34. Darken, C.; Chang, J.; Moody, J. Original appears in Neural Networks for Signal Processing 2. In Proceedings of the 1992 IEEE Workshop, Seattle, WA, USA, 15–18 September 1992.
35. Sweke, R.; Wilde, F.; Meyer, J.J.; Schuld, M.; Fährmann, P.K.; Meynard-Piganeau, B.; Eisert, J. Stochastic gradient descent for hybrid quantum-classical optimization. *Quantum* **2020**, *4*, 01155. [CrossRef]
36. Khaneja, N.; Reiss, T.; Kehlet, C.; Schulte-Herbrüggen, T.; Glaser, S.J. Optimal control of coupled spin dynamics: Design of NMR pulse sequences by gradient ascent algorithms. *J. Magn. Reson.* **2005**, *172*, 296–305. [CrossRef] [PubMed]
37. Seltzer, S.J. Developments in alkali-metal atomic magnetometry. Ph.D. Thesis, Princeton University, Princeton, NJ, USA, 2008.
38. Yin, Y.; Zhou, B.; Wang, Y.; Ye, M.; Ning, X.; Han, B.; Fang, J. The influence of modulated magnetic field on light absorption in SERF atomic magnetometer. *Rev. Sci. Instrum.* **2022**, *93*, 13001. [CrossRef]

Disclaimer/Publisher's Note: The statements, opinions and data contained in all publications are solely those of the individual author(s) and contributor(s) and not of MDPI and/or the editor(s). MDPI and/or the editor(s) disclaim responsibility for any injury to people or property resulting from any ideas, methods, instructions or products referred to in the content.

Bibliography

[1] L. Galvani, *Aloysii Galvani De viribus electricitatis in motu musculari commentarius*, Ex Typographia Instituti Scientiarium (1791).

[2] A. D. Waller, "A Demonstration on Man of Electromotive Changes accompanying the Heart's Beat," *The Journal of Physiology* **8**, 229–234 (1887).

[3] H. Berger, "Über das Elektrenkephalogramm des Menschen," *Archiv für Psychiatrie und Nervenkrankheiten* **87**, 527–570 (1929).

[4] R. İnce, S. S. Adanır, and F. Sevmez, "The inventor of electroencephalography (EEG): Hans Berger (1873–1941)," *Child's Nervous System* **37**, 2723–2724 (2021).

[5] B. D. Denny-Brown, "On the nature of postural reflexes," *Proceedings of the Royal Society of London. Series B, Containing Papers of a Biological Character* **104**, 252–301 (1929).

[6] E. D. Adrian and D. W. Bronk, "The discharge of impulses in motor nerve fibres," *The Journal of Physiology* **67**, 9–151 (1929).

[7] B. Denny-Brown, "The histological features of striped muscle in relation to its functional activity," *Proceedings of the Royal Society of London. Series B, Containing Papers of a Biological Character* **104**, 371–411 (1929).

[8] S. Singh, "Magnetoencephalography: Basic principles," *Annals of Indian Academy of Neurology* **17**, 107 (2014).

[9] R. König, C. Sielużycki, and P. J. Durka, "Tiny Signals from the Human Brain: Acquisition and Processing of Biomagnetic Fields in Magnetoencephalography," *Journal of Low Temperature Physics* **146**, 697–718 (2007).

[10] S. Williamson and L. Kaufman, "Biomagnetism," *Journal of Magnetism and Magnetic Materials* **22**, 129–201 (1981).

[11] H. Reichenberger, S. Schneider, W. Moshage, *et al.*, "Biomagnetic multichannel systems. Principles and application in cardiology," *Clinical Physiology* **12**, 325–333 (1992).

[12] G. Baule and R. McFee, "Theory of Magnetic Detection of the Heart's Electrical Activity," *Journal of Applied Physics* **36**, 2066–2073 (1965).

[13] D. Cohen, E. A. Edelsack, and J. E. Zimmerman, "Magnetocardiograms taken inside a shielded room with a superconducting point-contact magnetometer," *Applied Physics Letters* **16**, 278–280 (1970).

[14] A. Rosen, G. T. Inouye, A. L. Morse, *et al.*, "Magnetic Recordings of the Heart's Electrical Activity with a Cryogenic Magnetometer," *Journal of Applied Physics* **42**, 3682–3684 (1971).

[15] M. Saarinen, P. J. Karp, T. E. Katila, *et al.*, "The magnetocardiogram in cardiac disorders," *Cardiovascular Research* **8**, 820–834 (1974).

[16] V. Kariniemi, J. Ahopelto, P. J. Karpi, *et al.*, "The fetal magnetocardiogram," *Journal of Perinatal Medicine* **2**, 214–216 (1974).

[17] T. Katila, R. Maniewski, T. Poutanen, *et al.*, "Magnetic fields produced by the human eye (invited)," *Journal of Applied Physics* **52**, 2565–2571 (1981).

[18] L. Caruso, T. Wunderle, C. M. Lewis, *et al.*, "In Vivo Magnetic Recording of Neuronal Activity," *Neuron* **95**, 1283–1291 (2017).

[19] Q. Tao, L. Zhang, X. Han, *et al.*, "Magnetic Susceptibility Difference-Induced Nucleus Positioning in Gradient Ultrahigh Magnetic Field," *Biophysical Journal* **118**, 578–585 (2019).

[20] M. C. Vinding, P. Tsitsi, J. Waldthaler, *et al.*, "Reduction of spontaneous cortical beta bursts in Parkinson's disease is linked to symptom severity," *Brain Communications* **2**, fcaa052 (2020).

[21] E. Boto, S. S. Meyer, V. Shah, *et al.*, "A new generation of magnetoencephalography: Room temperature measurements using optically-pumped magnetometers.," *NeuroImage* **149**, 404–414 (2017).

[22] J. Clarke, Y.-H. Lee, and J. Schneiderman, "Focus on SQUIDs in Biomagnetism," *Superconductor Science and Technology* **31**, 080201 (2018).

[23] M. I. Faley, J. Dammers, Y. V. Maslennikov, *et al.*, "High- Tc SQUID biomagnetometers," *Superconductor Science and Technology* **30**, 083001 (2017).

[24] W. Happer and H. Tang, "Spin-exchange shift and narrowing of magnetic resonance lines in optically pumped alkali vapors," *Physical Review Letters* **31**, 273–276 (1973).

[25] T. M. Tierney, N. Holmes, S. Mellor, *et al.*, "Optically pumped magnetometers: From quantum origins to multi-channel magnetoencephalography," *NeuroImage* **199**, 598–608 (2019).

[26] A. Borna, T. R. Carter, A. P. Colombo, *et al.*, "Non-Invasive Functional-Brain-Imaging with an OPM-based Magnetoencephalography System," *PLOS ONE* **15**, e0227684 (2020).

[27] H. Xia, A. Ben-Amar Baranga, D. Hoffman, *et al.*, "Magnetoencephalography with an atomic magnetometer," *Applied Physics Letters* **89**, 211104 (2006).

[28] J. C. Allred, R. N. Lyman, T. W. Kornack, *et al.*, "High-Sensitivity Atomic Magnetometer Unaffected by Spin-Exchange Relaxation," *Physical Review Letters* **89**, 130801 (2002).

[29] M. P. Ledbetter, I. M. Savukov, V. M. Acosta, *et al.*, "Spin-exchange-relaxation-free magnetometry with Cs vapor," *Physical Review A - Atomic, Molecular, and Optical Physics* **77**, 1–7 (2008).

[30] J. Fang, T. Wang, H. Zhang, *et al.*, "Optimizations of spin-exchange relaxation-free magnetometer based on potassium and rubidium hybrid optical pumping," *Review of Scientific Instruments* **85**, 123104 (2014).

[31] H. B. Dang, A. C. Maloof, and M. V. Romalis, "Ultrahigh sensitivity magnetic field and magnetization measurements with an atomic magnetometer," *Applied Physics Letters* **97**, 151110 (2010).

[32] I. I. Sobelman, *Atomic Spectra and Radiative Transitions*, Springer Berlin Heidelberg, Berlin, Heidelberg (1992).

[33] C. J. Foot, *Atomic Physics*, vol. 7, Oxford University Press, Oxford (2015).

[34] D. A. Steck, "Cesium D Line Data," (1998).

[35] G. Breit and I. I. Rabi, "Measurement of Nuclear Spin," *Physical Review* **38**, 2082 (1931).

[36] A. Kastler, "Optical Methods of Atomic Orientation and of Magnetic Resonance*," *Journal of the Optical Society of America* **47**, 460 (1957).

[37] V. Tiporlini and K. Alameh, "High sensitivity optically pumped quantum magnetometer.," *TheScientificWorldJournal* **2013**, 858379 (2013).

[38] S. J. Seltzer, *Developments in Alkali-Metal Atomic Magnetometry*. PhD thesis, Princeton University, New Jersey (2008).

[39] T. Scholtes, S. Woetzel, R. IJsselsteijn, *et al.*, "Intrinsic relaxation rates of polarized Cs vapor in miniaturized cells," *Applied Physics B* **117**, 211–218 (2014).

[40] N. W. Ressler, R. H. Sands, and T. E. Stark, "Measurement of Spin-Exchange Cross Sections for Cs133, Rb87, Rb85, K39, and Na23," *Phys. Rev.* **184**, 102–119 (1969).

[41] N. D. Bhaskar, J. Pietras, J. Camparo, *et al.*, "Spin destruction in collisions between cesium atoms," *Physical Review Letters* **44**, 930–933 (1980).

[42] N. Bererini, P. Minguzzi, and F. Strumia, "Foreign-Gas-Induced Cesium Hyperfine Relaxation," *Physical Review A - Atomic, Molecular, and Optical Physics* **4**, 550–554 (1971).

[43] A. Borna, J. Iivanainen, T. R. Carter, *et al.*, "Cross-Axis projection error in optically pumped magnetometers and its implication for magnetoencephalography systems," *NeuroImage* **247**, 1053–8119 (2022).

[44] G. A. Pitz, C. D. Fox, and G. P. Perram, "Pressure broadening and shift of the cesium D2 transition by the noble gases and N2, H2, HD, D2, CH4, C2H6, CF4, and He3 with comparison to the D1 transition," *Physical Review A - Atomic, Molecular, and Optical Physics* **82**, 042502 (2010).

[45] A. Andalkar and R. B. Warrington, "High-resolution measurement of the pressure broadening and shift of the Cs D1 and D2 lines by N2 and He buffer gases," *Physical Review A - Atomic, Molecular, and Optical Physics* **65**, 032708 (2002).

[46] W. Happer and A. C. Tam, "Effect of rapid spin exchange on the magnetic-resonance spectrum of alkali vapors," *Physical Review A* **16**, 1877–1891 (1977).

[47] I. Savukov and S. J. Seltzer, "Spin-exchange-relaxation-free (SERF) magnetometers," in *Optical Magnetometry*, D. Budker and D. F. Jackson Kimball, Eds., 85–103, Cambridge University Press, Cambridge (2013).

[48] J. Wang, G. Li, K. Fu, *et al.*, "Application of hydrogen for rare-earth gadolinium purification and thermodynamic simulation of system," *Journal of Materials Science* **54**, 13334–13343 (2019).

[49] D. A. Steck, "Rubidium 87 D Line Data," (2001).

[50] T. G. Tiecke, "Properties of Potassium," (2010).

[51] Y. Chen, Y. Chen, L. Zhao, *et al.*, "Single beam Cs-Ne SERF atomic magnetometer with the laser power differential method," *Optics Express, Vol. 30, Issue 10, pp. 16541-16552* **30**, 16541–16552 (2022).

[52] Y. Wang, T. Shi, W. Zhou, *et al.*, "Evaluation of optical parameters for a microminiature Rb vapor cell in a dual-beam SERF magnetometer," *Optics Express* **30**, 23587 (2022).

[53] International Electrotechnical Commission, "IEC 60601-1," (2012).

[54] N. Castagna and A. Weis, "Measurement of longitudinal and transverse spin relaxation rates using the ground-state Hanle effect," *Physical Review A - Atomic, Molecular, and Optical Physics* **84**, 1–11 (2011).

[55] E. Breschi and A. Weis, "Ground-state Hanle effect based on atomic alignment," *Physical Review A* **86**, 053427 (2012).

[56] Y. Yin, B. Zhou, Y. Wang, *et al.*, "The influence of modulated magnetic field on light absorption in SERF atomic magnetometer," *Rev. Sci. Instrum* **93**, 13001 (2022).

[57] V. Shah and M. V. Romalis, "Spin-exchange relaxation-free magnetometry using elliptically polarized light," *Physical Review A* **80**, 013416 (2009).

[58] A. Kastler, "The Hanle effect and its use for the measurements of very small magnetic fields," *Nuclear Instruments and Methods* **110**, 259–265 (1973).

[59] Z. Li, R. T. Wakai, and T. G. Walker, "Parametric modulation of an atomic magnetometer," *Applied Physics Letters* **89**, 134105 (2006).

[60] H. Huang, H. Dong, and L. Chen, "Single-beam three-axis atomic magnetometer," *Appl. Phys. Lett* **109**, 62404 (2016).

[61] J. Zhao, G. Liu, J. Lu, *et al.*, "A Non-Modulated Triaxial Magnetic Field Compensation Method for Spin-Exchange Relaxation-Free Magnetometer Based on Zero-Field Resonance," *IEEE Access* **7**, 167557–167565 (2019).

[62] S. J. Seltzer and M. V. Romalis, "Unshielded three-axis vector operation of a spin-exchange-relaxation-free atomic magnetometer," *Applied Physics Letters* **85**, 4804–4806 (2004).

[63] W. Clark Griffith, S. Knappe, J. Kitching, *et al.*, "Femtotesla atomic magnetometry in a microfabricated vapor cell," *Optics Express, Vol. 18, Issue 26, pp. 27167-27172* **18**, 27167–27172 (2010).

[64] P. Schwindt, S. Knappe, V. Shah, *et al.*, "Microfabricated Atomic Magnetometer," in *IEEE Sensors, 2005.*, 73–76, IEEE (2005).

[65] V. Shah, S. Knappe, P. D. Schwindt, *et al.*, "Subpicotesla atomic magnetometry with a microfabricated vapour cell," *Nature Photonics* **1**, 649–652 (2007).

[66] E. J. Eklund, A. M. Shkel, S. Knappe, *et al.*, "Glass-blown spherical microcells for chip-scale atomic devices," *Sensors and Actuators, A: Physical* **143**, 175–180 (2008).

[67] S. Morales, M. C. Corsi, W. Fourcault, *et al.*, "Magnetocardiography measurements with 4He vector optically pumped magnetometers at room temperature," *Physics in Medicine and Biology* **62**, 7267–7279 (2017).

[68] M. J. Maciel, M. F. Silva, S. Pimenta, *et al.*, "Detection of low-magnetic fields by rubidium (87Rb) vapor cell," *Journal of Physics: Conference Series* **1837**, 012002 (2021).

[69] S. Dyer, P. F. Griffin, A. S. Arnold, *et al.*, "Micro-machined deep silicon atomic vapor cells," *J. Appl. Phys* **132**, 134401 (2022).

[70] Y. J. Kim and I. Savukov, "Ultra-sensitive Magnetic Microscopy with an Optically Pumped Magnetometer," *Scientific Reports* **6**, 1–7 (2016).

[71] J. Lu, J. Wang, K. Yang, *et al.*, "In-Situ Measurement of Electrical-Heating-Induced Magnetic Field for an Atomic Magnetometer," *Sensors (Basel, Switzerland)* **20**, 22–25 (2020).

[72] N. Holmes, T. M. Tierney, J. Leggett, *et al.*, "Balanced, bi-planar magnetic field and field gradient coils for field compensation in wearable magnetoencephalography," *Scientific Reports* **9**, 14196 (2019).

[73] M. C. D. Tayler, K. Mouloudakis, R. Zetter, *et al.*, "Miniature Biplanar Coils for Alkali-Metal-Vapor Magnetometry," *Physical Review Applied* **10**, 14036 (2022).

[74] J. Chen, Z. Wu, G. Bao, *et al.*, "Design of coaxial coils using hybrid machine learning," *Review of Scientific Instruments* **92**, 045103 (2021).

[75] R. Carter, "Coil-system design for production of uniform magnetic fields," *Proceedings of the Institution of Electrical Engineers* **123**, 1279 (1976).

[76] M. Saqib, F. S. N., and F. J. N., "Design and Development of Helmholtz Coils for Magnetic Field," in *2020 International Youth Conference on Radio Electronics, Electrical and Power Engineering (REEPE)*, 1–5, IEEE (2020).

[77] A. F. Restrepo, E. Franco, H. Cadavid, *et al.*, "A comparative study of the magnetic field homogeneity for circular, square and equilateral triangular helmholtz coils," in *2017 International Conference on Electrical, Electronics, Communication, Computer, and Optimization Techniques (ICEECCOT)*, **2018-January**, 13–20, IEEE (2017).

[78] R. Hurtado-Velasco and J. Gonzalez-Llorente, "Simulation of the magnetic field generated by square shape Helmholtz coils," *Applied Mathematical Modelling* **40**, 9835–9847 (2016).

[79] A. F. Restrepo Alvarez, E. Franco Mejia, H. Cadavid Ramirez, *et al.*, "Analysis of the Magnetic Field Homogeneity for an Equilateral Triangular Helmholtz Coil," *Progress In Electromagnetics Research M* **50**, 75–83 (2016).

[80] K. Wang, B. Zhou, J. Tang, *et al.*, "Advances in laser heating of alkali vapor cells in magnetometers: a review," in *AOPC 2020: Optical Spectroscopy and Imaging; and Biomedical Optics*, Y. Wang, Y. Sun, J. Liu, *et al.*, Eds., 41, SPIE (2020).

[81] V. V. Yashchuk, S. Lee, and E. Paperno, "Magnetic Shielding," *Proceedings of the IEEE* **53**, 655 (1965).

[82] V. V. Yashchuk, S.-K. Lee, and E. Paperno, "Magnetic shielding," in *Optical Magnetometry*, D. F. J. K. Dmitry Budker, Ed., **9781107010352**, 225–248, Cambridge University Press, Cambridge (2013).

[83] M. S. Mrozowski, I. C. Chalmers, S. J. Ingleby, *et al.*, "Ultra-low noise, bipolar, programmable current sources," *Review of Scientific Instruments* **94**, 014701 (2023).

[84] G. Geršak and S. Beguš, "Thermometers in low magnetic fields," in *International Journal of Thermophysics*, **31**, 1622–1632 (2010).

[85] J. Mo, Y. Liu, H. Huang, *et al.*, "Coupling between visual alpha oscillations and default mode activity," *NeuroImage* **68**, 112–118 (2013).

[86] P. Welch, "The use of fast Fourier transform for the estimation of power spectra: A method based on time averaging over short, modified periodograms," *IEEE Transactions on Audio and Electroacoustics* **15**, 70–73 (1967).

[87] R. M. Hill, J. Devasagayam, N. Holmes, *et al.*, "Using OPM-MEG in contrasting magnetic environments," *NeuroImage* **253**, 119084 (2022).

[88] N. Holmes, J. Leggett, E. Boto, *et al.*, "A bi-planar coil system for nulling background magnetic fields in scalp mounted magnetoencephalography," *NeuroImage* **181**, 760–774 (2018).

[89] M. Rea, N. Holmes, R. M. Hill, *et al.*, "Precision magnetic field modelling and control for wearable magnetoencephalography," *NeuroImage* **241**, 118401 (2021).

[90] A. Jodko-Władzińska, K. Wildner, T. Pałko, *et al.*, "Compensation System for Biomagnetic Measurements with Optically Pumped Magnetometers inside a Magnetically Shielded Room," *Sensors* **20**, 4563 (2020).

[91] R. Dawson, C. O'Dwyer, E. Irwin, *et al.*, "Automated Machine Learning Strategies for Multi-Parameter Optimisation of a Caesium-Based Portable Zero-Field Magnetometer," *Sensors* **23**, 4007 (2023).

[92] J. Sheng, S. Wan, Y. Sun, *et al.*, "Magnetoencephalography with a Cs-based high-sensitivity compact atomic magnetometer," *Review of Scientific Instruments* **88**, 094304 (2017).

[93] J. Fang, R. Li, L. Duan, *et al.*, "Study of the operation temperature in the spin-exchange relaxation free magnetometer," *Review of Scientific Instruments* **86**, 73116 (2015).

[94] Q. Li, J. Zhang, L. Li, *et al.*, "The effects of phase retardation of wave plate on cesium magnetometer sensitivity," in *Applied Mechanics and Materials*, **203**, 263–267 (2012).

[95] F. Recknagel, "Applications of machine learning to ecological modelling," *Ecological Modelling* **146**, 303–310 (2001).

[96] A. Rajkomar, J. Dean, and I. Kohane, "Machine Learning in Medicine," *New England Journal of Medicine* **380**, 1347–1358 (2019).

[97] E. Horvitz and D. Mulligan, "Data, privacy, and the greater good," *Science* **349**, 253–255 (2015).

[98] C. Deans, L. D. Griffin, L. Marmugi, *et al.*, "Machine Learning Based Localization and Classification with Atomic Magnetometers," *Physical Review Letters* **120**, 033204 (2018).

[99] X. Meng, Y. Zhang, X. Zhang, *et al.*, "Machine Learning Assisted Vector Atomic Magnetometry," *arXiv [Instrumentation and Detectors]* **2301.05707**, 1–8 (2022).

[100] G. Carleo and M. Troyer, "Solving the quantum many-body problem with artificial neural networks," *Science* **355**, 602–606 (2017).

[101] A. Seif, K. A. Landsman, N. M. Linke, *et al.*, "Machine learning assisted readout of trapped-ion qubits," *Journal of Physics B: Atomic, Molecular and Optical Physics* **51**, 174006 (2018).

[102] I. Nakamura, A. Kanemura, T. Nakaso, *et al.*, "Non-standard trajectories found by machine learning for evaporative cooling of 87 Rb atoms," *Optics Express* **27**, 20435 (2019).

[103] P. B. Wigley, P. J. Everitt, A. van den Hengel, *et al.*, "Fast machine-learning online optimization of ultra-cold-atom experiments," *Scientific Reports* **6**, 25890 (2016).

[104] A. D. Tranter, H. J. Slatyer, M. R. Hush, *et al.*, "Multiparameter optimisation of a magneto-optical trap using deep learning," *Nature Communications* **9**, 4360 (2018).

[105] Y. Wu, Z. Meng, K. Wen, *et al.*, "Active Learning Approach to Optimization of Experimental Control*," *Chinese Physics Letters* **37**, 103201 (2020).

[106] A. J. Barker, H. Style, K. Luksch, *et al.*, "Applying machine learning optimization methods to the production of a quantum gas," *Machine Learning: Science and Technology* **1**, 015007 (2020).

[107] N. Siddique and H. Adeli, "Nature Inspired Computing: An Overview and Some Future Directions," *Cognitive Computation* **7**, 706–714 (2015).

[108] A. Slowik and H. Kwasnicka, "Evolutionary algorithms and their applications to engineering problems," (2020).

[109] T. Bäck and H.-P. Schwefel, "An Overview of Evolutionary Algorithms for Parameter Optimization," *Evolutionary Computation* **1**, 1–23 (1993).

[110] D. Whitley, "An overview of evolutionary algorithms: practical issues and common pitfalls," *Information and Software Technology* **43**, 817–831 (2001).

[111] Q. Zhao, H. Yan, and J. Jin, "Research on the Most Efficient Use of Wind Energy Resources in the Context of Carbon Neutrality: Overview Based on Evolutionary Algorithm," *Mathematical Problems in Engineering* **2022**, 1–12 (2022).

[112] J. H. Holland, *Adaptation in Natural and Artificial Systems*, The MIT Press, Cambridge (1975).

[113] J. Koza, "Genetic programming as a means for programming computers by natural selection," *Statistics and Computing* **4**, 87–112 (1994).

[114] R. Storn, "On the Usage of Differential Evolution for Function Optimization," in *Proceedings of North American Fuzzy Information Processing*, 519–523 (1996).

[115] R. Storn and K. Price, "Differential Evolution-A Simple and Efficient Heuristic for Global Optimization over Continuous Spaces," *Journal of Global Optimization* **11**, 341–359 (1997).

[116] T. Tušar and B. Filipič, "Differential Evolution versus Genetic Algorithms in Multiobjective Optimization," in *Evolutionary Multi-Criterion Optimization*, **4403 LNCS**, 257–271, Springer Berlin Heidelberg, (Berlin, Heidelberg) (2007).

[117] S. Ruder, "An overview of gradient descent optimization algorithms," *arXiv [Machine Learning]* **2**, 1609.04747 (2016).

[118] C. Darken, J. Chang, and J. Moody, "Learning rate schedules for faster stochastic gradient search," in *Neural Networks for Signal Processing II Proceedings of the 1992 IEEE Workshop*, 3–12, IEEE (1992).

[119] R. Sweke, F. Wilde, J. J. Meyer, *et al.*, "Stochastic gradient descent for hybrid quantum-classical optimization," *Quantum* **4**, 314 (2020).

[120] N. Khaneja, T. Reiss, C. Kehlet, *et al.*, "Optimal control of coupled spin dynamics: Design of NMR pulse sequences by gradient ascent algorithms," *Journal of Magnetic Resonance* **172**, 296–305 (2005).

[121] T. Dyer, S. J. Ingleby, C. Dunare, *et al.*, "Micro-fabricated caesium vapor cell with 5 mm optical path length," *Journal of Applied Physics* **132**, 204401 (2022).

[122] J. Iivanainen, M. Stenroos, and L. Parkkonen, "Measuring MEG closer to the brain: Performance of on-scalp sensor arrays," *NeuroImage* **147**, 542–553 (2017).

[123] T. P. Gutteling, M. Bonnefond, T. Clausner, *et al.*, "A New Generation of OPM for High Dynamic and Large Bandwidth MEG: The 4He OPMs—First Applications in Healthy Volunteers," *Sensors* **23**, 2801 (2023).

[124] M. Jas, S. R. Jones, and M. S. Hämäläinen, "Whole-head OPM-MEG enables noninvasive assessment of functional connectivity," *Trends in Neurosciences* **44**, 510–512 (2021).

[125] R. M. Hill, E. Boto, M. Rea, *et al.*, "Multi-channel whole-head OPM-MEG: Helmet design and a comparison with a conventional system," *NeuroImage* **219**, 116995 (2020).

[126] Y. Yang, M. Xu, A. Liang, *et al.*, "A new wearable multichannel magnetocardiogram system with a SERF atomic magnetometer array," *Scientific Reports* **11**, 5564 (2021).

[127] O. Alem, T. H. Sander, R. Mhaskar, *et al.*, "Fetal magnetocardiography measurements with an array of microfabricated optically pumped magnetometers," *Physics in Medicine and Biology* **60**, 4797–4811 (2015).

[128] R. Körber, J. H. Storm, H. Seton, *et al.*, "SQUIDs in biomagnetism: A roadmap towards improved healthcare," (2016).

[129] P. K. Mandal, A. Banerjee, M. Tripathi, *et al.*, "A Comprehensive Review of Magnetoencephalography (MEG) Studies for Brain Functionality in Healthy Aging and Alzheimer's Disease (AD)," *Frontiers in Computational Neuroscience* **12**, 60 (2018).

[130] H. Kwon, K. Kim, Y. H. Lee, *et al.*, "Non-invasive magnetocardiography for the early diagnosis of coronary artery disease in patients presenting with acute chest pain," *Circulation Journal* **74**, 1424–1430 (2010).

[131] Y. Chen and A. Zhan, "Clinical value of magnetic resonance imaging in identifying multiple cerebral gliomas from primary central nervous system lymphoma," *Oncology Letters* **18**, 593–598 (2019).

[132] J. Zhang, J. Xiang, L. Luo, *et al.*, "Editorial: EEG/MEG based diagnosis for psychiatric disorders," (2022).

[133] N. Hamedi, A. Khadem, M. Delrobaei, *et al.*, "Detecting ADHD Based on Brain Functional Connectivity Using Resting-State MEG Signals," *Frontiers in Biomedical Technologies* **9**, 110–118 (2022).

[134] H. Hamada, H. Horigome, M. Asaka, *et al.*, "Prenatal diagnosis of long QT syndrome using fetal magnetocardiography," *Prenatal Diagnosis* **19**, 677–680 (1999).

[135] S. Watanabe and S. Yamada, "Magnetocardiography in Early Detection of Electromagnetic Abnormality in Ischemic Heart Disease," *Journal of Arrhythmia* **24**, 4–17 (2008).

[136] M. A. Lopes, D. Krzemiński, K. Hamandi, *et al.*, "A computational biomarker of juvenile myoclonic epilepsy from resting-state MEG," *Clinical Neurophysiology* **132**, 922–927 (2021).

[137] J. Fang, T. Wang, W. Quan, *et al.*, "In situ magnetic compensation for potassium spin-exchange relaxation-free magnetometer considering probe beam pumping effect," *Review of Scientific Instruments* **85**, 063108 (2014).

[138] M. J. Brookes, J. Leggett, M. Rea, *et al.*, "Magnetoencephalography with optically pumped magnetometers (OPM-MEG): the next generation of functional neuroimaging," (2022).

[139] E. Boto, R. Bowtell, P. Krüger, *et al.*, "On the potential of a new generation of magnetometers for MEG: A beamformer simulation study," *PLoS ONE* **11**, e0157655 (2016).

[140] E. Boto, N. Holmes, J. Leggett, *et al.*, "Moving magnetoencephalography towards real-world applications with a wearable system," *Nature* **555**, 657–661 (2018).

[141] B. U. Westner, J. I. Lubell, M. Jensen, *et al.*, "Contactless measurements of retinal activity using optically pumped magnetometers," *NeuroImage* **243**, 118528 (2021).

[142] J. F. Schneiderman, "Information content with low- vs. high-Tc SQUID arrays in MEG recordings: The case for high-Tc SQUID-based MEG," *Journal of Neuroscience Methods* **222**, 42–46 (2014).

[143] J. Kitching, "Chip-scale atomic devices," *Applied Physics Reviews* **5**, 031302 (2018).

[144] E. Collett, *Field Guide to Polarization*, SPIE Press, Bellingham (2005).

[145] Z. Ding, J. Yuan, Z. Wang, *et al.*, "Optically pumped rubidium atomic magnetometer with elliptically polarized light," *Optik* **127**, 5270–5273 (2016).

[146] A. J. Mäkinen, R. Zetter, J. Iivanainen, *et al.*, "Magnetic-field modeling with surface currents. Part I. Physical and computational principles of bfieldtools," *Journal of Applied Physics* **128**, 063906 (2020).

[147] R. Zetter, A. J. Mäkinen, J. Iivanainen, *et al.*, "Magnetic field modeling with surface currents. Part II. Implementation and usage of bfieldtools," *Journal of Applied Physics* **128**, 063905 (2020).

[148] S. J. Ingleby, P. F. Griffin, A. S. Arnold, *et al.*, "High-precision control of static magnetic field magnitude, orientation, and gradient using optically pumped vapour cell magnetometry," *Review of Scientific Instruments* **88**, 043109 (2017).

[149] M. Nomura, Y. Nakaya, K. Saito, *et al.*, "Noninvasive localization of accessory pathways by magnetocardiographic imaging," *Clinical Cardiology* **17**, 239–244 (1994).

[150] F. E. Smith, P. Langley, P. van Leeuwen, *et al.*, "Comparison of magnetocardiography and electrocardiography: a study of automatic measurement of dispersion of ventricular repolarization," *EP Europace* **8**, 887–893 (2006).

[151] K. Kamada, Y. Ito, and T. Kobayashi, "Human MCG measurements with a high-sensitivity potassium atomic magnetometer," *Physiological Measurement* **33**, 1063 (2012).

[152] R. Wyllie, M. Kauer, G. S. Smetana, *et al.*, "Magnetocardiography with a modular spin-exchange relaxation-free atomic magnetometer array," *Physics in Medicine & Biology* **57**, 2619 (2012).

[153] Y. J. Kim, I. Savukov, and S. Newman, "Magnetocardiography with a 16-channel fiber-coupled single-cell Rb optically pumped magnetometer," *Applied Physics Letters* **114**, 143702–7 (2019).

[154] X. Bao, A. K. Abdala, and E. N. Kamavuako, "Estimation of the Respiratory Rate from Localised ECG at Different Auscultation Sites," *Sensors (Basel, Switzerland)* **21**, 1–11 (2021).

[155] E. Rodin, M. Funke, and J. Haueisen, "Cardio-respiratory contributions to the magnetoencephalogram," *Brain Topography* **18**, 37–46 (2005).

[156] C. M. Bentz, L. Baudzus, and P. M. Krummrich, "Signal to noise ratio (SNR) enhancement comparison of impulse-, coding- and novel linear-frequency-chirp-based optical time domain reflectometry (OTDR) for passive optical network (PON) monitoring based on unique combinations of wavelength selective mirrors," *Photonics* **1**, 33–46 (2014).

[157] E. Ashley and J. Niebauer, *Cardiology Explained*, vol. 1, REMEDICA, London (2004).

[158] K. Fujiwara, M. Oogane, A. Kanno, *et al.*, "Magnetocardiography and magnetoencephalography measurements at room temperature using tunnel magnetoresistance sensors," *Applied Physics Express* **11**, 023001 (2018).

[159] E. A. P. Alday, H. Ni, C. Zhang, *et al.*, "Comparison of Electric- and Magnetic-Cardiograms Produced by Myocardial Ischemia in Models of the Human Ventricle and Torso," *PLOS ONE* **11**, e0160999 (2016).

[160] G. Thut and C. Miniussi, "New insights into rhythmic brain activity from TMS-EEG studies," (2009).

[161] N. An, F. Cao, W. Li, *et al.*, "Multiple Source Detection Based on Spatial Clustering and Its Applications on Wearable OPM-MEG," *IEEE Transactions on Biomedical Engineering* **69**, 3131–3141 (2022).

[162] J. J. Li, P. C. Du, J. Q. Fu, *et al.*, "Miniature quad-channel spin-exchange relaxation-free magnetometer for magnetoencephalography," *Chinese Physics B* **28**, 040703 (2019).

[163] M. Pang, Z. Huang, H. Wu, *et al.*, "Thermal Analysis of Wearable OPM-MEG Array System for Auditory Evoked Experiments," *IEEE Sensors Journal* **22**, 4514–4523 (2022).

[164] S. Mellor, U. Vivekananda, G. C. O'Neill, *et al.*, "First experiences of whole-head OP-MEG recordings from a patient with Epilepsy," *medRxiv* **21264047**, 1–13 (2021).

[165] J. Iivanainen, R. Zetter, M. Grön, *et al.*, "On-scalp MEG system utilizing an actively shielded array of optically-pumped magnetometers," *NeuroImage* **194**, 244–258 (2019).

[166] T. H. Sander, U. Marhl, R. Brühl, *et al.*, "A 50 channel optically pumped magnetometer MEG in an externally actively shielded two-layer room," *International Journal of Bioelectromagnetism* **23**, 1–4 (2021).

[167] G. Roberts, N. Holmes, N. Alexander, *et al.*, "Towards OPM-MEG in a virtual reality environment," *NeuroImage* **199**, 408–417 (2019).

[168] S. Haegens, H. Cousijn, G. Wallis, *et al.*, "Inter- and intra-individual variability in alpha peak frequency," *NeuroImage* **92**, 46–55 (2014).

[169] W. Hohaia, B. W. Saurels, A. Johnston, *et al.*, "Occipital alpha-band brain waves when the eyes are closed are shaped by ongoing visual processes," *Scientific Reports* **12**, 1194 (2022).

[170] D. Ma, X. Fang, J. Lu, *et al.*, "Analysis and Measurement of Differential-Mode Magnetic Noise in Mn-Zn Soft Ferrite Shield for Ultra-Sensitive Sensors," *Materials* **15**, 8704 (2022).

[171] I. Savukov, Y. J. Kim, V. Shah, *et al.*, "High-sensitivity operation of single-beam optically pumped magnetometer in a kHz frequency range," *Measurement Science and Technology* **28**, 35104 (2017).